



저작자표시-비영리-변경금지 2.0 대한민국

이용자는 아래의 조건을 따르는 경우에 한하여 자유롭게

- 이 저작물을 복제, 배포, 전송, 전시, 공연 및 방송할 수 있습니다.

다음과 같은 조건을 따라야 합니다:



저작자표시. 귀하는 원저작자를 표시하여야 합니다.



비영리. 귀하는 이 저작물을 영리 목적으로 이용할 수 없습니다.



변경금지. 귀하는 이 저작물을 개작, 변형 또는 가공할 수 없습니다.

- 귀하는, 이 저작물의 재이용이나 배포의 경우, 이 저작물에 적용된 이용허락조건을 명확하게 나타내어야 합니다.
- 저작권자로부터 별도의 허가를 받으면 이러한 조건들은 적용되지 않습니다.

저작권법에 따른 이용자의 권리는 위의 내용에 의하여 영향을 받지 않습니다.

이것은 [이용허락규약\(Legal Code\)](#)을 이해하기 쉽게 요약한 것입니다.

[Disclaimer](#)

공학박사 학위논문

Extrusion Deformation Behavior of Magnesium Alloys

마그네슘합금의 압출변형거동에 대한 연구

2015년 2월

서울대학교 대학원

재료공학부

최기순

Extrusion Deformation Behavior of Magnesium Alloys

지도교수 신 광 선

이 논문을 공학박사 학위논문으로 제출함
2015년 1월

서울대학교 대학원
재료공학부
최 기 순

최기순의 박사 학위논문을 인준함
2015년 1월

위 원 장	<u>한 홍 남</u>	(인)
부위원장	<u>신 광 선</u>	(인)
위 원	<u>김 도 향</u>	(인)
위 원	<u>조 원 석</u>	(인)
위 원	<u>이 경 훈</u>	(인)

Abstract

Extrusion Deformation Behavior of Magnesium Alloys

Ki Soon Choi

School of Materials Science and Engineering

The Graduate School

Seoul National University

In this study, the extrusion deformation behavior of wrought magnesium alloys such as commercial AZ31 alloy and newly developed ZAM631 alloy was studied by using crystal plasticity and finite element method to improve the formability by controlling texture evolution. The study focused on investigating the microscopic deformation mechanism and the macroscopic extrusion deformation behavior of the alloys and intensively on predicting texture evolution of the alloys during extrusion.

When the critical resolved shear stress (CRSS) values and hardening parameters were investigated, the number of parameters for VPSC model could be more than 50 depending on the number of slip and twinning modes. Therefore optimization technique, Genetic Algorithm, was used to find the optimum CRSS values and hardening parameters of the alloys. To date, there are so many works that have been carried out to find the CRSS values for understanding the deformation mechanisms of magnesium and its alloys. But most of the works have been performed for 3 or 4 deformation modes at room temperature or single temperature without any temperature change. Because the plastic deformation of the alloys is greatly influenced by various parameters such as temperature and deformation modes, the considered deformation modes and the temperature range were very important to understand correctly the deformation mechanisms of the alloys. In this study,

five deformation modes were considered to be active per grain i.e. basal $\langle a \rangle$ slip, prismatic $\langle a \rangle$ slip, second order pyramidal $\langle c+a \rangle$ slip, tensile twin and compressive twin at the temperature range of 533~653K. Visco-plastic self-consistent-genetic-algorithm (VPSC-GA) optimizations were performed to find the optimal CRSS parameter sets corresponding to the process temperature and to investigate the microscopic deformation behavior. During compressive deformation, the basal $\langle a \rangle$ slip and tensile twin were mainly activated. The contribution of the basal $\langle a \rangle$ slip decreased and that of the tensile twin decreased with increasing temperature. The CRSS values decreased with increasing temperature in all deformation modes. The CRSS values of the prismatic $\langle a \rangle$ slip, the $\langle c+a \rangle$ slip and the compressive twin were strongly dependent on temperature, whereas the basal $\langle a \rangle$ slip and the tensile twin were weakly dependent on temperature.

The hot compression tests of AZ31 and ZAM631 alloy were performed at the temperature range of 533~653K and the strain rate range of 10^{-3} ~1/s using Gleeble thermo-mechanical simulator. The peak value of flow stress increased with increasing strain rate at constant temperature and decreased with increasing temperature at constant strain rate. The flow stress-strain curves showed distinct flow softening at all deformation conditions. The microstructures of samples sectioned parallel to deformation direction were examined by optical microscopy. The results showed that the flow softening were due to dynamic recrystallization (DRX) during deformation. The size of DRX grains was formulated as a function of the Zener-Hollomon parameter. The flow stress equation characterizing DRX has been derived. Good agreements between the predicted and measured flow stress were achieved.

A non isothermal three-dimensional finite element simulation of the indirect extrusion process was carried out by using the commercial rigid plastic software DEFORM-3D V11.0 to investigate the macroscopic extrusion deformation behavior of AZ31 and ZAM631 alloy during extrusion. Indirect extrusion processes were simulated at a reduction ratio 56:1 at the ram speed 1.2 cm/min for extruded plate (3t) and at a reduction ratio 25:1 at the ram speed 0.8 cm/min for extruded rod (16Φ), respectively. In order to reduce the

computational time, only a quarter model was used considering the rotational symmetry in geometry and loading condition. The flow stress model was implemented as a function of plastic strain, strain rate and temperature defined by the compressive stress-strain curves measured using a Gleeble thermo-mechanical simulator at the temperature range of 533~653K. The evolution of temperature, strain rate and strain during extrusion were predicted.

These macroscopic variables are not enough to predict quality of extruded product which is more strongly related to the microscopic variables such as slip activity and texture change. The VPSC model can predict microscopic evolution but only with simple loading condition at constant temperature. To monitor microscopic behavior during the non-isothermal extrusion process new methodology was designed to connect macroscopic deformation history to the microscopic model, VPSC. The modified VPSC-FE subroutine provided by VPSC7 released year 2007 is modified to accommodate different CRSS parameter sets at different temperature. In this study, 4 set of CRSS parameters are generated for each temperature using VPSC-GA and applied VPSC-FE model. The texture evolutions during the plate (3t) extrusion of AZ31 alloy and the rod (16Φ) extrusion of ZAM631 alloy were predicted by using the new methodology, respectively. The prediction showed good qualitative agreement with the experimental results. The new methodology can be successfully applied to infer the effects of temperature on the texture evolution and used to improve the formability of magnesium alloys by controlling the texture evolution during extrusion.

Keywords: Magnesium alloys, Extrusion, Texture, FEM, VPSC
Student Number: 2004-30237

Contents

Chapter 1 Introduction	1
1.1 Motivation	1
1.2 Wrought magnesium alloys	5
1.3 Plastic deformation in magnesium alloys	10
1.3.1 Slip System	10
1.3.2 Twinning system	14
1.4 Modeling of texture evolution	20
1.4.1 Sachs' model	20
1.4.2 Taylor model	20
1.4.3 Visco-plastic self-consistent (VPSC) model	21
1.5 Extrusion	23
1.5.1 Direct extrusion	23
1.5.2 Indirect extrusion	24
1.6 Rigid-plastic FEM analysis	26
1.6.1 Basic equations	26
1.6.2 Hybrid-mixed formulation of rigid-plastic finite element equations	27
1.7 Recent research status	29
1.7.1 Hot working process	29
1.7.2 Simulation of texture evolution	29
1.8 Research objectives	32
Chapter 2 Experimental procedures	33

2.1 Alloy selection and fabrication	33
2.1.1 Alloy selection	33
2.1.2 Casting and homogenization	37
2.2 Characterization analysis	38
2.2.1 Microstructure	38
2.2.2 Texture	38
2.2.3 Mechanical property	41
 Chapter 3 Numerical procedures	 42
3.1 FEM simulation of extrusion process	42
3.2 Prediction of texture evolution	47
 Chapter 4 Results and discussion	 50
4.1 Crystal plasticity analysis of magnesium alloys	50
4.1.1 Effects of temperature on CRSS for slip and twinning modes in AZ31 alloy	50
4.1.2 Effects of temperature on CRSS for slip and twinning modes in ZAM631 alloy	56
4.2 Hot deformation behavior of AZ31 alloy	61
4.2.1 Flow stress behavior	61
4.2.2 Microstructures	64
4.2.3 Modeling of flow stress	75
4.2.3.1 Determination of peak stress	75
4.2.3.2 Determination of flow stress	77
4.3 Hot deformation behavior of ZAM631 alloy	89
4.3.1 Flow stress behavior	89

4.3.2	Microstructures	92
4.3.3	Modeling of flow stress	101
4.3.3.1	Determination of peak stress	101
4.3.3.2	Determination of flow stress	102
4.4	Finite element analysis of extrusion process	113
4.4.1	FE analysis during AZ31 alloy plate (3t) extrusion	113
4.4.2	FE analysis during ZAM631 alloy rod (16Φ) extrusion ...	119
4.5	Texture evolution prediction of magnesium alloys during extrusion process	124
4.5.1	Texture evolution prediction during AZ31 alloy plate (3t) extrusion	124
4.5.2	Texture evolution prediction during ZAM631 alloy rod (16Φ) extrusion	135
Chapter 5 Conclusions		143
Bibliography		145
Appendix		153
초록		175

List of Tables

Table 1.1	Solubility of alloying elements	8
Table 1.2	Mechanical properties of commercial wrought magnesium alloys	9
Table 2.1	Chemical compositions of magnesium alloys	39
Table 3.1	Process parameters used in the extrusion process simulation	46
Table 4.1	Best-fit model parameters for AZ31 alloy describing the CRSS and hardening responses of the five deformation behaviors as a function of temperature	52
Table 4.2	Best-fit model parameters for pure magnesium single crystal describing the CRSS and hardening responses of the five deformation behaviors as a function of temperature	54
Table 4.3	Best-fit model parameters for ZAM631 alloy describing the CRSS and hardening responses of the five deformation behaviors as a function of temperature	58
Table 4.4	Average DRX grain size (D_{drx}) of AZ31 alloy at a strain -0.7	70
Table 4.5	DRX volume fraction (X_{DRX}) of AZ31 alloy at a strain -0.7	71
Table 4.6	$\ln Z$ values of AZ31 alloy under different deformation conditions	72
Table 4.7	Ψ and ξ values of AZ31 alloy under different deformation conditions	88
Table 4.8	Average DRX grain (D_{drx}) size of ZAM631 alloy at a strain -0.7	96
Table 4.9	DRX volume fraction (X_{drx}) of ZAZ631 alloy at a strain -0.7	97
Table 4.10	$\ln Z$ values of ZAM631 alloy under different deformation conditions	98

Table 4.11	Ψ and ξ values of ZAM631 alloy under different deformation conditions	112
------------	--	-----

List of Figures

Figure 1.1	Typical tensile strength and elongation for the common commercial wrought magnesium alloys	8
Figure 1.2	Slip system in HCP crystal; (a) basal, prismatic and pyramidal slip systems with $\langle a \rangle$ Burgers vector and (b) four possible pyramidal slip systems with $\langle c+a \rangle$ Burgers vector	12
Figure 1.3	Evolution of the dislocation source for a $\langle c+a \rangle$ pyramidal slip system; (a) cross slip of a dislocation, (b) formation of $\langle c+a \rangle$ dislocation junction and (c) cross slip of $\langle c+a \rangle$ dislocation	13
Figure 1.4	HCP lattice change after twinning; (a) θ angle between the compression direction and a axis (b) Rotation of an HCP lattice after twinning	17
Figure 1.5	Stress-strain curves of the extruded Mg-Zn-Zr alloy compression-tested at a temperature of 623K and a strain rate of 1/s	18
Figure 1.6	Sample area with recrystallized twins; (a) EBSD-Kikuchi band contrast map revealing recrystallized twins and $\{10\bar{1}2\}$ tensile twins, (b) detailed view of a recrystallized twin indicating the presence of some low angle boundaries (thin lines) within the recrystallized structure comprised of high angle boundaries (bold lines) and (c) neighboring tensile twin showing no recrystallization	19
Figure 1.7	Schematic diagrams of direct extrusion and indirect extrusion	25
Figure 2.1	Phase diagrams of binary Mg alloys; (a) Mg-Zn, (b) Mg-Al and (c) Mg-Mn	34
Figure 2.2	Gleeble-3500 thermo-mechanical simulator	40
Figure 2.3	Schematic representation of thermo-mechanical process ...	40
Figure 3.1	Schematic representation of the extrusion simulation procedure	

	in DEFORM software	44
Figure 3.2	Assembly of the meshed billet, die, ram and container for extruded rod (16Φ) simulation	45
Figure 3.3	Schematic flow chart for prediction of texture evolution during extrusion process	49
Figure 4.1	Experimental and simulated uni-axial compression curves of AZ31 alloy	53
Figure 4.2	Relative activities of the five deformation modes during uni-axial compressive deformation of AZ31 alloy	53
Figure 4.3	Comparison of CRSS values between AZ31 alloy and pure magnesium single crystal published data; (a) CRSS and (b) CRSS normalized by $CRSS_{basal\langle a \rangle}$	55
Figure 4.4	Experimental and simulated uni-axial compression curves of ZAM631 alloy	59
Figure 4.5	Relative activities of the five deformation modes during uni-axial compressive deformation of ZAM631 alloy	59
Figure 4.6	Comparison of CRSS values between ZAM631 alloy and pure magnesium single crystal published data; (a) CRSS and (b) CRSS normalized by $CRSS_{basal\langle a \rangle}$	60
Figure 4.7	True stress-true strain curves of AZ31 alloy at different strain rates; (a) $10^{-3}/s$, (b) $10^{-2}/s$, (c) $10^{-1}/s$ and (d) $1/s$	62
Figure 4.8	Microstructures of AZ31 alloy compressed at a strain rate $10^{-3}/s$ at a strain -0.3 and -0.7; (a) 533K, (b) 573K, (c) 613K and (d) 653K	66
Figure 4.9	Microstructures of AZ31 alloy compressed at a strain rate $10^{-2}/s$ at a strain -0.3 and -0.7; (a) 533K, (b) 573K, (c) 613K and (d) 653K	67
Figure 4.10	Microstructures of AZ31 alloy compressed at a strain rate $10^{-1}/s$ at a strain -0.3 and -0.7; (a) 533K, (b) 573K, (c) 613K and (d) 653K	68
Figure 4.11	Microstructures of AZ31 alloy compressed at a strain rate $1/s$ at a strain -0.3 and -0.7; (a) 533K, (b) 573K, (c) 613K and (d)	

	653K	69
Figure 4.12	Average DRX grain (D_{drx}) size of AZ31 alloy compressed at various strain rates at a strain -0.7	73
Figure 4.13	Relation between average DRX grain (D_{drx}) size and Zener-Hollomon parameter of AZ31 alloy	74
Figure 4.14	Schematic of the dependence of the peak stress of AZ31 alloy on temperature and strain rate; (a) schematic of $\ln \sigma_p$ versus $\ln \dot{\epsilon}$, (b) schematic of σ_p versus $\ln \dot{\epsilon}$, (c) schematic of $\ln(\sinh(\alpha \sigma_p))$ versus $1/T$, (d) schematic of $\ln(\sinh(\alpha \sigma_p))$ versus $\ln \dot{\epsilon}$, (e) schematic of $\ln(\sinh(\alpha \sigma_p))$ versus $\ln Z$ and (f) schematic of $\ln \epsilon_p$ versus $\ln Z$	79
Figure 4.15	Schematic of the relationship of $(\ln \sigma - \ln \sigma_p) / \ln \zeta \epsilon$ and ϵ of AZ31 alloy at different strain rates; (a) $10^{-3}/s$, (b) $10^{-2}/s$, (c) $10^{-1}/s$ and (d) $1/s$	82
Figure 4.16	Schematic of the rate of change of $(\ln \sigma - \ln \sigma_p) / \ln \zeta \epsilon$ with ϵ of AZ31 alloy at different strain rates; (a) $10^{-3}/s$, (b) $10^{-2}/s$, (c) $10^{-1}/s$ and (d) $1/s$	84
Figure 4.17	Comparison between model prediction results and experimental results of AZ31 alloy; (a) $10^{-3}/s$, (b) $10^{-2}/s$, (c) $10^{-1}/s$ and (d) $1/s$	86
Figure 4.18	True stress-true strain curves of ZAM631 alloy at different strain rates; (a) $10^{-3}/s$, (b) $10^{-2}/s$, (c) $10^{-1}/s$ and (d) $1/s$	90
Figure 4.19	Microstructures of ZAM631 alloy compressed at a strain rate $10^{-3}/s$ at a strain -0.3 and -0.7; (a) 533K, (b) 573K, (c) 613K and (d) 653K	93
Figure 4.20	Microstructures of ZAM631 alloy compressed at a strain rate $10^{-2}/s$ at a strain -0.3 and -0.7; (a) 533K, (b) 573K and (c) 613K	94
Figure 4.21	Microstructures of ZAM631 alloy compressed at a strain rate $10^{-1}/s$ at a strain -0.3 and -0.7; (a) 533K and (b) 573K	95
Figure 4.22	Average DRX grain (D_{drx}) size of ZAM631 alloy compressed	

	at various strain rates at a strain -0.7	99
Figure 4.23	Relation between average DRX grain (D_{drx}) size and Zener-Hollomon parameter of ZAM631 alloy	100
Figure 4.24	Schematic of the dependence of the peak stress of ZAM631 alloy on temperature and strain rate; (a) schematic of $\ln \sigma_p$ versus $\ln \dot{\epsilon}$, (b) schematic of σ_p versus $\ln \dot{\epsilon}$, (c) schematic of $\ln(\sinh(\alpha \sigma_p))$ versus $1/T$, (d) schematic of $\ln(\sinh(\alpha \sigma_p))$ versus $\ln \dot{\epsilon}$, (e) schematic of $\ln(\sinh(\alpha \sigma_p))$ versus $\ln Z$ and (f) schematic of $\ln \epsilon_p$ versus $\ln Z$	103
Figure 4.25	Schematic of the relationship of $(\ln \sigma - \ln \sigma_p) / \ln \zeta \epsilon$ and ϵ of ZAM631 alloy at different strain rates; (a) $10^{-3}/s$, (b) $10^{-2}/s$, (c) $10^{-1}/s$ and (d) $1/s$	106
Figure 4.26	Schematic of the rate of change of $(\ln \sigma - \ln \sigma_p) / \ln \zeta \epsilon$ with ϵ of ZAM631 alloy at different strain rates; (a) $10^{-3}/s$, (b) $10^{-2}/s$, (c) $10^{-1}/s$ and (d) $1/s$	108
Figure 4.27	Comparison between model prediction results and experimental results of ZAM631 alloy; (a) $10^{-3}/s$, (b) $10^{-2}/s$, (c) $10^{-1}/s$ and (d) $1/s$	110
Figure 4.28	Macroscopic extrusion deformation behavior of the AZ31 alloy at P1 traced during extrusion at 533K; (a) evolution of temperature, (b) evolution of effective strain rate and (c) evolution of effective strain	115
Figure 4.29	Macroscopic extrusion deformation behavior of the AZ31 alloy at P1 traced during extrusion at 573K; (a) evolution of temperature, (b) evolution of effective strain rate and (c) evolution of effective strain	116
Figure 4.30	Macroscopic extrusion deformation behavior of the AZ31 alloy at P1 traced during extrusion at 613K; (a) evolution of temperature, (b) evolution of effective strain rate and (c) evolution of effective strain	117
Figure 4.31	Macroscopic extrusion deformation behavior of the AZ31 alloy	

	at P1 traced during extrusion at 653K; (a) evolution of temperature, (b) evolution of effective strain rate and (c) evolution of effective strain	118
Figure 4.32	Macroscopic extrusion deformation behavior of the ZAM631 alloy at P1 traced during extrusion at 533K; (a) evolution of temperature, (b) evolution of effective strain rate and (c) evolution of effective strain	120
Figure 4.33	Macroscopic extrusion deformation behavior of the ZAM631 alloy at P1 traced during extrusion at 573K; (a) evolution of temperature, (b) evolution of effective strain rate and (c) evolution of effective strain	121
Figure 4.34	Macroscopic extrusion deformation behavior of the ZAM631 alloy at P1 traced during extrusion at 613K; (a) evolution of temperature, (b) evolution of effective strain rate and (c) evolution of effective strain	122
Figure 4.35	Macroscopic extrusion deformation behavior of the ZAM631 alloy at P1 traced during extrusion at 653K; (a) evolution of temperature, (b) evolution of effective strain rate and (c) evolution of effective strain	123
Figure 4.36	Measured texture distributions with the location in the remaining billet of AZ31 alloy extruded plate (3t) at 533K; (a) location of points at different stages of extrusion and (b) measured texture distributions (EBSD) at P1,P2 and P3	126
Figure 4.37	Predicted texture distributions with the location in the remaining billet of AZ31 alloy extruded plate (3t) at 533K; (a) location of points at different stages of extrusion and (b) predicted texture distributions (VPSC-FE) at P1,P2 and P3	127
Figure 4.38	Measured texture distributions and predicted texture distributions of AZ31 alloy extruded plate (3t) at 533K; (a) measured texture distributions (EBSD) at P1, P2 and P3 and (b)	

	predicted texture distributions (VPSC-FE) at P1, P2 and P3	128
Figure 4.39	Measured texture distributions with the extrusion temperature of AZ31 alloy extruded plate (3t); (a) location of points at different stages of extrusion and (b) measured texture distributions (XRD) at P3	129
Figure 4.40	Predicted texture distributions with the location in the remaining billet of AZ31 alloy extruded plate (3t) at 573K; (a) location of points at different stages of extrusion and (b) predicted texture distributions (VPSC-FE) at P1,P2 and P3	130
Figure 4.41	Predicted texture distributions with the location in the remaining billet of AZ31 alloy extruded plate (3t) at 613K; (a) location of points at different stages of extrusion and (b) predicted texture distributions (VPSC-FE) at P1,P2 and P3	131
Figure 4.42	Predicted texture distributions with the location in the remaining billet of AZ31 alloy extruded plate (3t) at 653K; (a) location of points at different stages of extrusion and (b) predicted texture distributions (VPSC-FE) at P1,P2 and P3	132
Figure 4.43	Comparison of predicted texture distributions of AZ31 alloy extruded plate (3t) with the extrusion temperature; (a) location of points at different stages of extrusion and (b) predicted texture distributions (VPSC-FE) at P3	133
Figure 4.44	Measured texture distributions and predicted texture distributions of AZ31 alloy extruded plate (3t) with the extrusion temperature; (a) measured texture distributions (XRD) at P3 and (b) predicted texture distributions (VPSC-FE) at P3	134
Figure 4.45	Measured texture distributions with the extrusion temperature	

	of ZAM631 alloy extruded rod (16Φ); (a) location of points at different stages of extrusion and (b) measured texture distributions (XRD) at P4	137
Figure 4.46	Predicted texture distributions with the location of remaining billet in ZAM631 alloy extruded rod (16Φ) at 533K; (a) location of points at different stages of extrusion and (b) predicted texture distributions (VPSC-FE) at P1, P2, P3 and P4	138
Figure 4.47	Predicted texture distributions with the location of remaining billet in ZAM631 alloy extruded rod (16Φ) at 613K; (a) location of points at different stages of extrusion and (b) predicted texture distributions (VPSC-FE) at P1, P2, P3 and P4	139
Figure 4.48	Predicted texture distributions with the extrusion temperature of ZAM631 alloy extruded rod (16Φ); (a) location of points at different stages of extrusion and (b) predicted texture distributions (XRD) at P4	140
Figure 4.49	Measured texture distributions and Predicted texture distributions with the extrusion temperature of ZAM631 alloy extruded rod (16Φ); (a) measured texture distributions (XRD) at P4 and (b) predicted texture distributions (VPSC-FE) at P4	141
Figure 4.50	Comparison between measured texture distribution and predicted texture distribution of specimen compressed to the true strain of -0.357 of ZAM631 alloy at 613K; (a) measured texture distribution (XRD) and (b) predicted texture distribution (VPSC-FE)	142

Chapter 1. Introduction

1.1 Motivation

Magnesium alloys have the lowest density (1.8 g/cm^3) among commercially available structural metals, and their specific strength and stiffness are high. Moreover, their recyclability and electromagnetic shielding are also superior [1]. For these reasons, magnesium alloys have recently received much attention because of the increasing demand for lightweight materials for automobile to reduce their environmental pollution [1-3].

The processes to manufacture the magnesium alloy components branch into two main processes. The first is the casting process such as die casting, gravity casting and sand casting. The second is the plastic forming process such as extrusion, forging and rolling. At the present, high-pressure die casting (HPDC) is the dominant process in producing magnesium alloy components. However, magnesium alloy components produced by HPDC suffer from entrapped gas pores as a result of high fill-up-rate, poor creep resistance due to fine grain size cast microstructure and unsuitable for welding [4]. On the other hand, the plastic forming process such as extrusion, forging and rolling has even more homogeneous and better properties than casted components. Therefore, wrought magnesium alloy products have several merits including higher strength and ductility, as well as a wide range of mechanical properties compared to casting alloy products. However, the application of wrought magnesium components to lightweight structures is limited because of its poor formability at room temperature.

The low formability at room temperature mainly arises from the limited number of slip systems that characterize the hexagonal close packed structure of magnesium alloys. According to the Von Mises criterion, five independent slip systems are needed to accommodate the arbitrary homogeneous deformation of polycrystalline materials. Basal $\langle a \rangle$ slip, prismatic $\langle a \rangle$ slip

and pyramidal $\langle a \rangle$ slip provide only four independent slip systems. Pyramidal $\langle c+a \rangle$ slip, which in principle provides the additional independent slip systems, is difficult to activate at room temperature because of its high CRSS. At room temperature, twinning can provide an independent deformation mechanism (in addition to basal and non-basal $\langle a \rangle$ slip systems) to satisfy the Von Mises criterion [5]. At elevated temperatures, the activation of pyramidal $\langle c+a \rangle$ slip and other non-basal slip occurs due to their lower CRSS, reducing flow stress and increasing formability. Therefore, the magnesium alloy forming technologies such as extrusion, forging and rolling have been used at elevated temperatures. During hot working, Some metallurgical phenomena such as work hardening (WH), dynamic recovery (DRV) and dynamic recrystallization (DRX) may occur simultaneously [6-7] resulting in refinement of grains and reduction of deformation resistance [8]. For magnesium alloys, due to its lower stacking fault energy (60~78 kJ/mol), DRX generally predominates during hot working process (e.g. above 513K) [9]. The strain softening due to DRV and DRX is the typical characteristic of the elevated flow stress behavior of magnesium alloys. The prediction of deformation resistance is very important, especially in hot deformation. The strain softening mechanism is governed by the volume fraction of DRX. Many researchers have studied to build the flow stress model of the hot deformation behavior of magnesium alloys. The flow stress can be expressed as the function of strain, strain rate and temperature. Most of the works only deal with the effect of strain rate and temperature. Therefore, they can only describe the effect of strain rate and temperature on the steady-state condition but not the whole mechanical characteristics during deformation. So, the flow stress model which includes the effect of strain is needed in order to design the deformation process describing the whole mechanical characteristics [10].

Extrusion is one of the bulk-working processes. It is extensively used to produce profiles in an efficient manner and even to introduce refined grain structure, thus enhancing strength and ductility [11-12]. Therefore, magnesium

extrusion is expected to be a promising bulk-working method, as the demand for lightweight structural components rises in the forthcoming years [13]. A number of experimental investigations have been performed to enhance extrudability of magnesium alloys [14-15]. Alternatively, the extrudability could first be determined by means of a numerical technique such as finite element analysis (FEA) to simulate the process and then validated through experiment [13]. This could be very cost effective way in the metal forming industry. But the application of finite element method (FEM) on magnesium extrusion has been performed scarcely, as compared with the aluminum extrusion. Therefore, the research on the FEA on magnesium extrusion is needed from both academic and industrial point of view.

Recently, some studies have been done to show that texture evolution during extrusion of magnesium alloys has great impact on its mechanical properties. Laser et al. [16] reported the extruded rods exhibit basal fiber texture (c-axis in the radial direction). Park et al. [17] showed that higher ram speed and lower exit temperature will result in a weaker fiber texture. Texture evolution is closely related to the activated deformation mechanisms. Although there have been a lot of progresses in this field, the correlation between texture evolution and the activated deformation modes has not yet been clear. Crystal plasticity has proven to be an adequate tool for understanding the micro-mechanism of plastic deformations in HCP metals and for predicting their macroscopic properties [18-20]. This approach requires detailed information on the local deformation mechanisms as on the distribution of crystallographic orientations of individual grains resulting from texture. Therefore, the study of finding relationship among the texture evolution, activation of various deformation systems and mechanical properties is needed essentially. Thus far, few studies on the prediction of texture evolution during extrusion process have been performed and any successful result has not been reported. In order to improve the formability and to expand the application of magnesium alloys in the automotive industry

and the electronics industry, the new methodology which can control the texture evolution during extrusion process is essentially needed.

1.2 Wrought magnesium alloys

Generally, the wrought magnesium alloys show superior mechanical properties compare to the cast magnesium alloys so that they can be applied for automotive and aircraft industries. Mechanical properties of wrought magnesium alloys can be improved by addition of alloying elements, solid solution hardening, precipitate hardening, aging hardening and so on. Solubility of alloying elements in magnesium is shown in Table 1.1. Figure 1.1 shows tensile properties of common wrought magnesium alloys. From the figure, wrought magnesium alloys can be divided into four types, age hardening magnesium alloys, non-age hardening magnesium alloys, magnesium-RE (Rare Earth) alloys and magnesium-lithium alloys. Table 1.2 shows the mechanical properties of commercial wrought alloys with their wrought processing method.

(1) Magnesium-Zinc (Age Hardening) Magnesium Alloys

The maximum solubility of zinc in molten magnesium is 6.0 wt.% and Mg-Zn alloys show a excellent hardness after typical age hardening with formation of precipitation such as coherent $MgZn_2$ and $MgZn$ phase. Mg-Zn alloys are age-hardenable, there is a great potential to improve the ductility by further heat treatment and addition of other alloying elements.

Minor additions may modify precipitation in Mg-Zn alloys. Ca and Sr which accelerate the rate of ageing but delay overageing, refine grain sizes, and increase the precipitates density.

(2) Magnesium-Aluminum (Non-age Hardening) Magnesium Alloys

Mg-Al-Zn series alloys are the most commonly used in wrought applications for their mechanical properties, corrosion resistance and relative ease of extrusion. The poor thermal stability of $Mg_{17}Al_{12}$ phase and its

discontinuous precipitation can result in substantial grain boundary sliding at elevated temperatures. The accelerated diffusion of Al in the magnesium matrix and the self-diffusion of magnesium at elevated temperature also contribute to creep deformation in Mg-Al based alloys. In addition, grain boundary sliding is an important deformation mechanism at elevated temperatures. The discontinuous $Mg_{17}Al_{12}$ lamellae on the grain boundaries are responsible for the deformation [21].

(3) Magnesium RE Alloys

The classification of rare earth metals can be divided into two groups. Cerium group (La, Ce, Pr, Nd, Pm, Sm and Eu) which has low solubility in magnesium and yttrium group (Gd, Tb, Dy, Ho, Er, Tm, Yb, Lu, Y and Sc) which has greater solubility in magnesium. Additions of the rare earths increase the strength of magnesium alloys at elevated temperature. They also reduce edge crack in rolling because they narrow the freezing range of magnesium alloys. Y containing Mg-RE alloys may accelerate solid solution and precipitation hardening, while Ce containing Mg-RE alloys only contribute to precipitation hardening. In most cases, Mg-RE alloys undergo post-extrusion heat treatments to improve their strength properties, but at the expense of ductility. It is possible for these heat-treated alloys to display a reduction in the yield asymmetry, but this is dependent upon the level of precipitation achieved within the grain structure.

(4) Magnesium-Lithium Alloys

The addition of Li to magnesium can increase mechanical properties, impact strength of magnesium alloys and significantly reduce the difference between tensile and compressive yield strength of magnesium alloys. An addition of Li below 5.5 wt.%, can reduce c/a axial ratio, which easily activate other slip systems [21]. The recent development of Mg-Li alloys has

concentrated on fully close packed hexagonal α -phase alloys (< 5 wt.% Li) because of the low-temperature instability of the mechanical properties of high lithium alloys [22].

Table 1.1 Solubility of alloying elements [23].

Alloying Elements	Maximum Solubility in Mg (wt.%)	
	at %	wt.%
Al	11.60	12.70
Sn	3.35	14.48
Zn	2.40	6.20
Zr	1.04	3.80
Sr	0.03	0.11
Y	3.75	12.47
Ca	0.82	1.35
Cu	0.01	0.03
Si	1.16	1.34
Mn	0.99	2.20

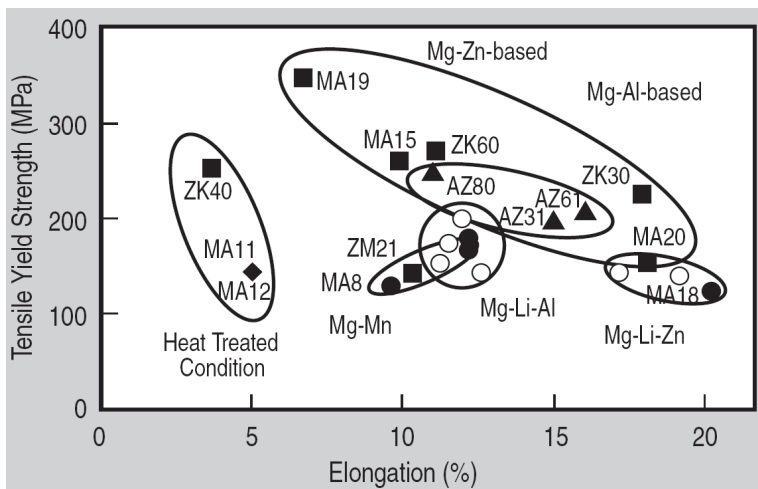


Figure 1.1 Typical tensile strength and elongation for the common commercial wrought magnesium alloys [22].

Table 1.2 Mechanical properties of commercial wrought magnesium alloys [23-24].

Alloys	Type	Tensile Properties		
		Y.S. (MPa)	U.T.S. (MPa)	El. (%)
AZ31	Extrusion	200(F)	255(F)	12(F)
WE54	Extrusion	190 (T6)	275 (T6)	10 (T6)
WE43	Extrusion	160 (T6)	260 (T6)	15 (T6)
ZM21	Extrusion	160	245	10
AZ80	Forging	200 (T5)	290 (T5)	6 (T5)
ZK31	Extrusion	225	305	8
ZK61	Extrusion	210	285	6
HK31	Sheet	170 (H24)	230 (H24)	4 (H24)
HM21	Forging	175 (T5)	225 (T5)	3 (T5)
HZ11	Extrusion	120	215	7
LA141	Sheet	95 (T7)	115 (T7)	10 (T7)

1.3 Plastic deformation in magnesium alloys

Plastic deformation in magnesium alloys with hexagonal close packed (HCP) crystallographic structure is due to both slip and twinning [25]. Due to the low symmetry, the deformation behavior of magnesium alloys is much more complicated than that of the high symmetry face centered cubic (FCC) structure metals, such as aluminum and copper. Dislocation slip in HCP metals can occur on basal (0001), prism $\{01\bar{1}0\}$, and pyramidal ($\{10\bar{1}1\}$ and $\{11\bar{2}2\}$) planes. In magnesium alloys, these slip systems are insufficient to satisfy the Taylor criterion for accommodation of the strain at grain boundaries. Hence, twinning on pyramidal planes plays an important role in the plastic deformation of magnesium alloys [26]. Therefore, the mechanical behavior of magnesium alloys can be controlled by the relative strengths and hardening responses of a variety of slip and twinning modes [27].

1.3.1 Slip system

Figure 1.2 shows the slip systems of HCP metals. It is well known that five independent slip systems are required for homogeneous plastic deformation in a polycrystalline material according to the von Mises criterion. In magnesium, the (0002) basal slip, which has only two independent slip systems, is preferentially operative because the CRSS for the basal slip is much lower than those for the non-basal slips at room temperature. On the other hand, the activation of $\langle c+a \rangle$ slip, which can accommodate c-axis strain, rarely occurs at room temperature. Thus, it is important to activate four independent modes by basal and pyramidal slips for plastic deformation in polycrystalline magnesium and its alloys at room temperature. Deformation twinning, which can accommodate c-axis strain, is an important deformation mechanism to be considered additionally because slip in the $\langle 11\bar{2}0 \rangle$ direction cannot accommodate c-axis strain [28].

The $\langle c+a \rangle$ slip or the second order pyramidal slip is important not only due to its four independent slip systems, but also due to the fact, that except deformation twinning, it is the only slip system with imparts deformation along the c -axis of the lattice. Yoo et al. [29] proposed a possible source mechanism for $\langle c+a \rangle$ dislocations, as shown in Figure 1.3. Figure 1.3(a) shows schematically the cross slip of a dislocation from the basal plane to a $(1\bar{1}00)$ prism plane. Figure 1.3(b) illustrates a $\langle c+a \rangle$ dislocation junction, along its near-screw orientation, formed when an active prismatic slip dislocation interacts with a sessile $\langle c \rangle$ dislocation. Here, $\langle c \rangle$ dislocations are assumed to exist in the grain matrix as a part of the initial microstructure. The subsequent cross slip of the $\langle c+a \rangle$ screw dislocation from the $(1\bar{1}00)$ prism plane to the $(11\bar{2}2)$ pyramidal plane is depicted in Figure 1.3(c). From the change in line tension calculated using the anisotropic elasticity theory, the cross slip of $\langle c+a \rangle$ screw dislocations from the prism plane into a pyramidal plane, at ambient temperatures, is energetically favorable in Zn and Be, and not in Mg and Ti. But, it becomes favorable in Ti at elevated temperatures above 573K.

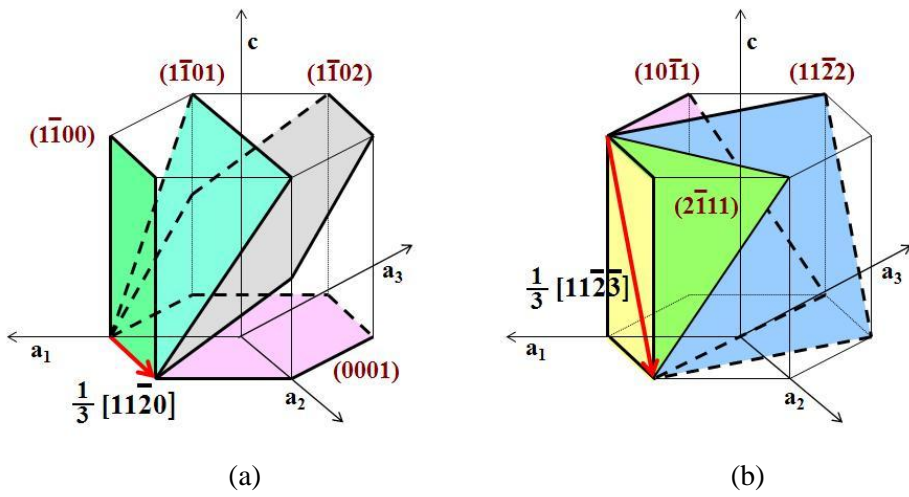


Figure 1.2 Slip system in HCP crystal; (a) basal, prismatic and pyramidal slip systems with $\langle a \rangle$ Burgers vector and (b) four possible pyramidal slip systems with $\langle c+a \rangle$ Burgers vector.

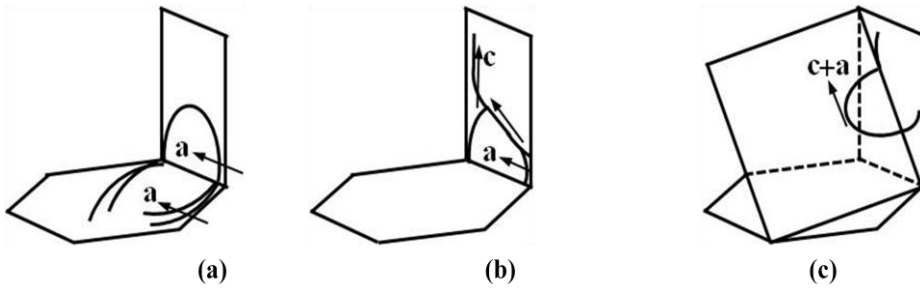


Figure 1.3 Evolution of the dislocation source for a $\langle c+a \rangle$ pyramidal slip system; (a) cross slip of $\langle a \rangle$ dislocation, (b) formation of $\langle c+a \rangle$ dislocation junction and (c) cross slip of $\langle c+a \rangle$ dislocation [29].

1.3.2 Twinning system

It is well known that twinning deformation modes play an important role during the deformation of magnesium alloys. Despite the limited contribution of twinning itself to the total plasticity, the abrupt change of orientation due to twinning may give rise to the reactivation of other slip systems. For metals with a c/a (where a and c are the lattice constants in hexagonal lattice) of less than $\sqrt{3}$ (e.g. titanium, zirconium, and magnesium), normally only the $\{10\bar{1}2\} \langle 10\bar{1}1 \rangle$ twin is activated by c -axis extension. During compression, the grains are favorably oriented if there are c -axes perpendicular to the compression direction and the twinning reorients the c -axes of the twins nearly parallel to the compression direction [30]. Twinning plays a vital role as the relaxation mechanisms. It is known that there are typical two deformation twin modes for magnesium; one is the $\{10\bar{1}2\} \langle 10\bar{1}1 \rangle$ tensile twin and another is the $\{10\bar{1}1\} \langle 10\bar{1}2 \rangle$ compression twin [28]. The former is generated at onset of plastic deformation and contributes to straining [31], on the other hand, the latter occurs at a late or final stage of deformation and serves to relax the stress concentration [32].

The initial texture after extrusion may be supposed to be the perfect fiber texture. After twinning, the twinned lattice reorientates itself, leading to a change of texture. Twinning mainly occurs on the $\{10\bar{1}2\}$ twinning plane, and the c -axis of the lattice rotates 86.3° about the $\langle 12\bar{1}0 \rangle$ direction after twinning (Figure.1.4 (a)). For the sake of simplification, the c -axis may be assumed to rotate 90° during twinning. After this rotation, the α angle between the loading direction and the c -axis is equal to $30^\circ - \theta$ (Figure.1.4 (b)). The angle θ changes from 0° to 30° . It can therefore be inferred that the α angle varies from 0° to 30° in twinned grains.

In twinning-dominated deformation, the strain-hardening region of a stress-strain curve exhibits marked changes in the strain-hardening rate. This region may be divided into three stages for the extruded Mg-Zn-Zr alloy, as

shown in Figure.1.5. At stage I, the flow stress increased slowly with strain. At stage II, the flow stress increased rapidly and the strain hardening reaches a high rate, and the stress-strain curve in nearly linear. At stage III, the strain hardening rate decreased gradually while the flow stress approaches a peak.

The strain hardening at stage I is mainly contributed by the tensile twins. These tensile twins expand and nearly consume the whole elongated grain matrix. Because of the broadening of the tensile twins during compression testing, they cannot refine the elongated grains effectively to raise the flow stress significantly through the Hall-Petch effect. The contribution of the tensile twins to strain hardening is mainly through the reorientation of grains, i.e., texture hardening [33].

Recently, there are several investigations the role of twins on DRX behavior in magnesium and its alloys. Al-Samman et al. [34] worked to gain information on the orientation of the recrystallized areas in a twin with respect to the neighboring twins and the parent grains by a detailed EBSD analysis in AZ31 alloy. A sample area with recrystallized twins is shown in Figure 1.6. The twin boundaries revealed $86^\circ \langle 11\bar{2}0 \rangle$ misorientation relationship with the matrix and therefore, were identified as $\{10\bar{1}2\}$ tensile twin which showed no DRX were free of low angle boundaries. The presence of some low angle boundaries in the recrystallized twin structure is apparently due to the dynamics of the process, that is low angle boundaries are first formed inside the twin and with progressing deformation they increasingly incorporate dislocations and eventually convert to high angle boundaries. He explained that this will fragment the original twin and creates a new structure of fine grains and also neighboring twins. Xu et al. [35] investigated the role of twins on DRX behavior in Mg-5.99Zn-1.76Ca-0.35 Mn (wt.%) alloy during indirect extrusion at 623K by EBSD analysis. In the early stage of extrusion, the activation of one special $\{10\bar{1}2\}\langle\bar{1}011\rangle$ tensile twin variant and the growth of twin lamellas resulted in the formation of coarse twinned areas. Fine-grained structures were preferentially formed near the twin boundaries due to

continuous DRX (CDRX). The CDRX process of untwinned matrix was faster than that of the twinned areas due to the preferential activation of prismatic slips. Therefore, the untwinned matrix was developed in the DRXed areas and the twinned areas temporarily remained in the unDRXed areas. Based on these results, He reported that $\{10\bar{1}2\}\langle\bar{1}011\rangle$ tensile twins played a dominant role in the formation of unDRXed areas. Wang et al. [36] reported different DRX mechanisms during hot rolling of AZ31 alloy where different types of twins were activated. The twin related DRX nucleation occurred mainly related to the $\{10\bar{1}1\} - \{10\bar{1}2\}$ double twinning. However, where the $\{10\bar{1}2\}$ tensile twinning was the dominant activated type of twins because the nucleation of DRX was mainly related to the original grain boundaries.

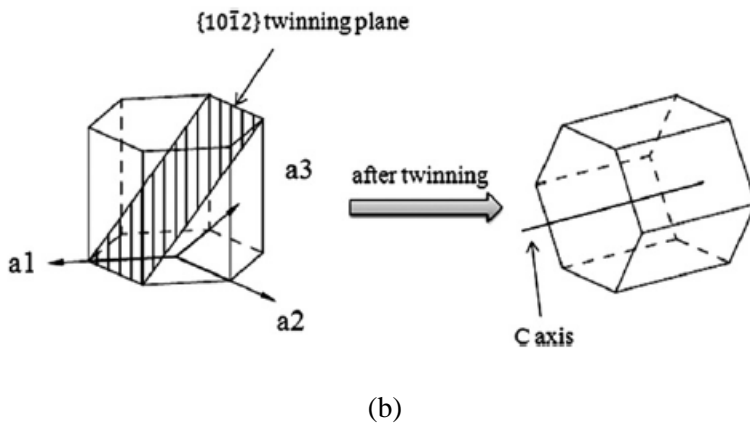
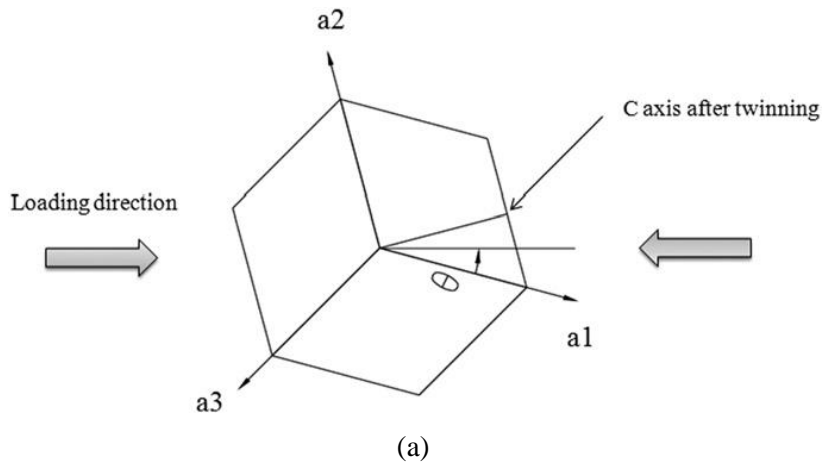


Figure 1.4 HCP lattice change after twinning; (a) θ angle between the compression direction and a axis (b) Rotation of an HCP lattice after twinning [33].

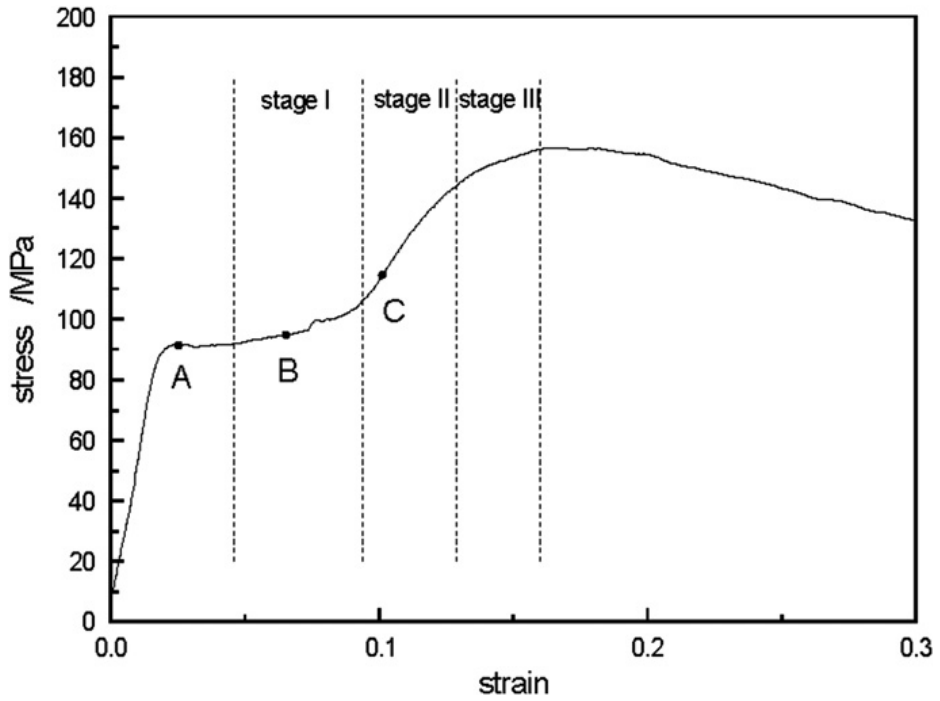


Figure 1.5 Stress-strain curves of the extruded Mg-Zn-Zr alloy compression-tested at a temperature of 623K and a strain rate of 1/s. The points along the curve ((A): $\epsilon = 0.025$, (B): $\epsilon = 0.065$ and (C): $\epsilon = 0.1$) indicate the strain where the compression tests were interrupted and microstructures examined [33].

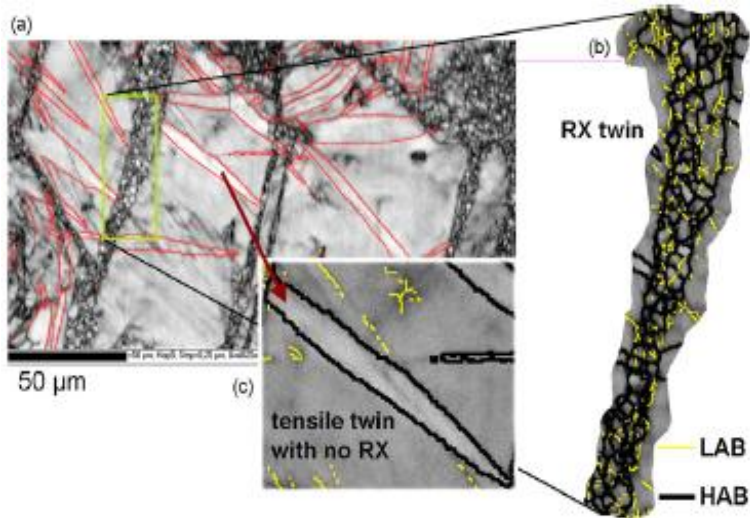


Figure 1.6 Sample area with recrystallized twins; (a) EBSD-Kikuchi band contrast map revealing recrystallized twins and $\{10\bar{1}2\}$ tensile twins, (b) detailed view of a recrystallized twin indicating the presence of some low angle boundaries (thin lines) within the recrystallized structure comprised of high angle boundaries (bold lines) and (c) neighboring tensile twin showing no recrystallization. [34].

1.4 Modeling of texture evolution

Polycrystal models have been developed to predict texture development and to calculate the stress-strain response of polycrystalline materials, considering texture evolution, evolving grain shapes, and single crystal hardening. As texture is a statistical property, large numbers of grains have to be considered in the representation of the polycrystal. It is best if the number is at least 1000 [37]. The main crystal plasticity models for large deformation are Sachs-type, Taylor-type and self consistent models. These models are based mainly on the physical deformation of slip and twinning, the two important modes. These models account for hardening and reorientation of single crystal grains.

1.4.1 Sachs' model

It is Sachs [38] who first proposed a model for polycrystalline plasticity by supposing that all grains within a polycrystal are subjected to the macroscopic stress mode and that they deform by single slip similarly to unconstrained single crystals. According to this model it can be maintained the stress continuity at grain boundary, but no strain compatibility because each grain has different strain values. Moreover the basic assumption itself is contradictory to the fact that stress status should be different in each grain in accordance with its orientation. Consequently, Sachs' model is applicable only for deformation in a single crystal [39].

1.4.2 Taylor model

Taylor model assumes that all grains must accommodate the same plastic strain equal to the macroscopically imposed strain. This implies that Taylor model neglects strain variations from grain to grain in the polycrystalline

aggregate. As a consequence, Taylor model does not consider the interaction between crystals, which is believed to be less significant in FCC and BCC materials due to their high crystallographic symmetries. Taylor model has played an important role in the field of modeling of forming of aluminum and steel sheets [40-42]. However, when the full constraints (FC) Taylor model is applied to simulate the deformation textures of FCC metals, a problem arises in that the yield conditions can be fulfilled by more than the necessary 5 slip systems, namely 6 or 8 slip systems. For the relaxed constraints (RC) Taylor-models, the ambiguity in selecting active slip systems exists [43].

1.4.3 Visco-plastic self-consistent (VPSC) model

Polycrystal plasticity and texture evolution of hexagonal materials are characterized by the diversity of possible deformation mechanisms such as basal slip, prismatic slip, pyramidal slip and several twinning modes. The low symmetry nature of these polycrystals may present high anisotropy and kinematic deficiencies. The difficulty of modeling of the plastic behavior of HCP metals is mainly due to the lack of slip systems available to satisfy the von-Mises criterion owing to the hexagonal symmetry of the lattice cell. In other words, hard glide systems should be activated to accommodate any arbitrary deformation. The VPSC model is well suited to model large strain behavior of polycrystalline materials. It accounts for the plastic anisotropy of each grain, as well as that of the polycrystal. Each grain is modeled as an ellipsoidal inclusion which is embedded into the so called Homogeneous Equivalent Medium (HEM) with the average properties of the whole polycrystal. The VPSC is given its name because the visco-plastic compliance tensor of the polycrystal is determined in each strain increment in a self-consistent manner. With the help of this tensor and by solution of the Eshelby inclusion problem, stress and strain state of each individual crystal is determined. For self consistency, the macroscopic stress and strain rate of the

HEM are set equal to the average of the stresses and strain rates of all the individual grains, each of which, in turn, is governed by its interaction with the HEM. Unlike one consequence of the self-consistent formulation is that each grain changes its form according to its local velocity gradient and deformation history. Another important consequence of the self-consistent formulation is that a grain no longer needs to have five independent slip systems to deform. This feature is especially important for non-cubic crystal structures, like hexagonals. In VPSC modeling it is, therefore, possible that a given grain deforms solely by basal slip while the other grains are deforming also on non-basal slip systems or by deformation twinning [44-45].

1.5 Extrusion

Extrusion is based on the plastic deformation of a material due to shear and compressive forces only; no tensile stresses are applied to the extruded metal. Basically, extrusion is the process by which a block of metal, such as a cylindrical billet, is forced to flow through a die orifice under high pressure and is thus reduced in cross-section, producing the required form of the product. Depending on the ductility of the material, metals may be extruded in either hot or cold conditions.

The extrusion of metals is used for the minimal extra finishing tasks the parts need after production; extruded parts usually have a constant cross-section along their length. This type of process works inexpensively in large quantity production. This process is also efficient in its flexibility. That is, if a part with a different cross section is needed, it is not necessary to get another machine to produce it; it only requires a change in the type of die. Therefore, extrusion is recommended for the production of long, straight sections with constant cross-sectional dimensions [46]. The extrusion can be mainly divided into direct and indirect extrusion, as shown in Figure 1.7.

1.5.1 Direct extrusion

Direct extrusion is the most commonly used extrusion process. A billet is inserted into the container. When the punch advances, the metal of the billet fills the container and is pressed against the die. With further movement of the ram, the billet starts to flow through the container and out through the die as a profile, with the same cross section as the die orifice [47].

Direct extrusion leaves a dead-metal zone at the end of the container surrounding the cone-shaped section of flowing metal. Oxides, inclusions, and other impurities from the skin of the billet accumulate in this area. Care must be taken to ensure that extrusion is stopped before this contaminated alloy is

carried through the die and into the billet. The main problem in direct extrusion is that frictional forces are created between the walls of the container and the billet; thus more force and power are required to run the extrusion process [46].

1.5.2 Indirect extrusion

In indirect extrusion, the die at the front end of the hollow stem moves relative to the container but there is no relative displacement between the billet and the container. Therefore, indirect extrusion is characterized by the absence of friction between the billet surface and the container (in indirect extrusion without a shell) and no displacement of the billet center relative to the peripheral regions. Therefore, the load required to extrude is decreased compared with direct extrusion [48].

Indirect extrusion has some advantages compared with direct extrusion. It does not require pressing the billet through the container. Due to this, the required extrusion force is lower, and in addition, there is better dimensional stability of the extruded profile. A third advantage is that the deformation of the metal flowing out through the die opening is more constant along the length of the profile than in direct extrusion, for there is almost zero pre-deformation of the billet in its back portion. In direct extrusion, these pre-deformations are bigger, especially the deformations of the peripheral layers of the billet, which is forced to slide along the container wall with the advance of the ram [47].

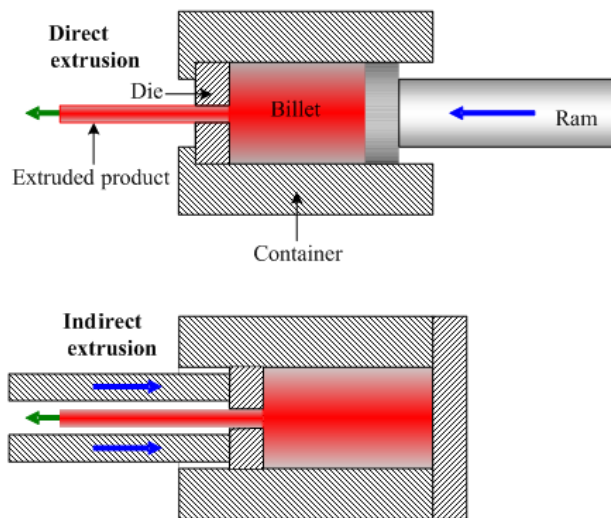


Figure 1.7 Schematic diagrams of direct extrusion and indirect extrusion.

1.6 Rigid-plastic FEM analysis

In metal forming process, depending on the model of material chosen, the finite element method can be mainly classified as elastic-plastic and rigid-plastic method. As elastic-plastic analysis considers the transition between the elastic and plastic regions, it can obtain more reliable stress and strain distribution, and treat geometric nonlinearity and instability. However, as it has to check whether an element attains yielding or not at every step, time increment should not be large. Therefore, it considerably needs large computational time and its formulation usually gets complicated for analyzing nonlinear material behavior. The rigid-plastic analysis is more effective in computational time and in formulation, on the basis that elastic deformation is far smaller compared with the plastic deformation in metal forming problems subject to large deformation such as extrusion and forging [49-50].

In this reasons, the rigid-plastic analysis is used to analyze the extrusion deformation behavior of magnesium alloys in the present work.

1.6.1 Basic equations

When the body is forced from exterior, the internal stress is generated in the interior of the body and reach in equilibrium. The equation to express this phenomenon is then given by the following:

$$\frac{\partial \sigma_{ij}}{\partial x_j} + \rho b_i = \rho a_i \quad (1.1)$$

where x_j is the location at equilibrium position, ρ is the density of body, a_i is the acceleration, and σ_{ij} is the stress. If the body force and the acceleration are ignored, the equation (1.1) is then given by the following form:

$$\frac{\partial \sigma_{ij}}{\partial x_j} = 0 \quad (1.2)$$

When the body is forced from exterior, the body is deformed. The strain rate $\dot{\epsilon}_{ij}$ to express this phenomenon is then given by the following:

$$\dot{\epsilon}_{ij} = \frac{1}{2} \left(\frac{\partial u_i}{\partial x_j} + \frac{\partial u_j}{\partial x_i} \right) \quad (1.3)$$

where u_i is the velocity at any point.

The equations that characterize a relation between stress and strain are called constitutive equations. The Levy-Mises' rigid-plastic equations called flow rules are used in the present work.

$$\dot{\epsilon}_{ij} = \frac{3}{2} \frac{\bar{\dot{\epsilon}}}{\bar{\sigma}} \dot{\sigma}_{ij} \quad (1.4)$$

where $\dot{\sigma}_{ij}$ is the deviatoric stress, $\bar{\sigma}$ is the effective stress and $\bar{\dot{\epsilon}}$ is the effective strain rate.

$$\dot{\sigma}_{ij} = \sigma_{ij} - \frac{1}{3} \delta_{ij} \sigma_{kk} \quad (1.5)$$

$$\bar{\sigma} = \sqrt{\frac{3}{2} \dot{\sigma}_{ij} \dot{\sigma}_{ij}} \quad (1.6)$$

$$\bar{\dot{\epsilon}} = \sqrt{\frac{3}{2} \dot{\epsilon}_{ij} \dot{\epsilon}_{ij}} \quad (1.7)$$

where δ_{ij} is the Kronecker delta.

The boundary conditions for body surface have to be also satisfied and are given then by the following:

$$\begin{aligned} \sigma_{ij} \cdot n_j &= \bar{F}_i \quad \text{on } S_F \\ u_i &= \bar{u}_i \quad \text{on } S_u \end{aligned} \quad (1.8)$$

where S_F is the region influenced by F on the body surface, F is the surface force per unit area and S_u is the region designated by \bar{u} on the body surface.

1.6.2 Hybrid-mixed formulation of rigid-plastic finite element equations

When the virtual work rate is applied to the equation (1.2), the equation is then given by the following:

$$\int_V \sigma_{ij} \delta \dot{\epsilon}_{ij} dV = \int_{S_t} F_i \delta u_i dS \quad (1.9)$$

In order to find the optimum velocity field, the variational principal method is

used. From the equation (1.9), the variational functional can be expressed by the following:

$$\delta\pi = \int_V \sigma_{ij} \delta\dot{\epsilon}_{ij} dV - \int_{s_t} F_i \delta u_i dS = 0 \quad (1.10)$$

When the equation (1.5) is substitute for the equation (1.10), the equation is then given by the following:

$$\delta\pi = \int_V \sigma_{ij} \delta\dot{\epsilon}_{ij} dV + \int_V \sigma_m \delta_{ij} \delta\dot{\epsilon}_{ij} dV - \int_{s_t} F_i \delta u_i dS = 0 \quad (1.11)$$

where σ_m is the mean stress and can be expressed by hydrostatic pressure, p , as following:

$$\sigma_m = \frac{1}{3} \sigma_{ij} \delta_{ij} = -p \quad (1.12)$$

When the equation (1.12) is substitute for the equation (1.11) and the constitutive equation is used, the equation is then given by the following:

$$\delta\pi = \int_V \bar{\sigma} \delta\bar{\epsilon} dV + \int_V p \delta\dot{\epsilon}_V dV - \int_{s_t} F_i \delta u_i dS = 0 \quad (1.13)$$

In order to consider the incompressibility, the penalty constant is used, as following:

$$\frac{p}{K_V} + \dot{\epsilon}_V = 0 \quad (1.14)$$

where K_V is the bulk penalty constant.

When the equation (1.14) is substitute for the equation (1.13) using Lagrange Multiplier, the equation is then given by the following:

$$\delta\pi = \int_V \bar{\sigma} \delta\bar{\epsilon} dV - \int_V p \delta\dot{\epsilon}_V dV - \int_{s_t} F_i \delta u_i dS - \int_V \left(\frac{p}{K_V} + \dot{\epsilon}_V \right) \delta p dV = 0 \quad (1.15)$$

1.7 Recent research status

Commercial wrought magnesium alloys have low formability due to the mechanical anisotropy and strong basal texture. For these reasons, the application of magnesium alloys has been limited in industries. Therefore, researches on the optimization of hot working processes such as extrusion, rolling, forging and equal channel angular pressing (ECAP), etc. are actively being progressed to improve the formability of magnesium alloys with controlling the microstructures and texture.

1.7.1 Hot working process

Severe plastic deformation (SPD) processes have been carried out to further improve the strength and ductility of magnesium alloys by controlling microstructures and texture [51-52]. Various SPD processes such as ECAP, accumulative roll-bonding (ARB), high pressure torsion (HPT), repetitive corrugation and straightening (RCS), cyclic extrusion compression (CEC), torsion extrusion, severe torsion straining (STS), cyclic closed-die forging (CCDF) and super short multi-pass rolling (SSMR) have been developed. These developed SPD processes provide high strength and good ductility to Mg alloys. However, the application of SPD in industries is limited because the available billet size is small. Therefore, the development of new methods for producing larger billets will expand the area of their applications [53-54].

1.7.2 Simulation of texture evolution

During the past few decades, the simulation of texture has become an established technique, due to advancement in microcomputer technology and plasticity modeling such as relaxed constraints (RC), full constraints (FC) and visco-plasticity self-consistent (VPSC) model [55]. FC and RC models have

brought satisfactory results for simulating the texture evolution, especially in cubic structured materials. However, there are certain limitations in both the models. The FC model doesn't consider any possible departure of grain deformation from the averaging aggregate's behavior. Though the relaxation in the RC model is based on considering the grain shape, its application is restricted to materials with highly distorted grains and with many equivalent slip systems such as FCC and BCC metals [39, 56]

It is known that in the case of HCP polycrystal, the individual grains split up into groups of hard and soft grains. The partition of plastic strain can be quite different between these groups. VPSC has been developed to solve these problems [45].

Thus far, a number of researches to predict texture evolution of magnesium alloys have been performed using VPSC model. Agnew et al. analyzed the mechanical behavior of pure magnesium and its solid solution alloys containing Li or Y additions at room temperature (RT). They have accounted the differences in the mechanical behavior of different alloys with VPSC model. They have also reported that the plane strain compression textures of the alloys exhibit an increased tendency for the basal poles to rotate away from the normal direction towards the rolling direction. This was primarily caused by an increased activity of the non basal $\langle c+a \rangle$ slip mode with VPSC model [55]. Yi et al. demonstrated the interaction between the texture and the deformation behavior of extruded magnesium alloy AZ31 at RT using in situ texture measurements and VPSC simulations [57]. Choi et al. reported that the tensile twin largely accommodates the deformation at a low strain level after performing uniaxial compression test at 473K with VPSC model [58].

All the above researchers demonstrated the utility of VPSC model in predicting texture evolution but performed those works at RT or single temperature without any temperature change. Although the process temperature changed during extrusion of magnesium and its alloys, the effects

of temperature have not yet been considered systematically in predicting texture evolution. The texture evolution during extrusion is influenced by both microscopic variables such as slip and twinning and macroscopic variables such as temperature, strain rate and strain. However, any successful researches to connect the macroscopic behavior to the microscopic behavior have not yet been reported. Therefore, the new methodology, which connects the macroscopic behavior to the microscopic behavior, has been proposed to predict the texture evolution during extrusion in this study.

1.8 Research objectives

The overall objective of this study is to predict the texture evolution during extrusion of magnesium alloys to improve their formability by considering both macroscopic and microscopic deformation behavior. This will help to control the texture evolution and facilitate the design of hot extrusion process. As a result, the markets for wrought magnesium alloys will be expanded in various fields and reduce the environmental pollution worldwide. The following objectives are sought in this study:

i) Investigation of the working temperature effects on the critical resolved shear stress (CRSS) values and hardening parameters for various major slip and twin systems of the AZ31 and the ZAM631 alloy. This will help to understand microscopic deformation behavior of the alloys. Visco-plastic self-consistent (VPSC) optimizations were performed by using genetic algorithm (GA) to find the best fitted CRSS sets.

ii) To investigate the relations among the parameters such as temperature, strain rate and strain during extrusion of the alloys. This will help to understand the macroscopic deformation behavior of the alloys. The simulation of the indirect extrusion process was carried out by using finite element method (FEM) to investigate the relations among the parameters.

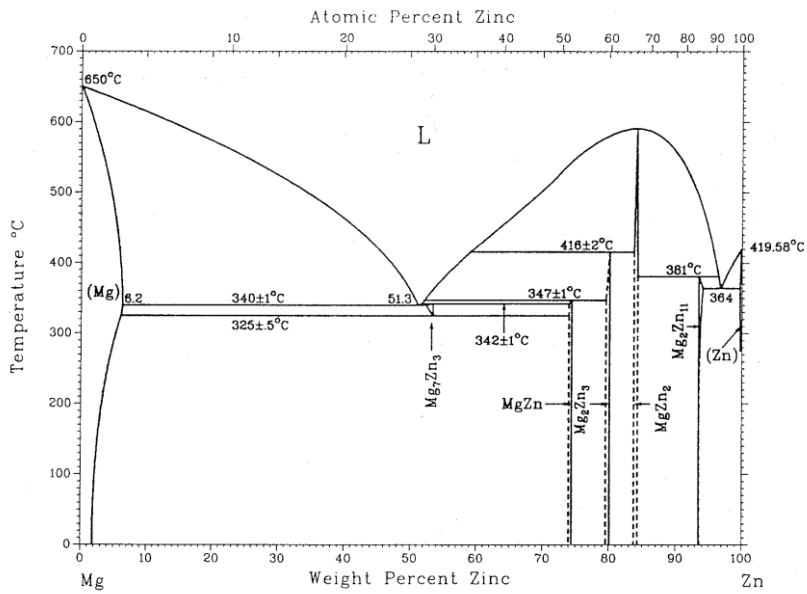
iii) To design a new methodology to connect the macroscopic behavior to the microscopic behavior for predicting texture evolution during extrusion of the alloys. This will help to control the texture evolution and improve the formability of magnesium alloys. The VPSC model was employed with subroutine, VPSC-FE and FEM was used for macroscopic deformation history.

Chapter 2. Experimental procedures

2.1 Alloy selection and fabrication

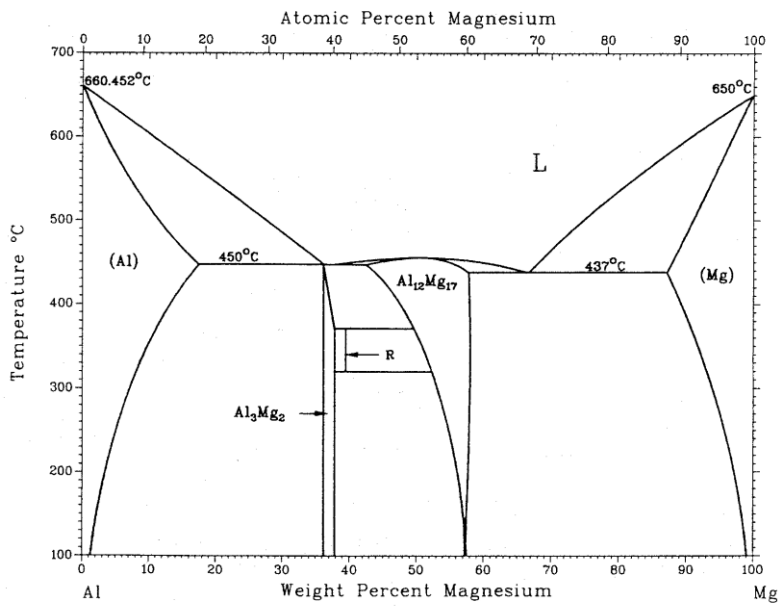
2.1.1 Alloy selection

Mg-Zn alloys are age-hardenable, there is a great potential to improve the ductility by further heat treatment and addition of other alloying elements because Mg-Zn alloys can form metastable precipitations such as MgZn, MgZn₂ and Mg₂Zn₃ phase [21-22]. Figure 2.1 shows Mg-Zn binary phase diagrams, Mg-Al binary phase diagrams and Mg-Mn binary phase diagrams. Maximum solubility of Zn to Mg is about 6.2 wt.% at 613K. In this study, AZ31 and ZAM631 alloy were selected owing to various merits. In order to maximize the age hardening response, the maximum amount of Zn was 6.0 wt.%, Al was added about 3.0 wt% and Mn was added 0.7~1.0 wt.%. Thus, ZAM631 alloy have a better age hardening response, strength and ductility than other wrought magnesium alloys. AZ31 alloy has been used the most widely in the commercial wrought magnesium alloys and has better extrusion characteristics, strength and ductility than other commercial wrought magnesium alloys.



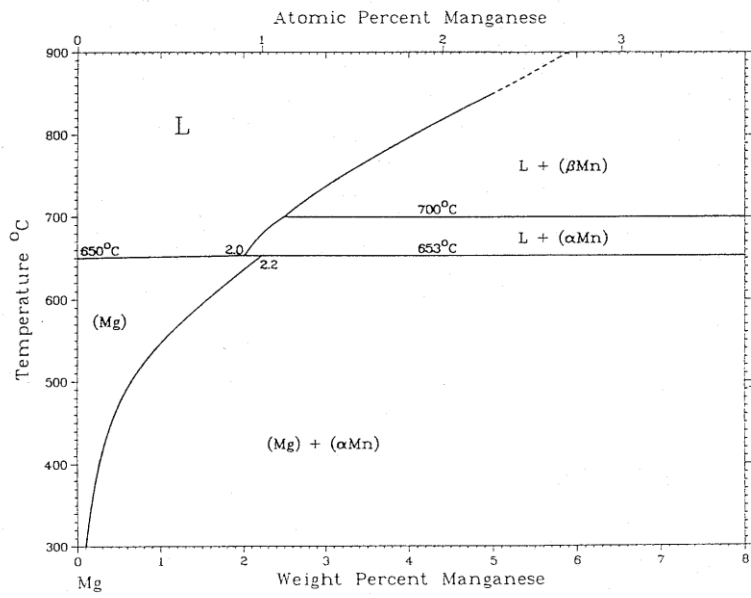
(a)

Figure 2.1 Phase diagrams of binary Mg alloys; (a) Mg-Zn, (b) Mg-Al and (c) Mg-Mn.



(b)

Figure 2.1 Continued.



(c)

Figure 2.1 Continued.

2.1.2 Casting and homogenization

The alloys were melted in clean steel crucible and the melt surface was protected with gaseous mixture of $\text{CO}_2+0.5\% \text{SF}_6$. The steel crucible was designed to manufacture the billets having the dimensions 80 mm (diameter) and 180 mm (height). Zn, Al and Mn with 99.99% purity were added to pure molten Mg at 973K. After the addition of alloying elements, the melt was mechanically stirred for 15 minutes, and the crucible was direct quenched into cold water at 973K. The nominal compositions of fabricated alloys are given in Table 2.1. The ingots were homogenized at 673K for 12 hrs, water-cooled, and subsequently machined to 80 mm diameter billets.

2.2 Characterization analysis

2.2.1 Microstructure

The microstructure was examined by optical microscopy. The specimens for microstructure observation were sectioned parallel to deformation direction. These specimens mechanically polished with sandpaper #4000 and then polished with 0.3 μm alumina powder. These specimens were then etched with acetic-picral (10 ml acetic acid + 4.2 g picric acid + 10 ml H₂O + 70 ml ethanol (95%)) [59].

2.2.2 Texture

The texture was measured by the X-ray diffraction using the Schulz reflection method by the X'pert pro XRD machine (Philips) with nickel-filtered copper target and the acceleration voltage and current were 40 kV and 30 mA respectively. For the texture measurement, the compressed and sectioned specimens were mechanically polished with sandpaper #4000 and then polished with 0.3 μm alumina powder. A set of five pole figures ((0002), {10 $\bar{1}$ 0}, {10 $\bar{1}$ 1}, {10 $\bar{1}$ 2} and {11 $\bar{2}$ 0}) was collected and used to obtain the orientation distribution function (ODF) after background removal and defocusing correction of the raw experimental data with LaboTex 3.0 software.

Table 2.1 Chemical compositions of magnesium alloys.

Alloy	Chemical Compositions (wt.%)					
	Zn	Al	Mn	Si	Cu	Mg
AZ31	0.727	3.187	0.287	0.018	0.004	Bal.
ZAM631	6.416	2.945	0.825	0.010	0.002	Bal.



Figure 2.2 Gleeble-3500 thermo-mechanical simulator.

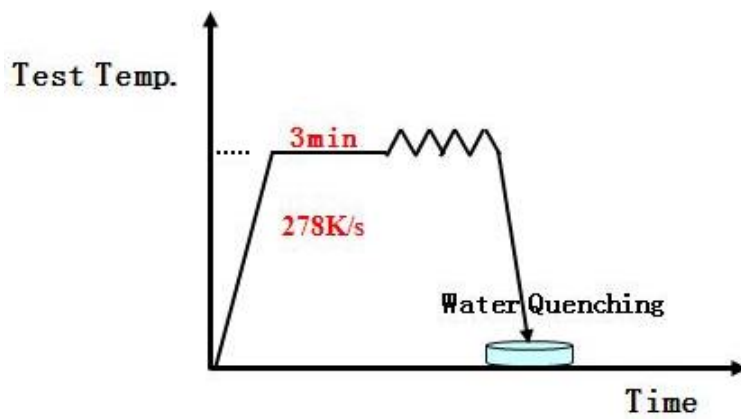


Figure 2.3 Schematic representation of thermo-mechanical process.

2.2.3 Mechanical property

Mechanical properties were evaluated by compressive tests. Compressive tests were conducted by using Gleeble thermo-mechanical simulator for AZ31 and ZAM631 alloy. Figure.2.2 shows Gleeble-3500 thermo-mechanical simulator. Cylindrical compressive specimens (10 mm in diameter and 15 mm in height) were cut along the extrusion direction from the billet. Isothermal compression tests were carried out at the temperature range of 533~653K with 40K intervals and strain rate range of 10^{-3} ~1/s. The homologous temperature range corresponding to the temperature range of 533~653K is 0.58~0.71. Figure.2.3 shows the schematic representation of thermo-mechanical process. A graphite type lubricant was used to reduce the friction between the specimen and the loading platen. All the specimens were compressed to a true strain of 1.2 and then quenched in water so as to retain the developed microstructure. The temperature ascended at the rate of 278K/s and the soaking time was 3 min. The true stress-strain curves were drawn immediately by computer with signals received by a strain-sensor during hot compression.

Chapter 3. Numerical procedures

3.1 FEM simulation of extrusion process

A non-isothermal three-dimensional finite element simulation of the indirect extrusion process was carried out by using the commercial rigid-plastic software DEFORM-3D V11.0 to obtain the macroscopic deformation behavior such as the temperature, strain rate and strain evolution during extrusion. The schematic representation of the extrusion simulation procedure is presented in Figure 3.1. The material for extrusion tooling, which was composed of die, container and ram, was the H13 hot-work tool steel. The assembly of the meshed billet, die, ram and container was constructed as shown in Figure 3.2. The extrusion simulation was performed at a reduction ratio 25:1 at the ram speed 0.8 cm/min for ZAM631 alloy rod (16Φ) and at a reduction ratio 56:1 at the ram speed 1.2 cm/min for AZ31 alloy plate (3t) at the temperature range of 533~653K. The initial billet had a diameter of 120 mm and a length of 80 mm. The FEM mesh was generated automatically within the space domain that included billet, die, ram and container. The re-meshing was also conducted automatically to accommodate large deformation and to consider the severely distorted meshes caused by the extensive deformation underwent during extrusion [60]. In order to reduce the computational time, only a quarter model was used considering the rotational symmetry in geometry and loading condition [61-62]. The process parameters used are listed in Table 3.1. The friction among the billet, die and container was modeled with the Coulomb friction law. The flow stress model was implemented as a function of plastic strain, strain rate and temperature defined by compression stress-strain curves measured using a Gleeble machine at the temperature range of 533~653K. We developed the user subroutines based on the flow stress model to describe the flow behavior of AZ31 and ZAM631

alloy during extrusion. The user subroutines were compiled by Absoft 11.0 Fortran compiler and then employed into DEFORM-3D system. These were presented in the Appendix A and B.

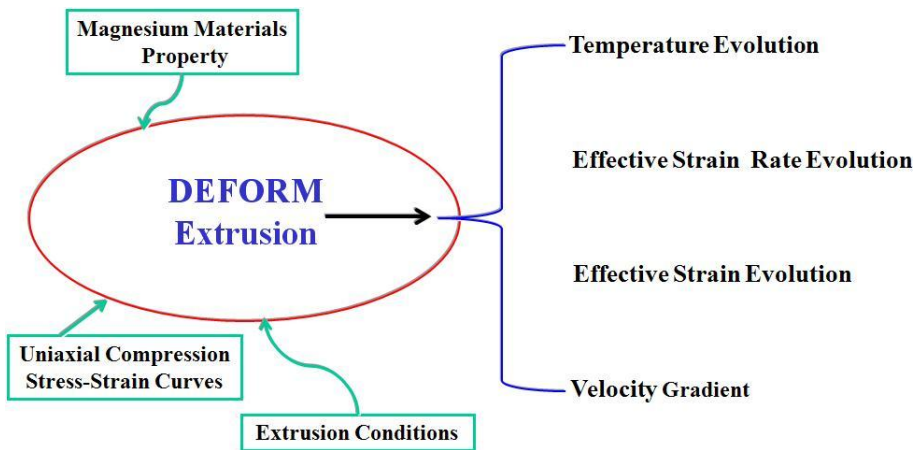


Figure 3.1 Schematic representation of the extrusion simulation procedure in DEFORM software.

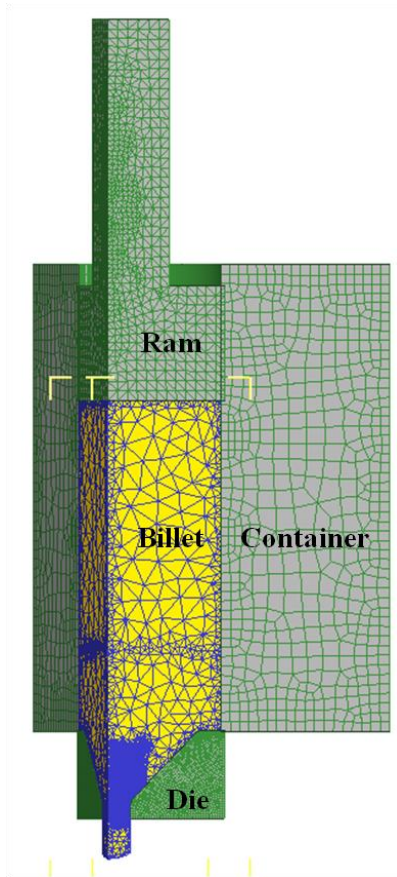


Figure 3.2 Assembly of the meshed billet, die, ram and container for extruded rod (16Φ) simulation.

Table 3.1 Process parameters used in the extrusion process simulation

Simulation Parameters		Workpiece Parameters	
Mode	Deformation	Material	AZ31, ZAM631
	Heat Transfer	No. of Elements	32,000
Extrusions	Rod, Plate	Tool Parameters	
Geometry	Axisymmetric	Material of Ram	H-13 tool steel
Process Parameters		Material of Die	H-13 tool steel
Ram Speed	AZ31 : 0.2 mm/s, ZAM631 : 0.13 mm/s	Material of Container	H-13 tool steel
Temperature	533~653K	Die Angle	45°
Environment Parameters		Tool-Workpiece Interaction	
Temperature	298K	Shear Friction Factor	0.3
Convection Coeff.	0.02 N/°Csmm ²	Heat Transfer Coeff.	11 N/°Csmm ²

3.2 Prediction of texture evolution

The macroscopic variables in FEM model for extrusion process are not enough to predict quality of extruded product which is more strongly related to the microscopic variables such as slip activity and texture change. The VPSC model can predict microscopic evolution but only with simple loading condition at constant temperature. To monitor microscopic behavior during the non-isothermal extrusion process new methodology was designed to connect macroscopic deformation history to the microscopic model, VPSC. The schematic flow chart for new methodology is presented in Figure 3.3.

The macroscopic flow stress-strain curves were obtained by conducting uniaxial compression tests under the considered extrusion deformation conditions. Then, the uniaxial compression test data were used to obtain microscopic material properties in VPSC model. The number of parameters for VPSC model could be more than 50 depending on the number of slip and twinning modes considered. Therefore optimization technique, Genetic Algorithm (GA), was used to find optimum material parameters to fit uniaxial compression test. The VPSC-GA optimizations were conducted with the randomly distributed initial texture measured by XRD. 1,000 grains were used to represent the initial texture. The fitting was performed by varying input range of the parameters at the range of 0~fully high values to find the optimal CRSS parameter sets. If the first CRSS parameter set was found, then, the optimizations were performed 3~4 times repeatedly by reducing the input range of parameters on the basis of the CRSS parameter set found. During calculations five deformation modes were considered to be active per grain i.e. basal $\langle a \rangle$ slip, prismatic $\langle a \rangle$ slip, second order pyramidal $\langle c+a \rangle$ slip, tensile twin and compressive twin.

The macroscopic response, velocity gradient and temperature were extracted from previously simulated DEFORM database using data extraction function and time saved sequentially. Any point can be selected to extract

macroscopic response. The VPSC-FE subroutine provided by VPSC7 released year 2007 is modified to accommodate different CRSS parameter sets at different temperature. Now sequential loading is applied on the microstructure to update the shape, the orientation and the hardening of the individual grains during extrusion process. The nearest temperature CRSS set is selected for each step with given temperature. In this study, 4 set of CRSS parameters are generated for each temperatures using VPSC-GA and applied VPSC-FE model. In order to represent the initial and predicted texture, 1,000 grains were used. The initial texture, which was measured by XRD, was randomly distributed.

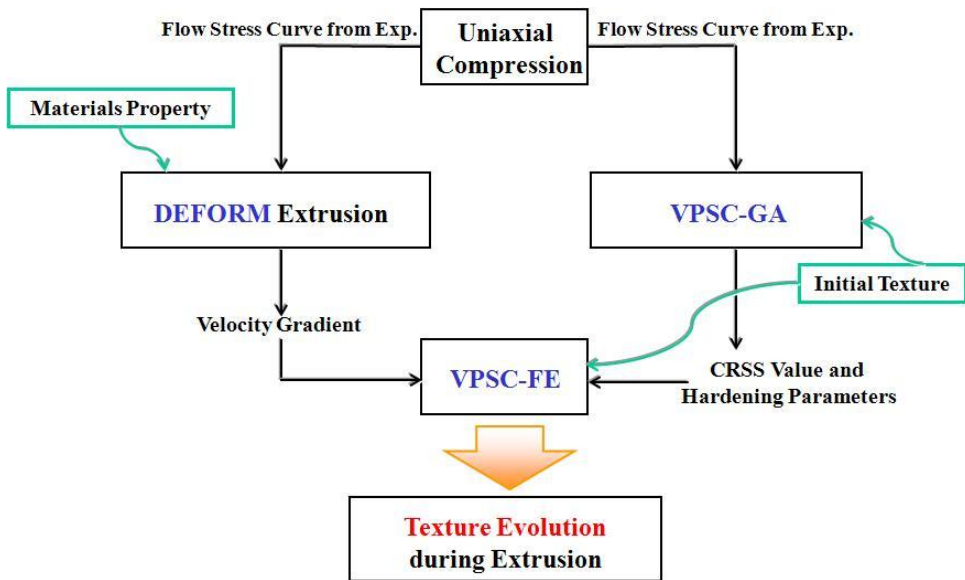


Figure 3.3 Schematic flow chart for prediction of texture evolution during extrusion process.

Chapter 4. Results and discussion

4.1 Crystal plasticity analysis of magnesium alloys

4.1.1 Effects of temperature on CRSS for slip and twinning modes in AZ31 alloy

The VPSC-GA optimizations were carried out to find microscopic material properties of AZ31 alloy with the randomly distributed initial texture measured by XRD. The experimental and simulated flow stress curves were compared. The simulated flow stress curves were in good agreement with the experimental results, as shown in Figure 4.1. Figure 4.2 shows the evolution of the relative activities of five deformation modes during compressive deformation at four different temperatures. During compressive deformation, the basal $\langle a \rangle$ slip and tensile twin were mainly activated. The contribution of the basal $\langle a \rangle$ slip decreased and that of the tensile twin decreased with increasing temperature. As the compressive deformation proceeded, most of the compressive deformations were mainly accommodated by the basal $\langle a \rangle$ slip.

The best-fitted CRSS values and hardening parameters obtained from the VPSC-GA optimizations are listed in Table 4.1. Table 4.1 shows that the basal $\langle a \rangle$ slip and tensile twin have the lower CRSS values than those of other deformation modes at four different temperatures. The basal $\langle a \rangle$ slip has the lowest CRSS values, ranging from 7.914 to 10.029 MPa and the values decreased with increasing temperature from 533 to 653K. The tensile twin has a CRSS value 1.5~2.1 times higher than those of basal $\langle a \rangle$ slip. Similarly, the prismatic $\langle a \rangle$ slip has 3.5~8.3 times higher and the $\langle c+a \rangle$ slip has 7.7~20.6 times higher. The compressive twin has a CRSS value much higher 24.0~32.3 times. The CRSS values decreased with increasing temperature in all

deformation modes. The CRSS values of the prismatic $\langle a \rangle$ slip, $\langle c+a \rangle$ slip and compressive twin were strongly dependent on temperature, whereas the basal $\langle a \rangle$ slip and tensile twin were weakly dependent on temperature.

The deformation mechanisms of magnesium and its alloys that are operative at low strain rates have been extensively investigated over the past years [63-65]. Although widely spread values have been reported for the CRSS values in different slip and twinning systems [66-68], It is generally accepted that, for polycrystals, $CRSS_{\text{basal}} < CRSS_{\text{tensile twin}} < CRSS_{\text{prismatic}} \leq CRSS_{\text{pyramidal}}$ [69]. The investigated CRSS values have shown the same trend.

The CRSS values and hardening parameters of pure magnesium single crystal are listed in table 4.2 [70]. The CRSS values obtained from VPSC-GA optimizations were compared with those of pure magnesium single crystal in Figure 4-3 (a). The CRSS values of AZ31 alloy were much higher than those of pure magnesium single crystal. Despite the difference in the magnitude, the relative decrease in the CRSS values was similar to that reported for pure magnesium single crystal over the observed temperature range.

For all deformation modes, the CRSS values were normalized by the CRSS values of basal $\langle a \rangle$ slip. The normalized CRSS values were compared with those of pure magnesium single crystal in Figure 4-3 (b). The normalized CRSS values of $\langle c+a \rangle$ slip were slightly higher than those of pure magnesium single crystal, whereas the normalized CRSS values of other non-basal (prismatic, tensile twin and compressive twin) deformation modes were lower than those of pure magnesium single crystal to ~ 2.989 .

Table 4.1 Best-fit model parameters for AZ31 alloy describing the CRSS and hardening responses of the five deformation behaviors as a function of temperature.

Mode	Voce Hardening	533K	573K	613K	653K
Basal <a>	τ_0	10.029	9.548	7.945	7.914
	τ_1	46.449	23.204	22.129	10.167
	θ_0	17.708	9.138	3.015	3.982
	θ_1	4.694	2.512	1.156	0.279
	h^{ss}	1	1	1	1
Prism. <a>	τ_0	83.254	52.727	39.849	28.029
	τ_1	118.990	58.839	42.356	13.940
	θ_0	230.790	106.010	72.989	28.031
	θ_1	72.693	50.968	30.804	18.783
	h^{ss}	1	1	1	1
<c+a>	τ_0	206.550	154.840	68.358	60.635
	τ_1	172.120	156.800	67.268	58.874
	θ_0	241.170	169.320	86.529	29.071
	θ_1	74.624	51.584	46.525	22.299
	h^{ss}	1	1	1	1
Tensile Twin	τ_0	20.716	17.826	13.224	12.252
	τ_1	77.185	28.188	27.239	9.650
	θ_0	207.030	94.922	57.440	28.000
	θ_1	45.919	46.911	17.206	3.542
	h^{ss}	3	3	3	1
Compressive Twin	τ_0	324.020	286.040	193.220	189.910
	τ_1	231.230	198.350	135.400	98.358
	θ_0	294.200	145.280	141.350	68.991
	θ_1	169.120	89.684	53.161	31.022
	h^{ss}	1	1	1	1

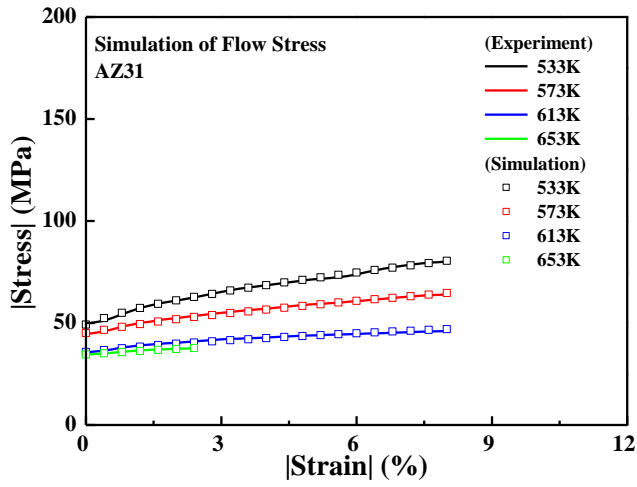


Figure 4.1 Experimental and simulated uni-axial compression curves of AZ31 alloy.

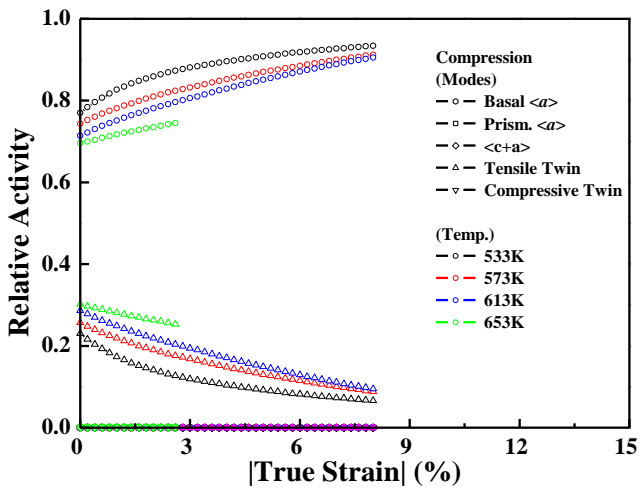


Figure 4.2 Relative activities of the five deformation modes during uni-axial compressive deformation of AZ31 alloy.

Table 4.2 Best-fit model parameters for pure magnesium single crystal describing the CRSS and hardening responses of the five deformation behaviors as a function of temperature [70].

Mode	Voce Hardening	533K	573K	613K	653K
Basal <a>	τ_0	0.489	0.405	0.368	0.324
	τ_1	0.106	0.081	0.020	0.074
	θ_0	58.410	25.414	11.712	8.714
	θ_1	5.644	3.909	2.218	1.290
	h^{ss}	1	1	1	1
Prism. <a>	τ_0	6.515	3.806	2.585	2.002
	τ_1	0.741	0.484	0.277	0.156
	θ_0	73.663	31.443	17.204	9.490
	θ_1	1.555	1.034	0.891	0.406
	h^{ss}	1	1	1	1
<c+a>	τ_0	10.188	6.256	3.243	2.156
	τ_1	3.204	1.130	0.842	0.693
	θ_0	144.950	32.359	24.823	18.925
	θ_1	15.411	11.712	4.111	2.959
	h^{ss}	1	1	1	1
Tensile Twin	τ_0	1.556	1.526	1.510	1.499
	τ_1	0.875	0.562	0.421	0.394
	θ_0	15.343	13.233	6.314	5.887
	θ_1	6.678	6.268	3.059	2.899
	h^{ss}	3	3	3	3
Compressive Twin	τ_0	30.418	24.700	16.700	11.784
	τ_1	8.942	4.254	2.746	1.075
	θ_0	146.400	48.945	30.195	23.355
	θ_1	25.524	13.803	7.992	4.186
	h^{ss}	1	1	1	1

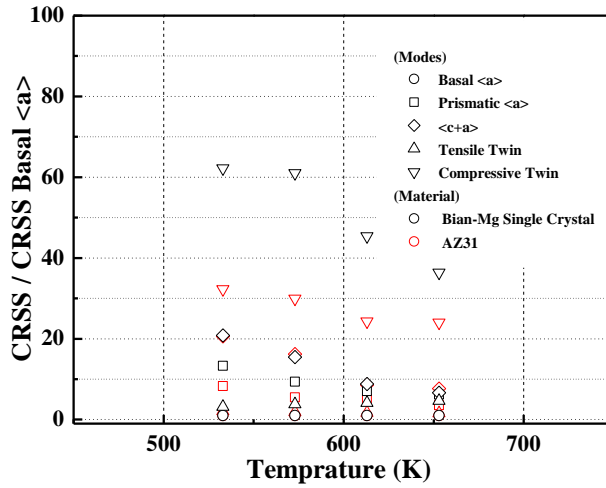
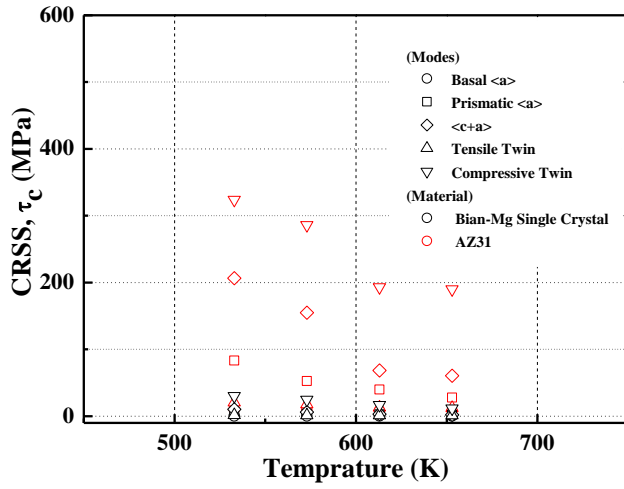


Figure 4.3 Comparison of CRSS values between AZ31 alloy and pure magnesium single crystal published data; (a) CRSS and (b) CRSS normalized by $CRSS_{\text{Basal}\langle a \rangle}$.

4.1.2 Effects of temperature on CRSS for slip and twinning modes in ZAM631 alloy

The VPSC-GA optimizations were carried out to find microscopic material properties of ZAM631 alloy with the randomly distributed initial texture measured by XRD. The experimental and simulated flow stress curves were compared. The simulated flow stress curves were in good agreement with the experimental results, as shown in Figure 4.4. Figure 4.5 shows the evolution of the relative activities of five deformation modes during compressive deformation at two different temperatures. During compressive deformation, the basal $\langle a \rangle$ slip and tensile twin were mainly activated at 533K. The contribution of the basal $\langle a \rangle$ slip decreased and that of the tensile twin decreased with increasing temperature. On the contrary, the $\langle c+a \rangle$ slip and basal $\langle a \rangle$ slip were mainly activated at 613K during compressive deformation.

The best-fitted CRSS values and hardening parameters obtained from the VPSC-GA optimizations are listed in Table 4.3. Table 4.3 shows that the predominant deformation mode have changed from the basal $\langle a \rangle$ slip to the non-basal $\langle c+a \rangle$ slip as the temperature was increasing from 533K to 613K. This result shows well the activation of the non-basal slip with the rise in temperature. The CRSS values of the basal $\langle a \rangle$ slip decreased slightly with increasing temperature from 533 to 613K. On the contrary, those values of the $\langle c+a \rangle$ slip decreased drastically with the rise in temperature. The CRSS values of the prismatic $\langle a \rangle$ slip, $\langle c+a \rangle$ slip and compressive twin were strongly dependent on temperature, whereas the basal $\langle a \rangle$ slip and tensile twin were weakly dependent on temperature.

The CRSS values obtained from VPSC-GA optimizations were compared with those of pure magnesium single crystal in Figure 4-6 (a). The CRSS values of ZAM631 alloy were much higher than those of pure magnesium single crystal.

For all deformation modes, the CRSS values were normalized by the CRSS values of basal $\langle a \rangle$ slip. The normalized CRSS values were compared with those of pure magnesium single crystal in Figure 4-6 (b). The normalized CRSS value of $\langle c+a \rangle$ slip was slightly higher than that of pure magnesium single crystal at 533K but was much lower than that of pure magnesium single crystal at 613K. The normalized CRSS values of other non-basal (prismatic slip, tensile twin and compressive twin) deformation modes were lower than those of pure magnesium single crystal to ~ 1.982 .

Table 4.3 Best-fit model parameters for ZAM631 alloy describing the CRSS and hardening responses of the five deformation behaviors as a function of temperature.

Mode	Voce Hardening	533K	613K
Basal <a>	τ_0	13.243	12.126
	τ_1	45.354	12.252
	θ_0	3.475	44.981
	θ_1	2.252	14.848
	h^{ss}	1	1
Prism. <a>	τ_0	163.410	74.097
	τ_1	168.460	49.757
	θ_0	206.950	76.727
	θ_1	88.862	13.736
	h^{ss}	1	1
<c+a>	τ_0	305.610	7.703
	τ_1	266.510	0.361
	θ_0	249.960	27.250
	θ_1	108.780	0.579
	h^{ss}	1	1
Tensile Twin	τ_0	24.768	28.011
	τ_1	114.150	38.497
	θ_0	188.080	32.479
	θ_1	42.490	22.098
	h^{ss}	3	3
Compressive Twin	τ_0	561.420	277.650
	τ_1	324.960	100.770
	θ_0	412.070	42.813
	θ_1	146.830	11.113
	h^{ss}	1	1

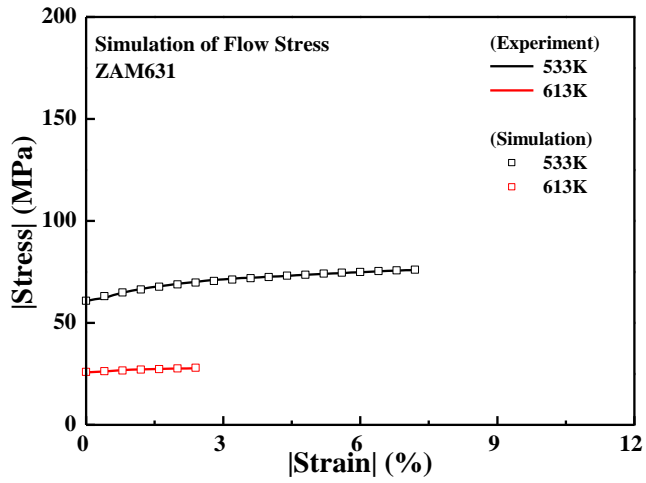


Figure 4.4 Experimental and simulated uni-axial compression curves of ZAM631 alloy.

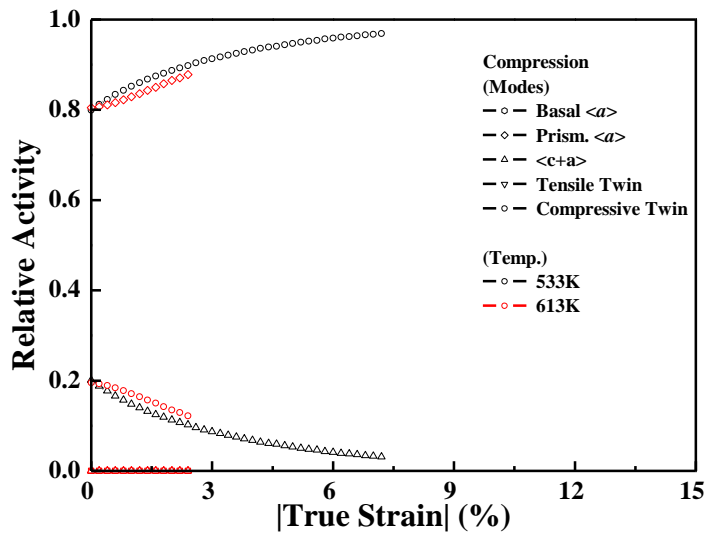
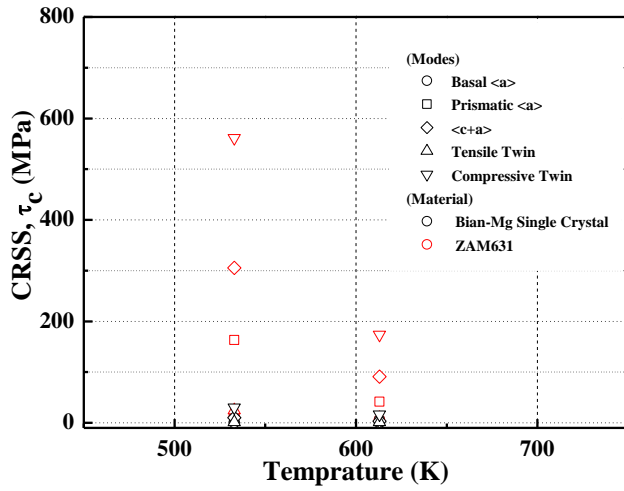
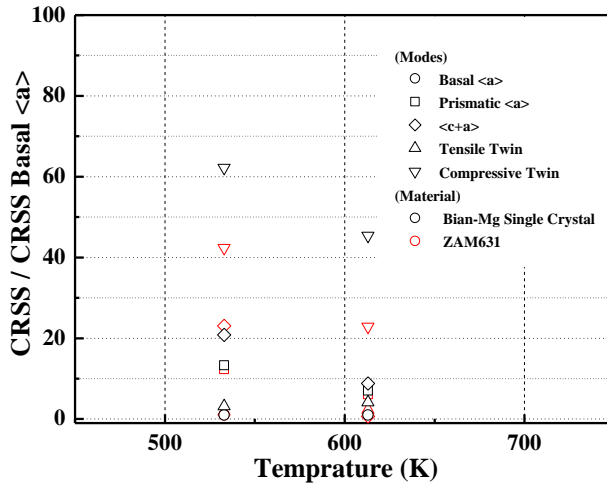


Figure 4.5 Relative activities of the five deformation modes during uni-axial compressive deformation of ZAM631 alloy.



(a)



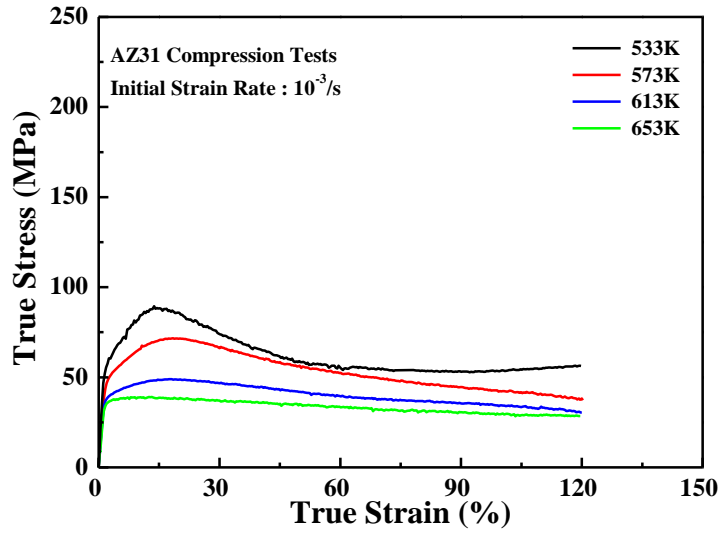
(b)

Figure 4.6 Comparison of CRSS values between ZAM631 alloy and pure magnesium single crystal published data; (a) CRSS and (b) CRSS normalized by $CRSS_{\text{basal}\langle a \rangle}$.

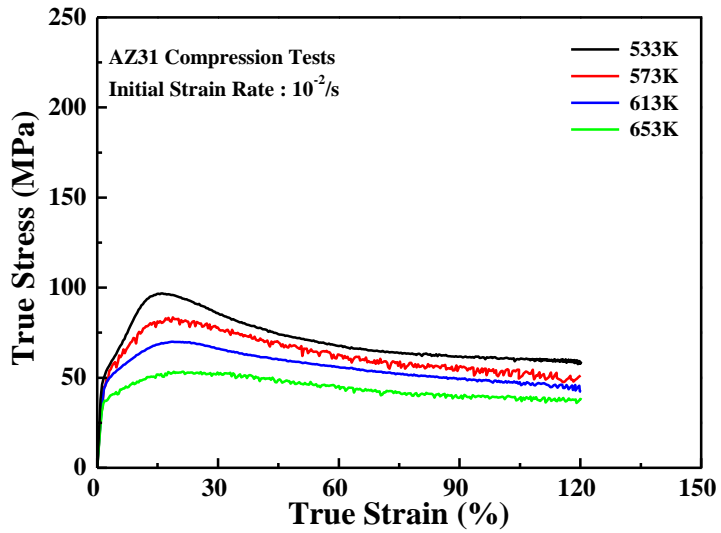
4.2 Hot deformation behavior of AZ31 alloy

4.2.1 Flow stress behavior

Figure 4.7 shows the stress-strain curves of AZ31 alloy under various deformation conditions. The general characteristics of the flow stress curves were similar under all deformation conditions. The flow stress increased to a peak (initial strain hardening) and then decreased to a steady state. With decreasing strain rate or increasing temperature, the strain hardening effect becomes weaker. As a result, the peak stress varies according to deformation conditions, so does the peak strain. Under a constant strain rate, the peak stress and the peak strain increased with decreasing temperature. Under a constant temperature, the peak stress and the peak strain increased with increasing strain rate. Owing to dynamic recovery (DRV) and DRX, wrought magnesium alloys show distinct high temperature softening. Material response can principally be divided into two categories in hot deformation: DRV type and DRX type. For metal with DRV, the flow stress curves increase with strain in the initial deformation and reach constant in consequence of attaining the balance between work hardening and DRV. For metal with DRX, initially the flow stress increases with strain due to being dominated by work hardening, and as DRX takes place upon critical strain, the flow stress begins to decrease after it reaches certain peak value. When the equilibrium is reached between softening due to DRX and work hardening, the curves drop to a steady-state region. For AZ31 alloy, DRX is the typical characteristic of flow stress curves [10]. DRX which can reduce the dislocation density and release the accumulated energy to facilitate straining [68] can easily occur during extrusion process on magnesium alloys, resulting in refined grains and improvement in mechanical properties [69].

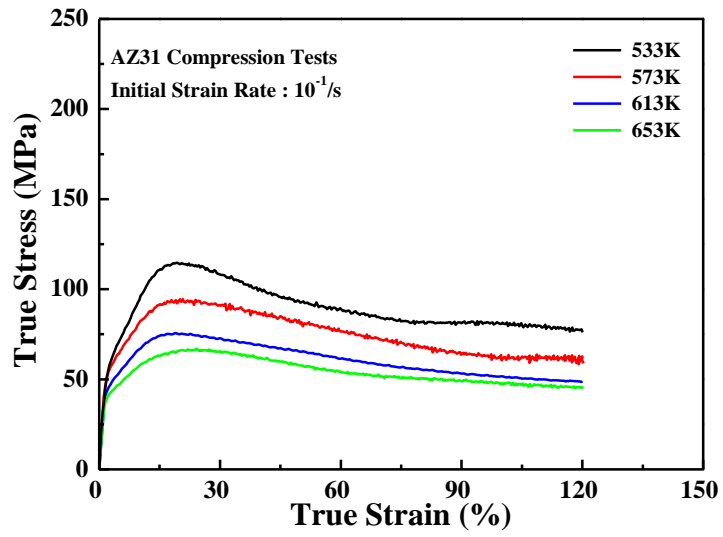


(a)

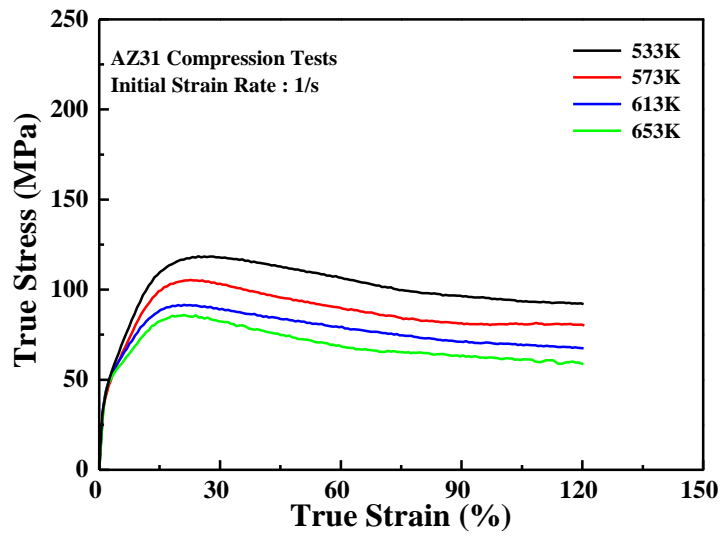


(b)

Figure 4.7 True stress-true strain curves of AZ31 alloy at different strain rates; (a) $10^{-3}/s$, (b) $10^{-2}/s$, (c) $10^{-1}/s$ and (d) $1/s$.



(c)



(d)

Figure 4.7 Continued.

4.2.2 Microstructures

The microstructure evolutions of compressed AZ31 alloy corresponding to the various deformation conditions (temperatures, strain rate and strain) are shown in Figures 4.8~4.11. The observed planes of specimens were parallel to the compression direction. The microstructures indicate that DRX occurs evidently during hot compression. The grains were broken and elongated. The grain boundaries were being serrated and this serration as well as elongation of grains increased with increasing strain. Twinning was occurred extensively in the initial stage of DRX at the strain rate range of 10^{-2} ~1/s under constant temperature. In the initial stage of DRX, the formation of a limited number of new small grains was observed. More new small grains were formed with deformation to higher strain. With increasing strain beyond the peak, most of the pre-existing boundaries were decorated by these new DRX grains. DRX is classified into either continuous or discontinuous one. In general continuous recrystallization is considered as a recovery process where a progressive increase in boundary misorientation and the conversion of low angle boundaries into the high angle ones may be realized. This type of recrystallization can be accompanied with gradual softening in the flow curve ending to a plateau in true stress-true strain curves [71-72]. Discontinuous recrystallization involves the nucleation of new grains, typically at pre-existing grain boundaries, followed by growth, which cause a significant softening in flow curve [72]. Accordingly, in this study, it can be deduced that discontinuous dynamic recrystallization (DDRX) is predominant at all deformation conditions.

The grain size and the volume fraction of DRX are dependent sensitively on deformation temperature and /or strain rate [73]. Tables 4.4 and 4.5 show the grain size and the volume fraction under the various deformation conditions. These observations reveal that the microstructural behaviors could be related to the Zener-Hollomon parameter Z , which is defined as [74]:

$$Z = \dot{\epsilon} \exp [Q / (RT)] \quad (4.1)$$

Where $\dot{\epsilon}$ = strain rate, T = the absolute temperature, Q = the apparent activation energy for deformation, and R = the gas constant.

Figure 4.12 shows average DRX grain size under various deformation conditions. Average DRX grain size increased with increasing deformation temperature. Figure 4.13 shows the relationship between average DRX grain size and $\ln Z$. Average DRX grain size exhibit linear dependency on $\ln Z$ as following:

$$D_{\text{drx}} = 158.077 Z^{-0.111} \quad (4.2)$$

Table 4.6 shows the $\ln Z$ values under various deformation conditions. The volume fraction and DRX grain size decrease with increasing Z value, that is to say decreasing deformation temperature or increasing strain rate. A high Z value leads to a lower DRX kinetics because of lower diffusivity at lower temperatures and/or insufficient time at higher strain rates. As there is not enough time for diffusion to take place at high strain rates, the grain growth is not so pronounced. As a result, the growth of new DRX grains was limited, thereby reducing the size of DRX grains [72].

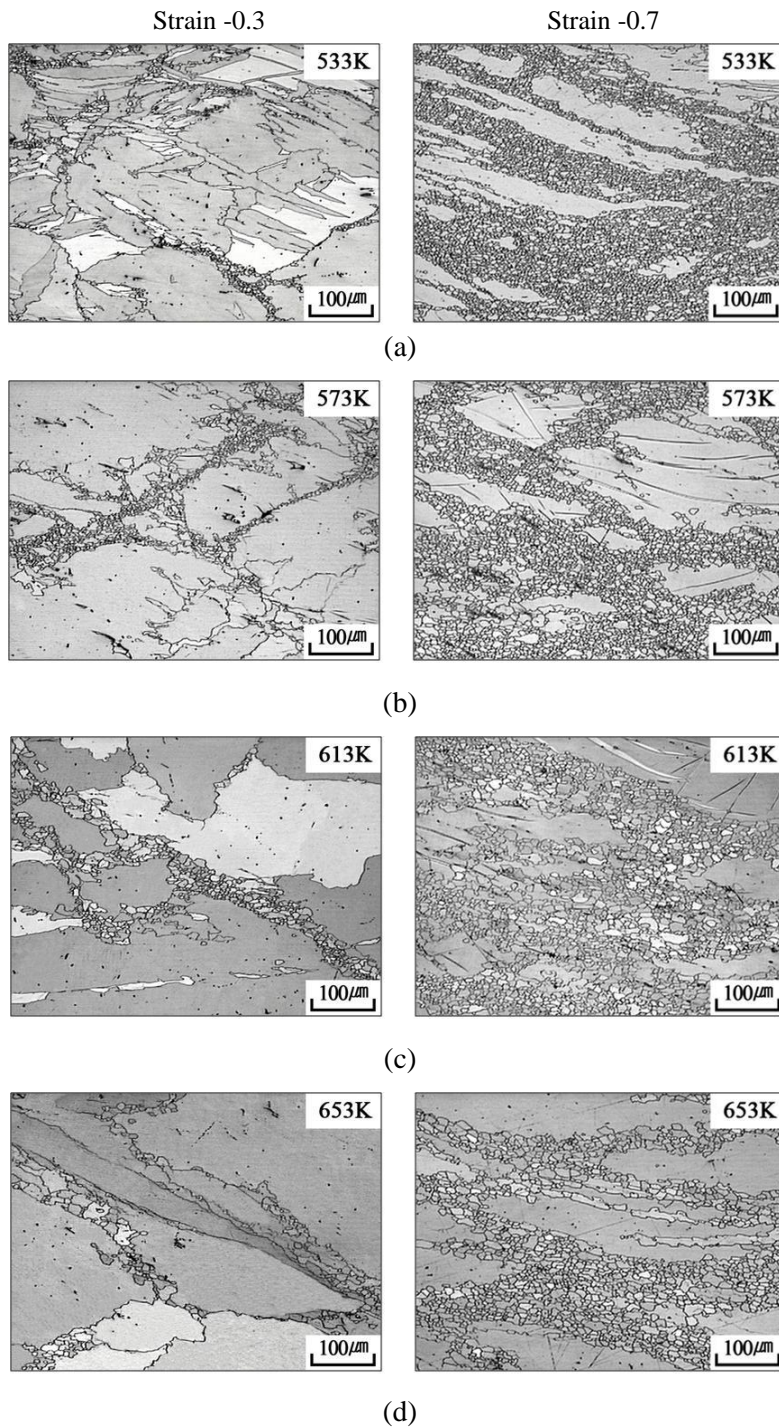


Figure 4.8 Microstructures of AZ31 alloy compressed at a strain rate $10^{-3}/s$ at a strain -0.3 and -0.7; (a) 533K, (b) 573K, (c) 613K and (d) 653K.

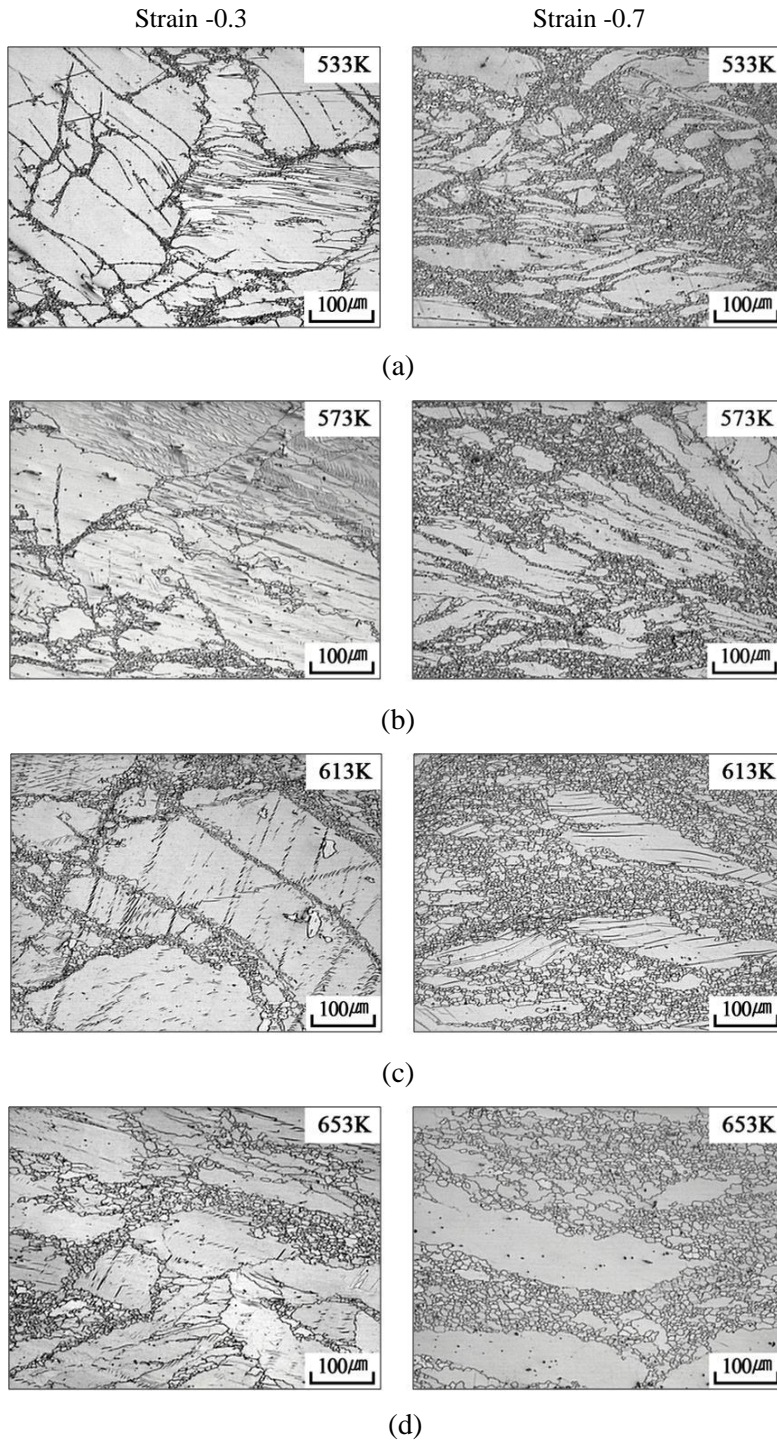


Figure 4.9 Microstructures of AZ31 alloy compressed at a strain rate $10^{-2}/s$ at a strain -0.3 and -0.7; (a) 533K, (b) 573K, (c) 613K and (d) 653K.

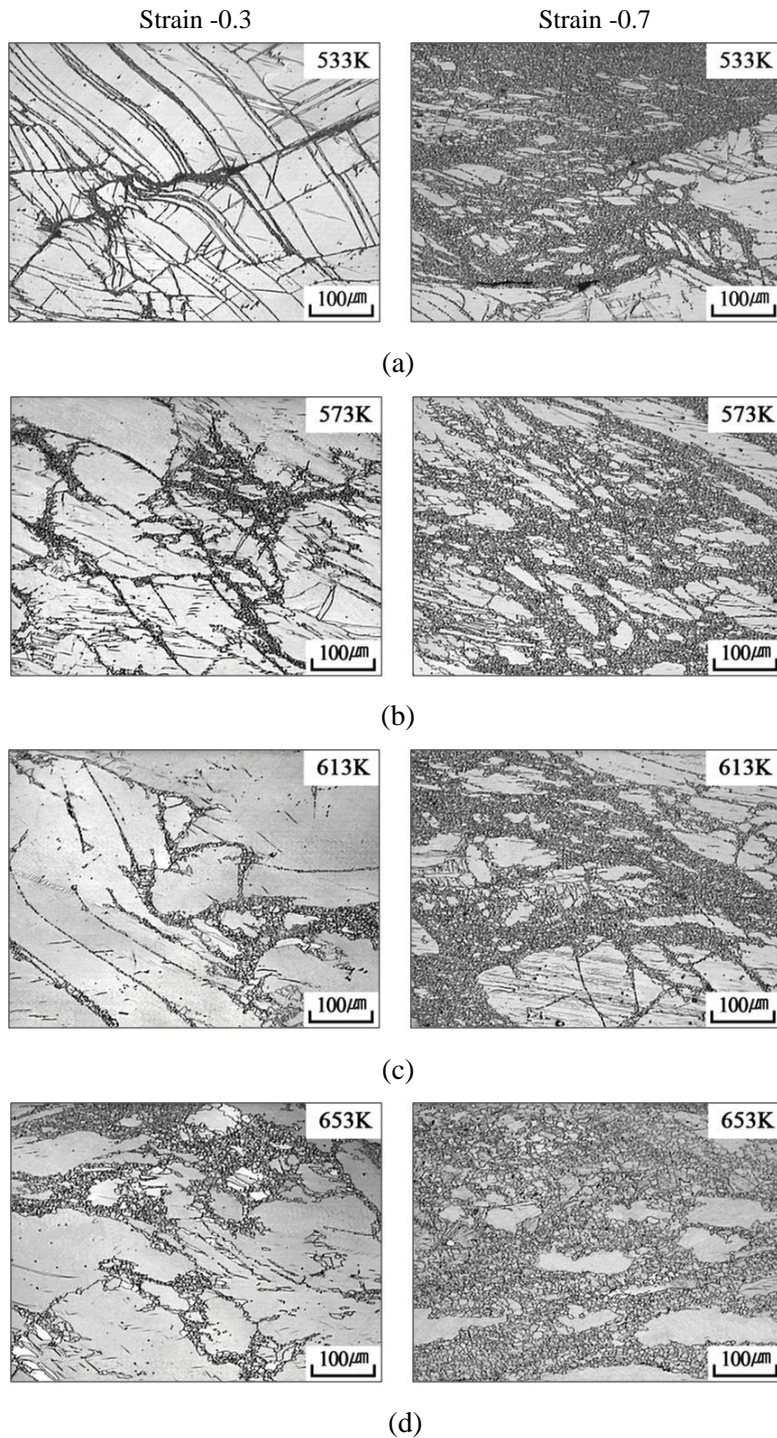


Figure 4.10 Microstructures of AZ31 alloy compressed at a strain rate $10^{-1}/s$ at a strain -0.3 and -0.7; (a) 533K, (b) 573K, (c) 613K and (d) 653K.

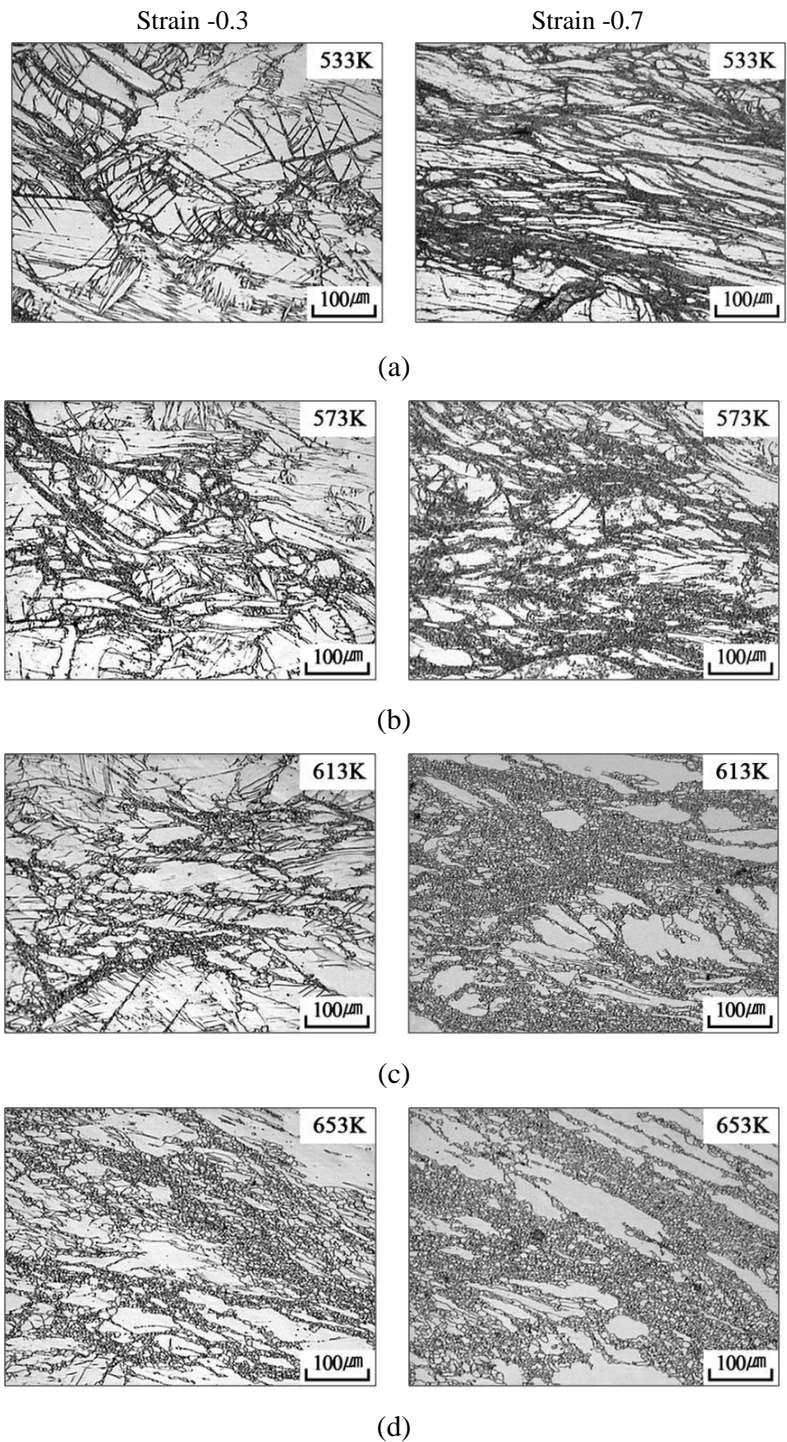


Figure 4.11 Microstructures of AZ31 alloy compressed at a strain rate 1/s at a strain -0.3 and -0.7; (a) 533K, (b) 573K, (c) 613K and (d) 653K.

Table 4.4 Average DRX grain size (D_{drx}) of AZ31 alloy at a strain -0.7.

Strain rate (/s)	Temperature (K)	D_{drx} (μm)
$10^{-3}/\text{s}$	533	3.111
	573	4.574
	613	6.018
	653	8.643
$10^{-2}/\text{s}$	533	2.800
	573	3.654
	613	4.581
	533	5.308
$10^{-1}/\text{s}$	533	1.976
	573	2.226
	613	3.338
	533	4.406
1/s	533	1.730
	573	1.968
	613	2.118
	533	2.961

Table 4.5 DRX volume fraction (X_{DRX}) of AZ31 alloy at a strain -0.7.

Strain rate (/s)	Temperature (K)	X_{DRX} (%)
$10^{-3}/\text{s}$	533	59.086
	573	62.781
	613	64.506
	653	69.020
$10^{-2}/\text{s}$	533	47.605
	573	49.276
	613	52.943
	533	61.242
$10^{-1}/\text{s}$	533	34.843
	573	41.366
	613	46.767
	533	52.512
1/s	533	28.858
	573	41.147
	613	46.406
	533	48.945

Table 4.6 $\ln Z$ values of AZ31 alloy under different deformation conditions.

Strain rate (/s)	Temperature (K)	$\ln Z$ (/s)
$10^{-3}/s$	533	35.297
	573	32.351
	613	29.789
	653	27.541
$10^{-2}/s$	533	37.600
	573	34.653
	613	32.092
	533	29.844
$10^{-1}/s$	533	39.902
	573	36.956
	613	34.394
	533	32.146
1/s	533	42.205
	573	39.259
	613	36.697
	533	34.449

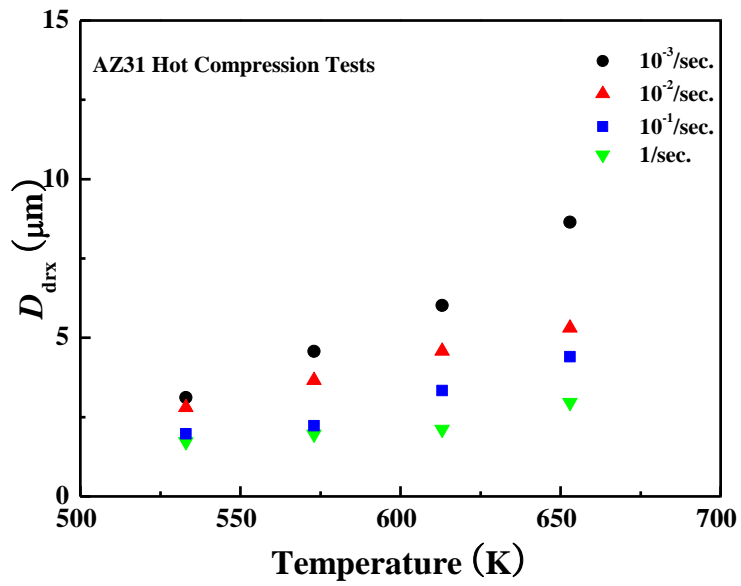


Figure 4.12 Average DRX grain (D_{drx}) size of AZ31 alloy compressed at various strain rates at a strain -0.7.

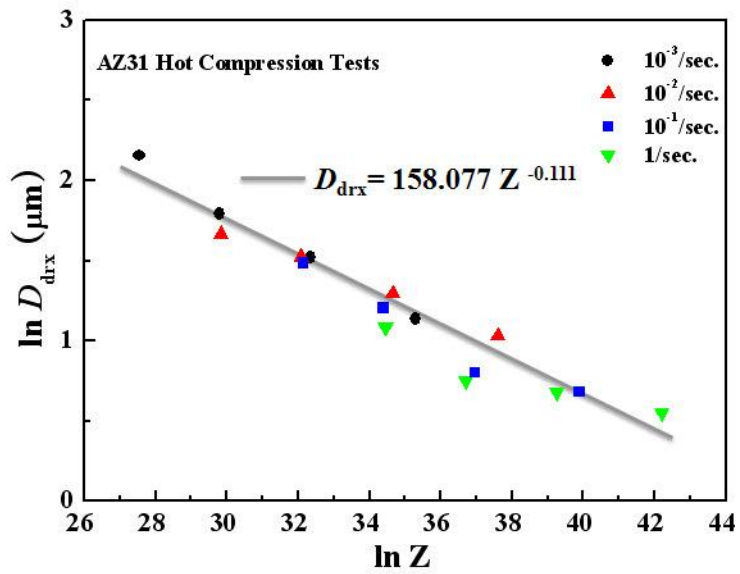


Figure 4.13 Relation between average DRX grain (D_{drx}) size and Zener-Hollomon parameter of AZ31 alloy.

4.2.3 Modeling of flow stress

Computer simulation of metal forming processes enables, hitherto not possible, obtaining a process model that is closer to the real conditions [75]. Two methods can be used to build flow stress equation. One is based on deformation mechanism from the microstructure's point of view such as dislocation density and grain size. The other is based on macroscopic mechanical behavior i.e., flow stress curve, thus the flow stress equation results from regression analysis of test data [10].

The mechanical properties of the workpiece under hot working are generally expressed by a constitutive equation, which connects the flow stress to the variables such as strain, strain rate, temperature and microstructures. In order to understand and control the hot working process, setting up a constitutive equation for DRX is needed [76].

4.2.3.1 Determination of peak stress

In hot deformation of AZ31 alloy, the atomic diffusibility and the driving force of dislocation migration are dependent on the temperature; the dislocation density and the accumulation of grain boundary energy are dependent on the strain rate. Therefore, the peak stress can be considered depending only on the temperature and strain rate, and taken as the function of the Zener-Hollomon parameter Z [10]. Z and σ obey the relation as follows :

$$Z = A [\sinh(\alpha\sigma)]^n \quad (4.3)$$

Following the previous works [10], the peak stress under hot working was derived with the aid of the following relations. The hot working favored the power law at the high stress level and the equation is presented as follows:

$$Z = A_1 \sigma^n \quad (4.4)$$

The favorite equation is the exponent law at the low stress level, which is given by

$$Z = A_2 \exp(\beta \sigma) \quad (4.5)$$

Assuming the value of n' equals n , the approximate value of n can be taken as the slope of the plot of $\ln \dot{\epsilon}$ versus $\ln \sigma$ at the low stress level. It can be seen by comparing Eq. (4.1) with Eq. (4.5) that A is equal to $A_2/2^n$ and the value of α is approximately equal to β/n . The value of A_2 and β can be determined corresponding to the $\ln \dot{\epsilon}$ versus σ plot at the high stress level. The value of Q is calculated in the following equation:

$$Q = R \left[\frac{\partial(\ln(\sinh(\alpha\sigma)))}{\partial(1/T)} \right]_{\dot{\epsilon}} \cdot \left[\frac{\partial(\ln \dot{\epsilon})}{\partial(\ln(\sinh(\alpha\sigma)))} \right]_T \quad (4.6)$$

The first term on the right-hand side of the above formula represents the slope of the $\ln(\sinh(\alpha\sigma_p))$ versus $1/T$ plot and the second term represents the reciprocal value of inclination of the $\ln(\sinh(\alpha\sigma_p))$ versus $\ln \dot{\epsilon}$ plot.

The approximate value of n is 13.117 corresponding to Figure 4.14 (a) and that of β is 0.179 corresponding to Figure 4.14 (b). So, the suitable value of α is 0.014. The average value of slope of the $\ln(\sinh(\alpha\sigma_p))$ versus $1/T$ is approximately 2.275×10^3 corresponding to Figure 4.14 (c). The reciprocal value of inclination of the $\ln(\sinh(\alpha\sigma_p))$ versus $\ln \dot{\epsilon}$ is approximately 9.887 corresponding to Figure 4.14 (d). So, the value of Q equals 187.025 kJ/mol. According to Eq. (4.3), the exact values of A and n are obtained from the $\ln(\sinh(\alpha\sigma_p)) - \ln Z$ plot. According to Figure 4.14 (e), the relationship of σ_p and Z is expressed as follows:

$$Z = \ln A + n (\sinh(\alpha\sigma_p)) \quad (4.7)$$

The σ_p is given by

$$\sigma_p = \frac{1}{\alpha} \cdot \left(\left(\frac{Z}{A} \right)^{\frac{1}{n}} + \left(\left(\frac{Z}{A} \right)^{\frac{2}{n}} + 1 \right) \right) \quad (4.8)$$

Where α is 0.014, n is 9.495, A is 9.452×10^{13} .

4.2.3.2 Determination of flow stress

Following the recent work of Liu et al. [10], the flow stress for reflecting DRX process under hot working was derived with the aid of the following relations between the peak strain (ε_p) and the peak stress (σ_p). The relationship of the difference of the flow stress at different strain and the peak stress with the increasing strain is considered. If the strain is multiplied by a certain coefficient ξ and all the variables are taken logarithm. In Figure 4.15, the x coordinate denotes ε ; the y coordinate represents the ratio of differences $\ln\sigma$ and $\ln\sigma_p$ to $\ln\xi\varepsilon$ (ξ is a specified coefficient) i.e., $(\ln\sigma - \ln\sigma_p)/\ln\xi\varepsilon$. The two order curves can be observed at various temperatures and strain rates. By means of Lagrange mean value theorem and least-square fitting, Figure 4.16 shows the dependence of the rate of change of $(\ln\sigma - \ln\sigma_p)/\ln\xi\varepsilon$ to strain at the corresponding strain. The linear relationship can be found at various temperatures and strain rates. The strain softening exponent is introduced. The definition is given by

$$\theta^* = \frac{\ln\sigma - \ln\sigma_p}{\ln\xi\varepsilon} \quad (4.9)$$

The relationship between θ^* and ε shows the two order curve. When the value of σ equals σ_p , the value of θ^* is minimum and its value equals 0. At this time, the value of ε is ε_p .

According to Figure 4.16, the linear relationship between $\partial\theta^*/\partial\varepsilon$ and ε can be observed, and therefore the expression is written as follows:

$$\partial\theta^*/\partial\varepsilon = k\varepsilon - b \quad (4.10)$$

When the value of θ^* is minimum, the value of $\partial\theta^*/\partial\varepsilon$ equals 0. Additionally, the minimum of θ^* corresponds to ε_p . As a result, ε_p equals b/k .

The integral of Eq. (4.10) is as follows:

$$\theta^* = (1/2k)(k\varepsilon - b)^2 + C \quad (4.11)$$

Where C is the constant. As the minimum of θ^* is zero when ε_p equals b/k , the value of C is equal to zero. The θ^* value can be given by

$$\theta^* = \frac{1}{2k}(k\varepsilon - b)^2 \quad (4.12)$$

Then, by Eq. (4.9)

$$\frac{\ln\sigma - \ln\sigma_p}{\ln\xi\varepsilon} = \frac{1}{2k}(k\varepsilon - b)^2 \quad (4.13)$$

The above formula can be expressed as follows:

$$\frac{\ln\sigma - \ln\sigma_p}{\ln\xi\varepsilon} = \frac{b^2}{2k} \left(\frac{\varepsilon - b/k}{b/k} \right)^2 \quad (4.14)$$

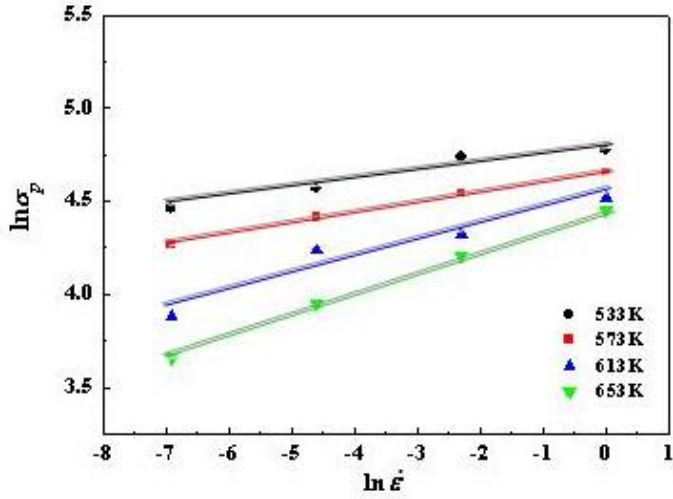
Substituting b/k by ε_p and $b^2/2k$ by η yields

$$\frac{\ln\sigma - \ln\sigma_p}{\ln\xi\varepsilon} = \eta \left(\frac{\varepsilon - \varepsilon_p}{\varepsilon_p} \right)^2 \quad (4.15)$$

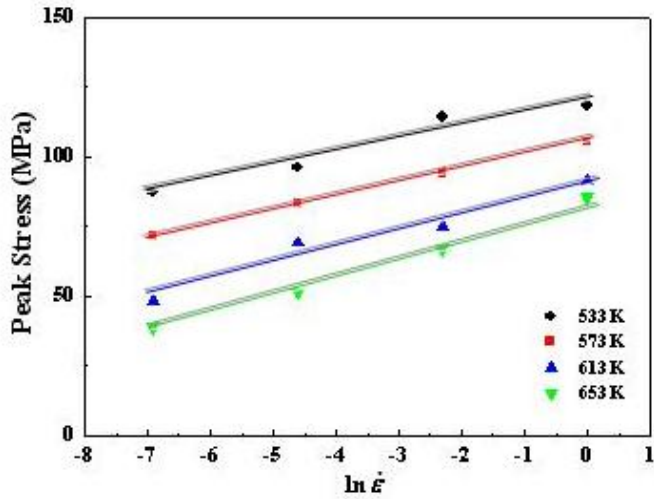
$$\ln\sigma = \Psi(\varepsilon - \varepsilon_p)^2 + \ln\sigma_p \quad (4.16)$$

where $\Psi = k/2$.

This model contains only two parameters which are ξ and Ψ . For multiple experimental values, the optimum values of two parameters obtained by the least-squares method are shown in Table 4.7. Figure 4.17 shows the comparison between model prediction results and experimental results of AZ31 alloy. The predicted results show good agreement with the experimental data. This flow stress model has been presented for the flow stress under various deformation conditions (strain, temperature and strain rate) and can be applied in the range of corresponding to the temperature between 533K and 653K, strain rate between $10^{-3}/s$ and $1/s$ and strain less than 1.

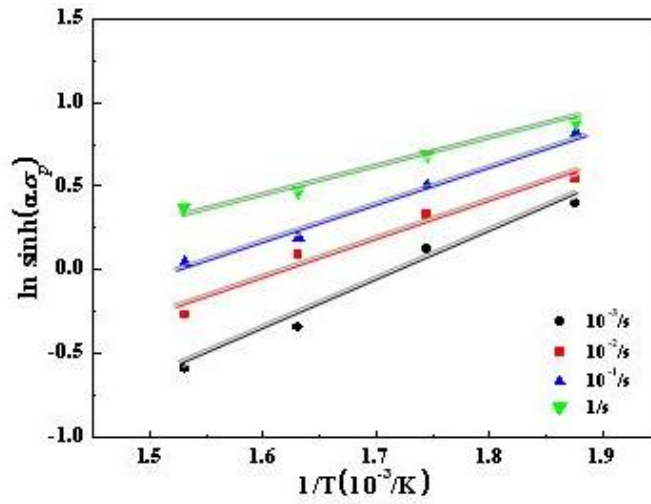


(a)

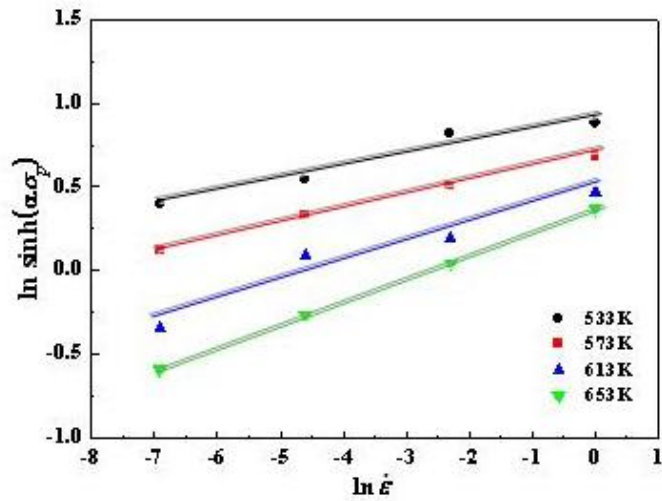


(b)

Figure 4.14 Schematic of the dependence of the peak stress of AZ31 alloy on temperature and strain rate; (a) schematic of $\ln \sigma_p$ versus $\ln \dot{\epsilon}$, (b) schematic of σ_p versus $\ln \dot{\epsilon}$, (c) schematic of $\ln(\sinh(\alpha \sigma_p))$ versus $1/T$, (d) schematic of $\ln(\sinh(\alpha \sigma_p))$ versus $\ln \dot{\epsilon}$, (e) schematic of $\ln(\sinh(\alpha \sigma_p))$ versus $\ln Z$ and (f) schematic of $\ln \epsilon_p$ versus $\ln Z$.

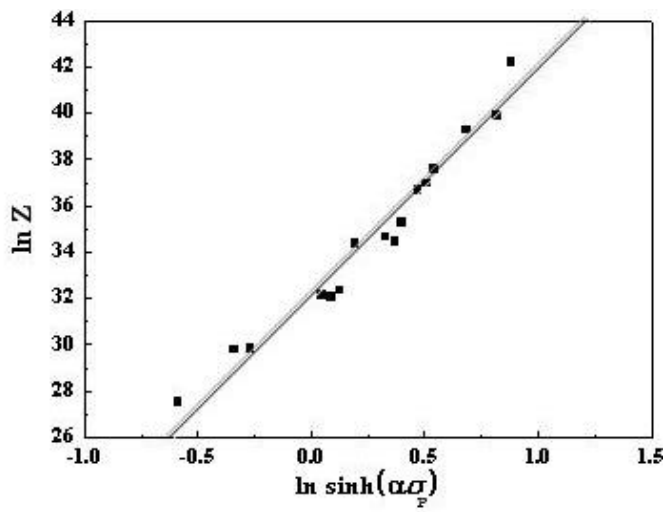


(c)



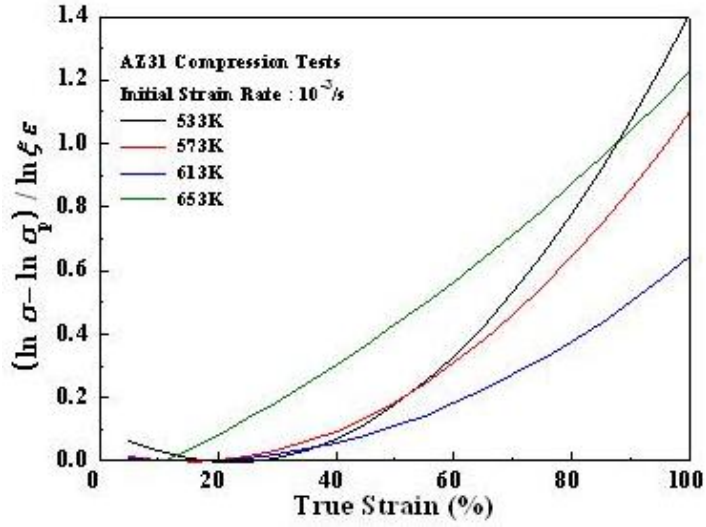
(d)

Figure 4.14 Continued.

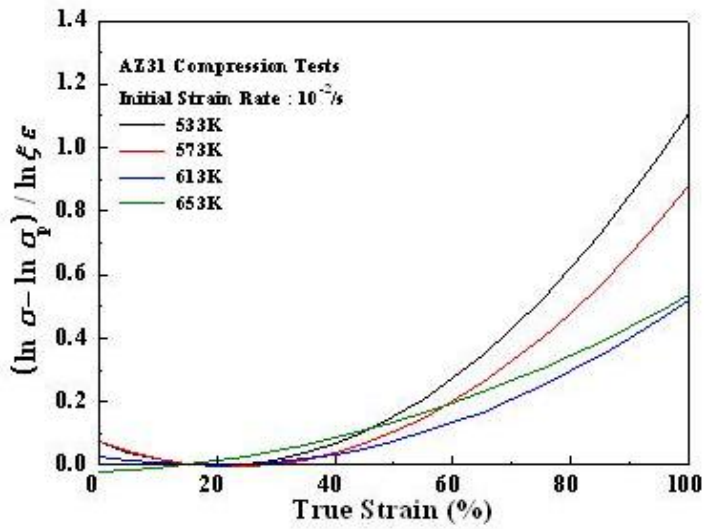


(e)

Figure 4.14 Continued.

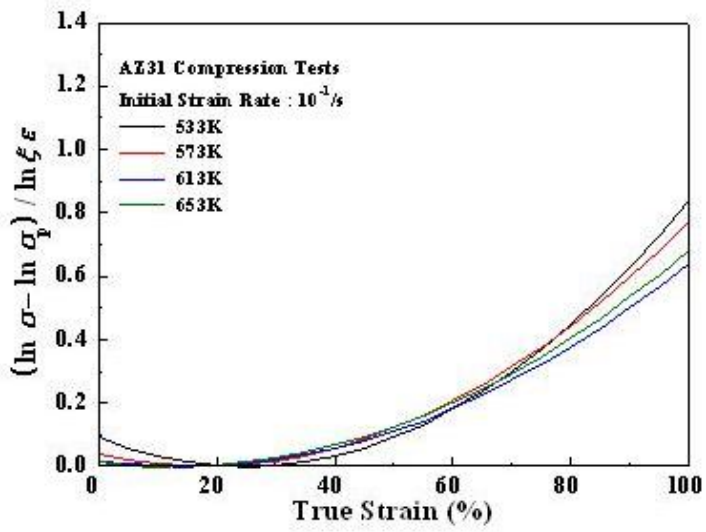


(a)

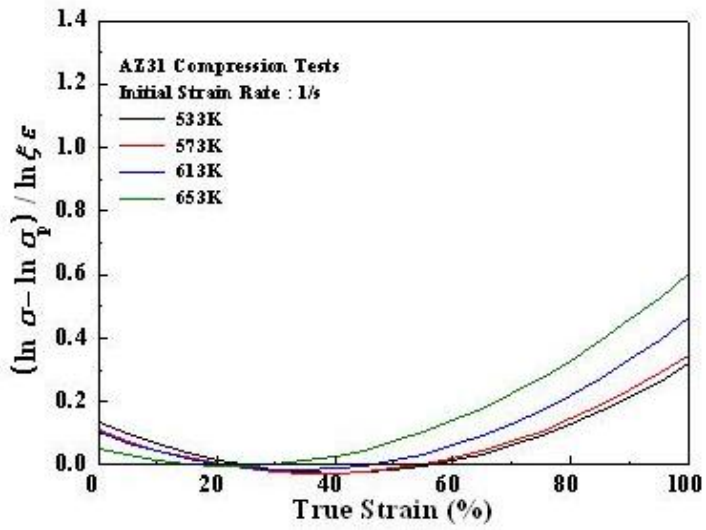


(b)

Figure 4.15 Schematic of the relationship of $(\ln \sigma - \ln \sigma_p) / \ln \xi \varepsilon$ and ε of AZ31 alloy at different strain rates; (a) $10^{-3}/s$, (b) $10^{-2}/s$, (c) $10^{-1}/s$ and (d) $1/s$.

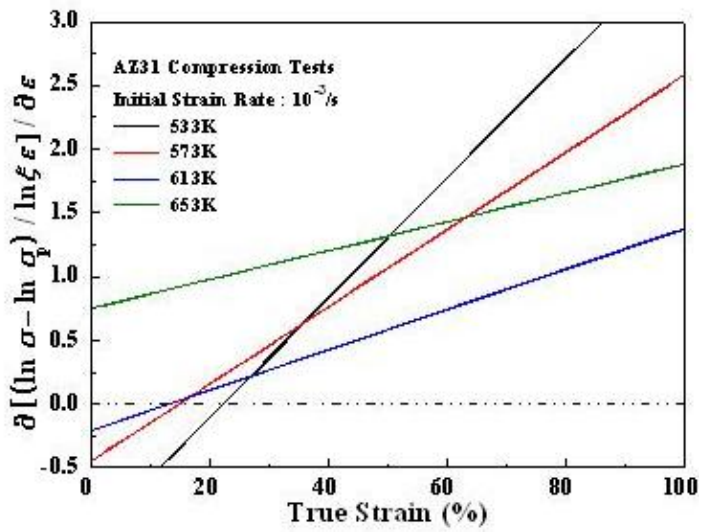


(c)

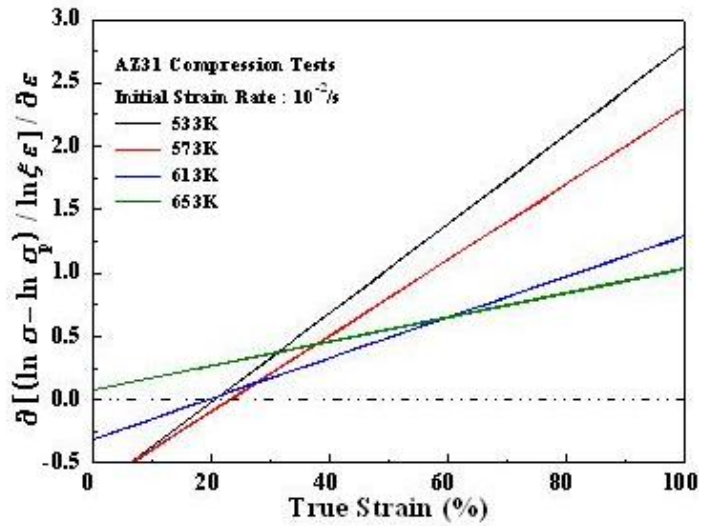


(d)

Figure 4.15 Continued.

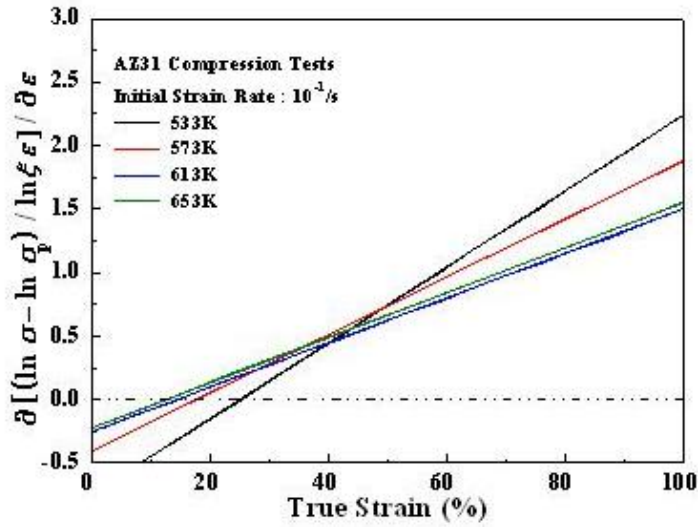


(a)

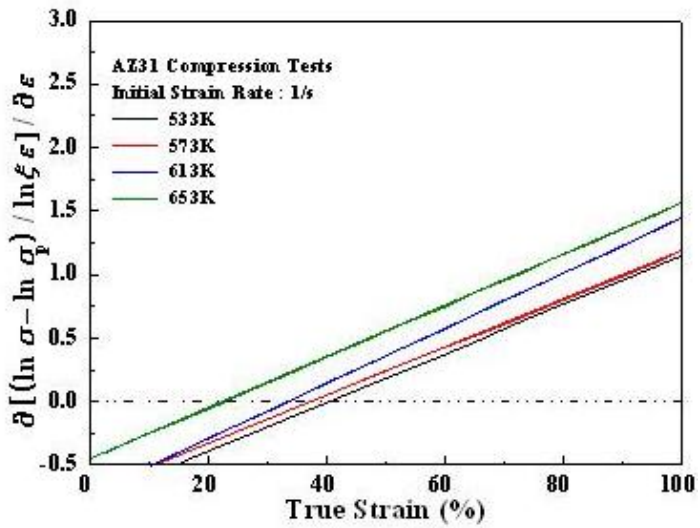


(b)

Figure 4.16 Schematic of the rate of change of $(\ln \sigma - \ln \sigma_p) / \ln \zeta \epsilon$ with ϵ of AZ31 alloy at different strain rates; (a) $10^{-3}/s$, (b) $10^{-2}/s$, (c) $10^{-1}/s$ and (d) $1/s$.

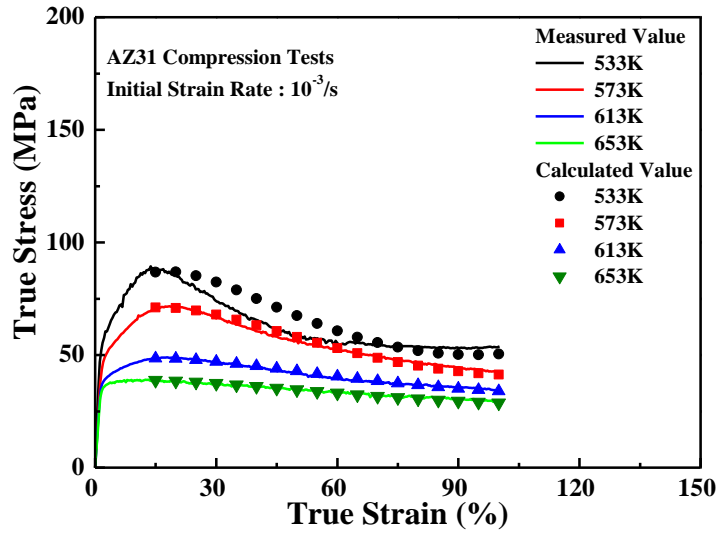


(c)

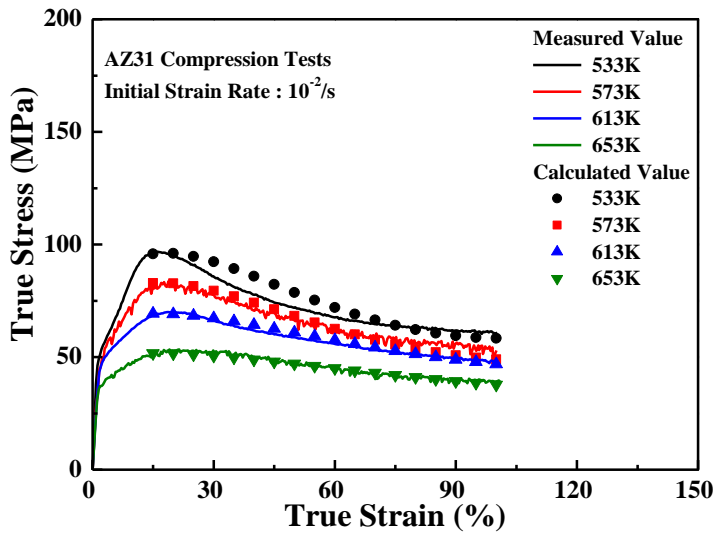


(d)

Figure 4.16 Continued.

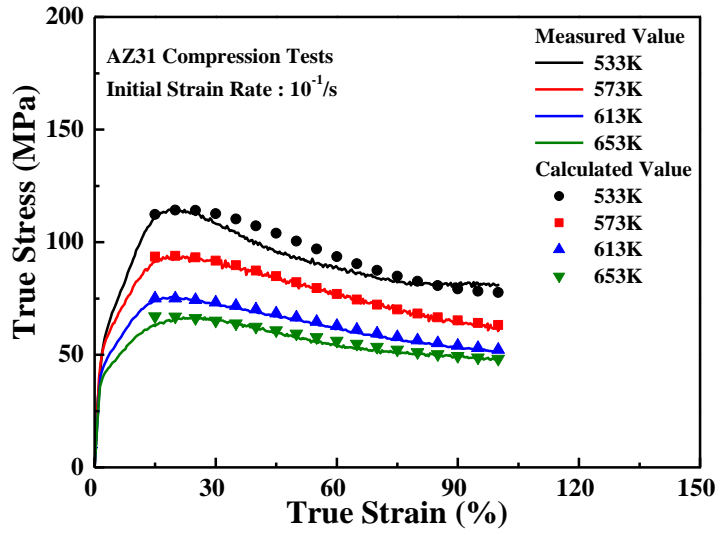


(a)

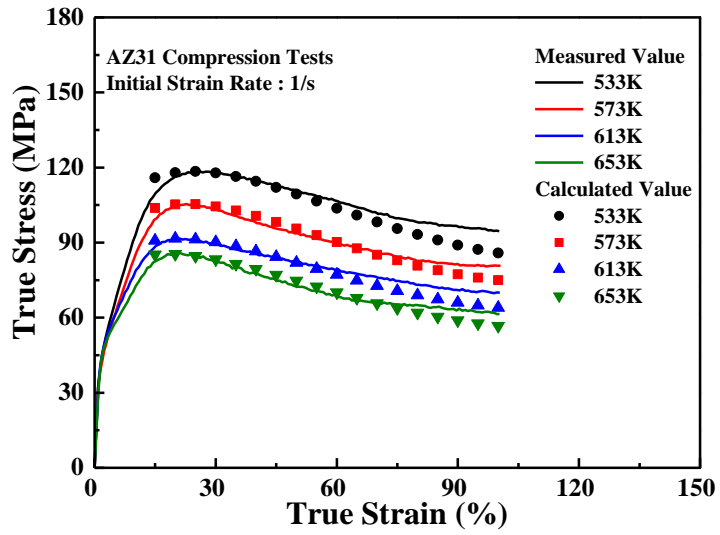


(b)

Figure 4.17 Comparison between model prediction results and experimental results of AZ31 alloy; (a) $10^{-3}/s$, (b) $10^{-2}/s$, (c) $10^{-1}/s$ and (d) $1/s$.



(c)



(d)

Figure 4.17 Continued.

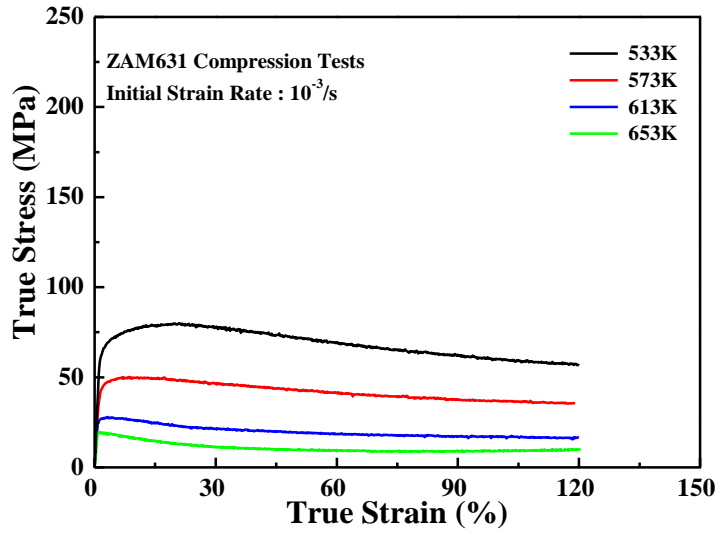
Table 4.7 Ψ and ξ values for AZ31 alloy under different deformation conditions.

Strain rate (/s)	Temperature (K)	Ψ	ξ
$10^{-3}/s$	533	2.355	0.711
	573	1.532	0.599
	613	0.880	0.555
	653	0.568	0.455
$10^{-2}/s$	533	1.758	0.655
	573	1.499	0.600
	613	0.799	0.500
	653	0.477	0.400
$10^{-1}/s$	533	1.497	0.652
	573	1.139	0.588
	613	0.875	0.545
	653	0.887	0.588
1/s	533	0.962	0.555
	573	1.075	0.588
	613	1.083	0.588
	653	1.007	0.544

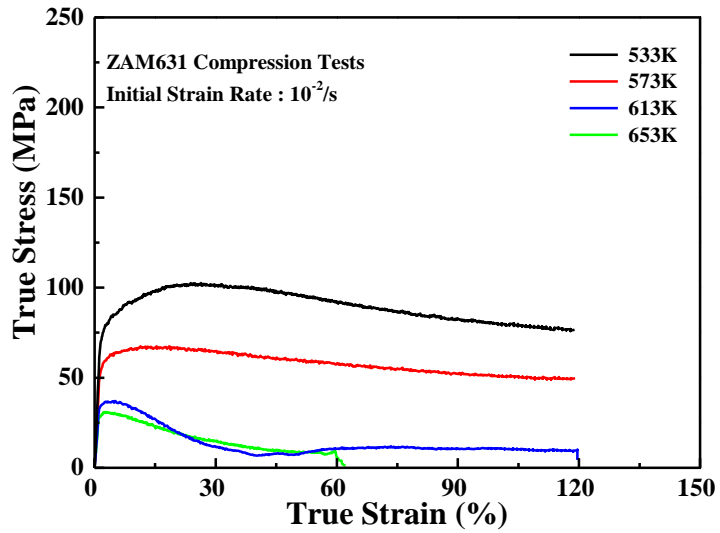
4.3 Hot Deformation behavior of ZAM631 alloy

4.3.1 Flow stress behavior

Figure 4.18 shows the stress-strain curves of ZAM631 alloy under various deformation conditions. The general characteristics of the flow stress curves were similar under all deformation conditions. The flow stress increased to a peak (initial strain hardening) and then decreased to a steady state. With decreasing strain rate or increasing temperature, the strain hardening effect becomes weaker. As a result, the peak stress varies according to deformation conditions, so does the peak strain. Under a constant strain rate, the peak stress and the peak strain increased with decreasing temperature. Under a constant temperature, the peak stress and the peak strain increased with increasing strain rate. For ZAM631 alloy as in AZ31 alloy, DRX is also the typical characteristic of flow stress curves [10]. This phenomenon usually occurs for metals with low to medium stacking fault energy (SFE) [77]. DRX, which can reduce the dislocation density and release the accumulated energy to facilitate straining [74], reduces considerably the flow stress and refines the grain size and provides improvement of ductility [71].

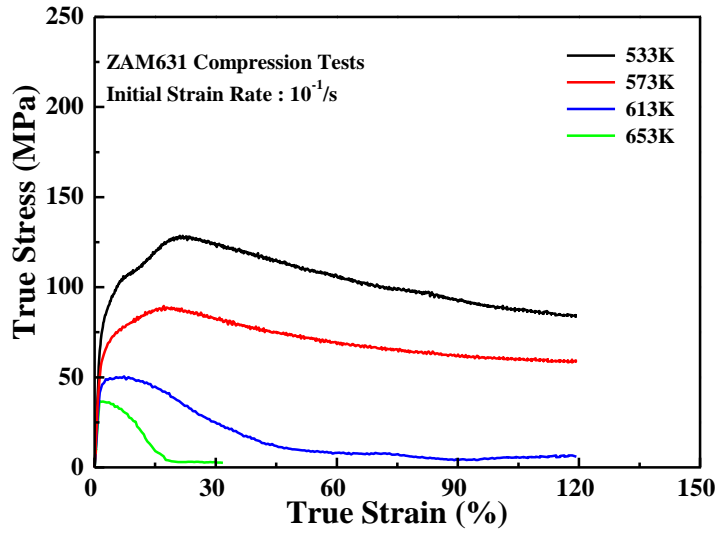


(a)

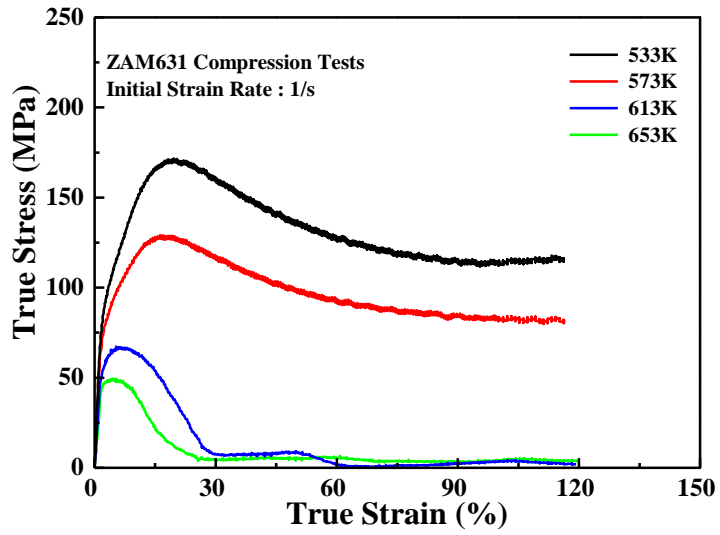


(b)

Figure 4.18 True stress-true strain curves of ZAM631 alloy at different strain rates; (a) $10^{-3}/s$, (b) $10^{-2}/s$, (c) $10^{-1}/s$ and (d) $1/s$.



(c)



(d)

Figure 4.18 Continued.

4.3.2 Microstructures

Figures 4.19~4.21 show the microstructure evolutions of compressed ZAM631 alloy corresponding to the various deformation conditions (temperatures, strain rate and strain). The observed planes of specimens were parallel to the compression direction. The grains were broken and elongated. The grain boundaries are being serrated and this serration as well as elongation of grains increased with increasing strain. In the initial stage of DRX, the formation of a limited number of new small grains was observed. More new small grains were formed with deformation to higher strain. With increasing strain beyond the peak, most of the pre-existing boundaries were decorated by these new DRX grains.

The grain size and the volume fraction of DRX are dependent sensitively on deformation temperature and /or strain rate [73]. Tables 4.8 and 4.9 show the grain size and the volume fraction under the various deformation conditions. These observations reveal that the microstructural behaviors could be related to the Zener-Hollomon parameter Z as in AZ31 alloy. Figure 4.22 shows average DRX grain size under various deformation conditions. Average DRX grain size increased with increasing deformation temperature. Figure 4.23 shows the relationship between average DRX grain size and $\ln Z$. Average DRX grain size exhibit linear dependency on $\ln Z$ as following:

$$D_{\text{drx}} = 228,927 Z^{-0.224} \quad (4.17)$$

Table 4.10 shows the $\ln Z$ values under various deformation conditions. The volume fraction and the grain size of DRX decrease with increasing Z value, that is to say decreasing deformation temperature or increasing strain rate. A high Z value leads to a lower DRX kinetics because of lower diffusivity at lower temperatures and/or insufficient time at higher strain rates. As there is not enough time for diffusion to take place at high strain rates, therefore the grain growth is not so pronounced. As a result, the growth of new DRX grains was limited, thereby reducing the size of DRX grains [72].

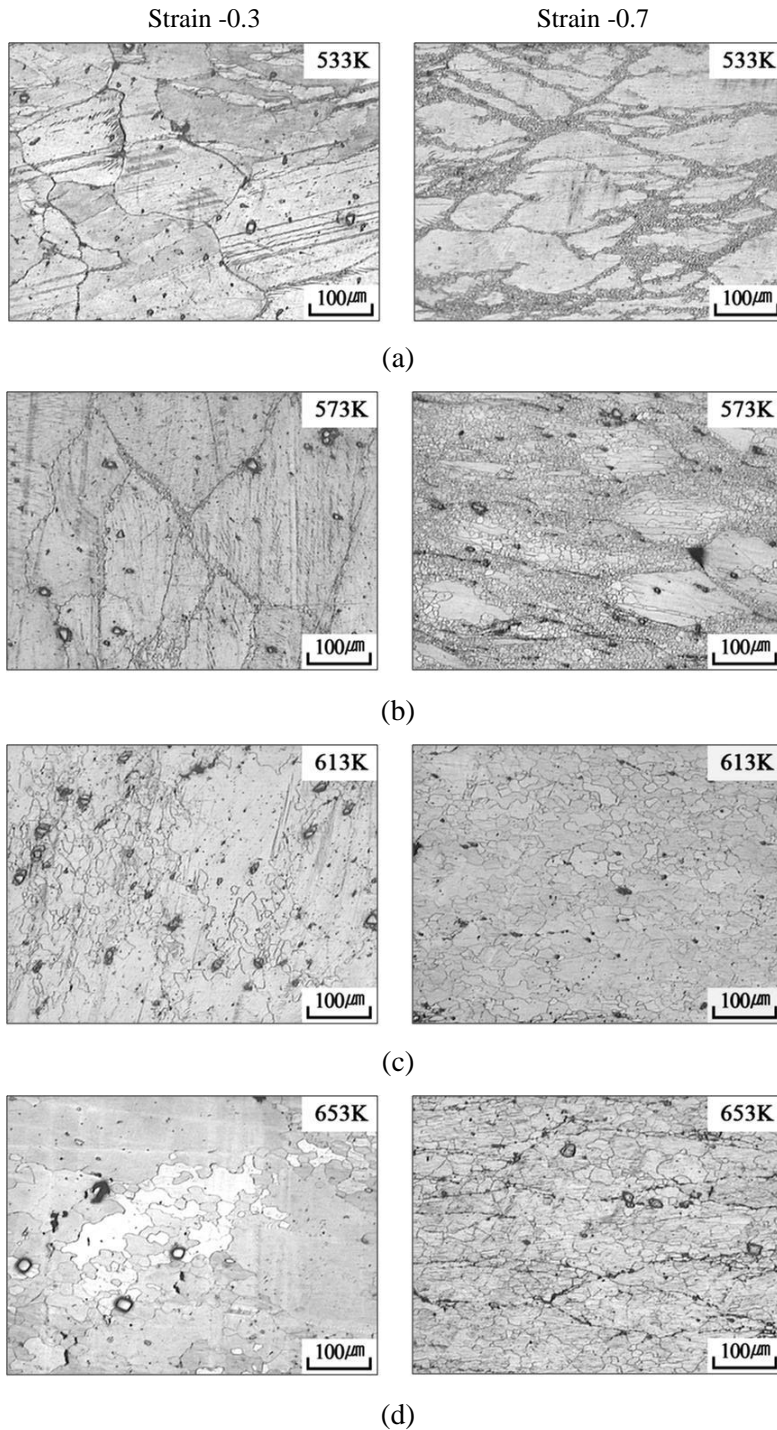


Figure 4.19 Microstructures of the ZAM631 alloy compressed at a strain rate $10^{-3}/s$ at a strain -0.3 and -0.7; (a) 533K, (b) 573K, (c) 613K and (d) 653K.

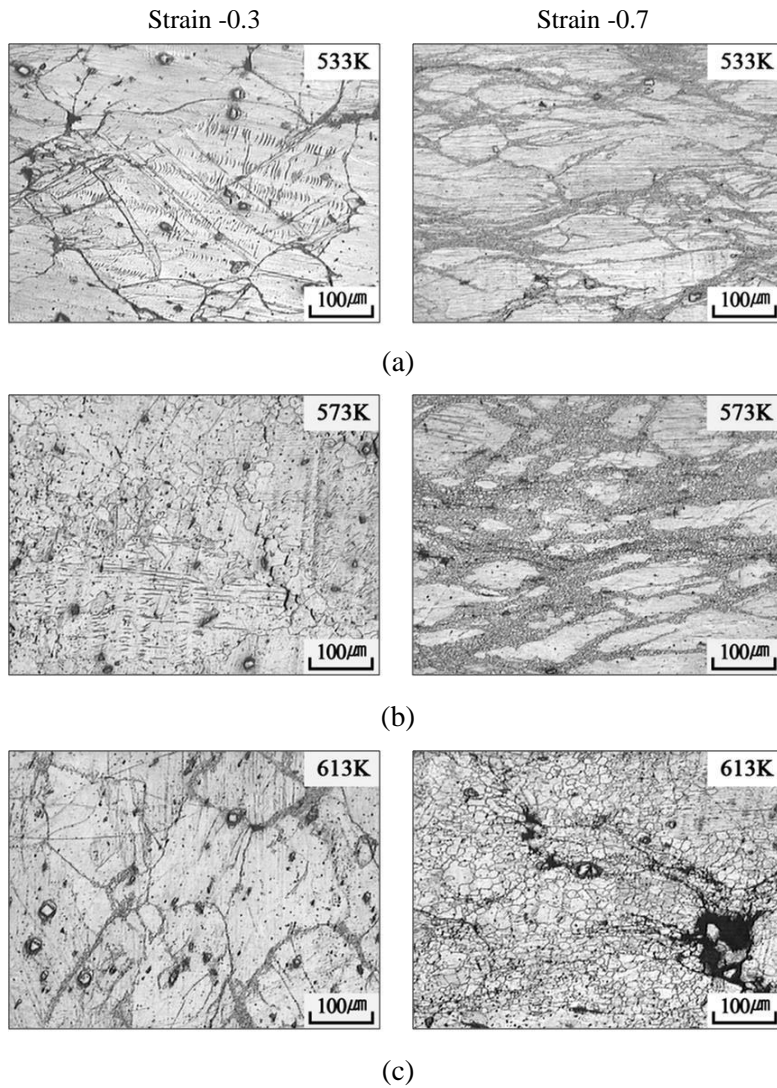


Figure 4.20 Microstructures of the ZAM631 alloy compressed at a strain rate $10^{-2}/s$ at a strain -0.3 and -0.7; (a) 533K, (b) 573K, and (c) 613K.

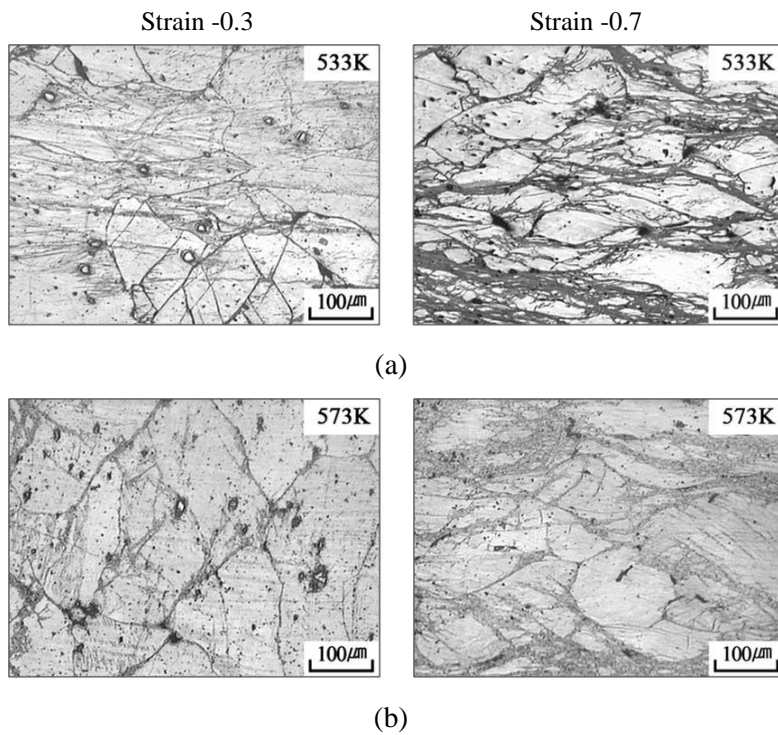


Figure 4.21 Microstructures of the ZAM631 alloy compressed at a strain rate $10^{-1}/s$ at a strain -0.3 and -0.7; (a) 533K and (b) 573K.

Table 4.8 Average DRX grain size (D_{drx}) of ZAMX631 alloy at a strain -0.7.

Strain rate (/s)	Temperature (K)	D_{drx} (μm)
$10^{-3}/\text{s}$	533	2.805
	573	8.541
	613	17.396
	653	25.079
$10^{-2}/\text{s}$	533	1.556
	573	5.773
	613	13.735
$10^{-1}/\text{s}$	533	1.099
	573	3.121

Table 4.9 DRX volume fraction (X_{DRX}) of ZAM631 alloy at a strain -0.7.

Strain rate (/s)	Temperature (K)	X_{DRX} (%)
$10^{-3}/\text{s}$	533	53.026
	573	58.226
	613	100
	653	100
$10^{-2}/\text{s}$	533	49.642
	573	55.872
	613	80.101
$10^{-1}/\text{s}$	533	48.471
	573	50.284

Table 4.10 $\ln Z$ values for ZAM631 alloy under different deformation conditions.

Strain rate (/s)	Temperature (K)	$\ln Z$ (/s)
$10^{-3}/s$	533	49.941
	573	45.972
	613	42.522
	653	39.494
$10^{-2}/s$	533	52.243
	573	48.275
	613	44.824
	653	41.796
$10^{-1}/s$	533	54.546
	573	50.577
	613	47.127
	653	44.099
1/s	533	56.848
	573	52.880
	613	49.429
	653	46.402

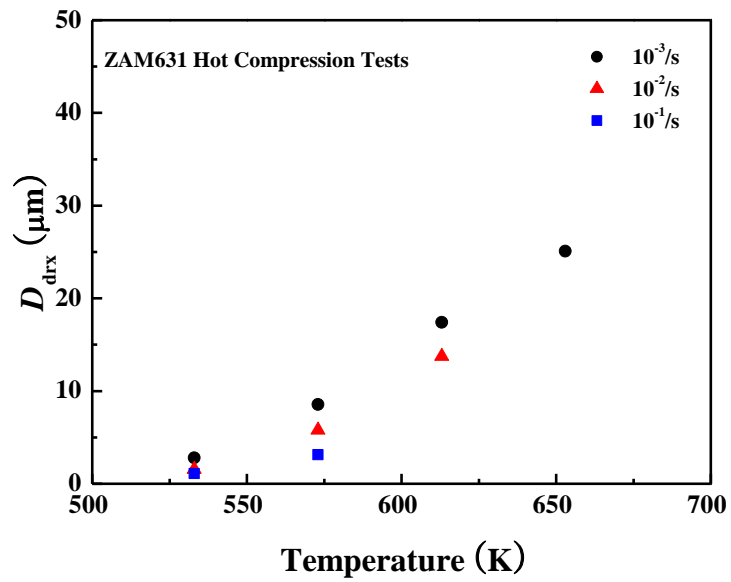


Figure 4.22 Average DRX grain size of ZAM631 alloy compressed at various strain rates at a strain -0.7.

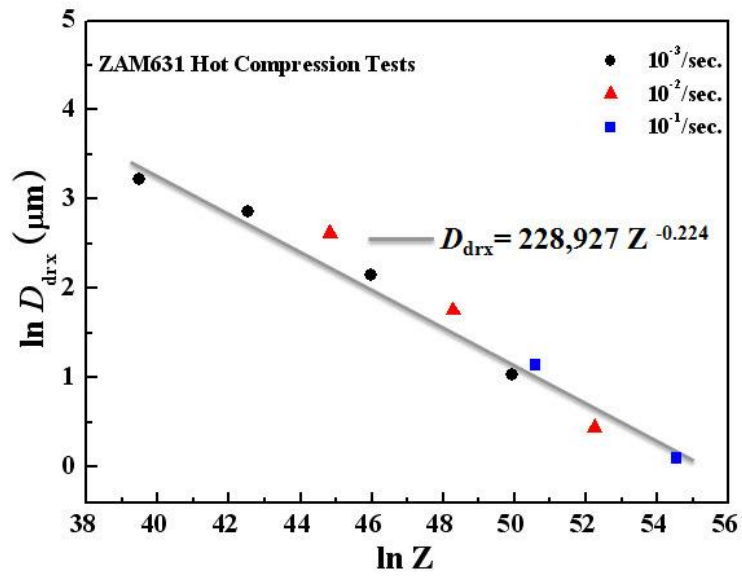


Figure 4.23 Relation between average DRX grain size and Zener-Hollomon parameter for ZAM631 alloy.

4.3.3 Modeling of flow stress

Computer simulation of metal forming processes enables, hitherto not possible, obtaining a process model that is closer to the real conditions [75]. Two methods can be used to build flow stress equation. One is based on deformation mechanism from the microstructure's point of view such as dislocation density and grain size. The other is based on macroscopic mechanical behavior i.e., flow stress curve, thus the flow stress equation results from regression analysis of tests data [10].

The mechanical properties of the workpiece under hot working are generally expressed by a constitutive equation, which connects flow stress to the variables such as strain, strain rate, temperature and microstructures. In order to understand and control the hot working process, setting up a constitutive equation for DRX is needed [76].

4.3.3.1 Determination of peak stress

In hot deformation of magnesium alloy ZAM631, the atomic diffusibility and the driving force of dislocation migration are dependent on the temperature; the dislocation density and the cumulation of grain boundary energy are dependent on the strain rate. Therefore, the peak stress can be considered depending only on the temperature and strain rate, and taken as the function of the Zener-Hollomon parameter Z [10] as in AZ31 alloy.

The approximate value of n is 8.038 according to Figure 4.24 (a) and that of β is 0.119 according to Figure 4.24 (b). So, the suitable value of α is 0.015. The average value of slope of the $\ln(\sinh(\alpha\sigma_p))$ versus $1/T$ is approximately 5.181×10^3 according to Figure 4.24 (c). The reciprocal value of inclination of the $\ln(\sinh(\alpha\sigma_p))$ versus $\ln \dot{\epsilon}$ is approximately 5.849 according to Figure 4.24 (d). So, the value of Q equals 251.916 kJ/mol. According to Eq. (4.3), the exact values of A and n are obtained from the $\ln Z$ - $\ln(\sinh(\alpha\sigma_p))$ plot. According to Figure 4.24 (e), the relationship of σ_p and Z

is expressed as follows:

$$Z = \ln A + n (\sinh(\alpha\sigma_p)) \quad (4.7)$$

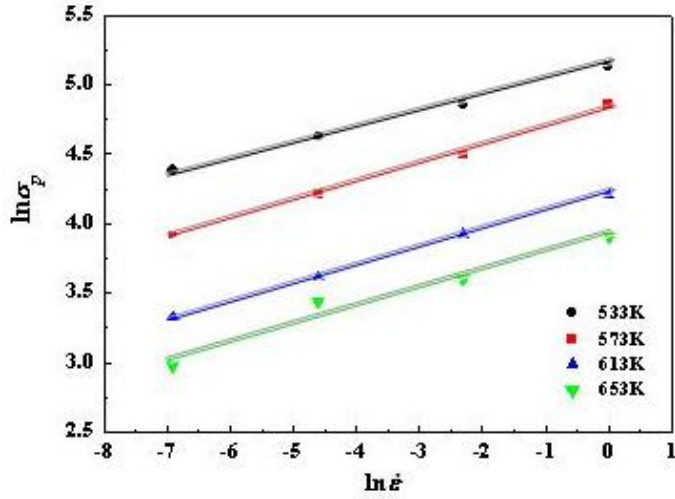
The σ_p is given by

$$\sigma_p = \frac{1}{\alpha} \cdot \left(\left(\frac{Z}{A} \right)^{\frac{1}{n}} + \left(\left(\frac{Z}{A} \right)^{\frac{2}{n}} + 1 \right) \right) \quad (4.8)$$

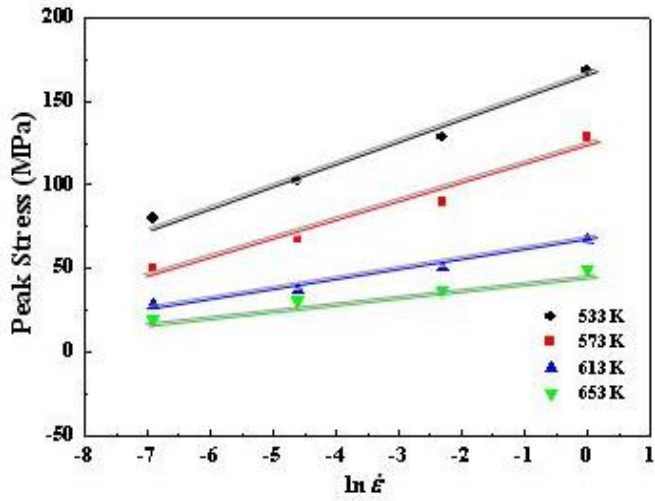
Where α is 0.015, n is 5.709, A is 3.761×10^{20} .

4.3.3.2 Determination of flow stress

According to the 4.1.3.2, the flow stress for reflecting DRX process under hot working was determined with the aid of the relations in Figures 4.25 and 4.26. This flow stress equation contains only two parameters which are ζ and Ψ . For multiple experimental values, the optimum values of two parameters obtained by the least-squares method are shown in Table 4.11. Figure 4.27 shows the comparison between model prediction results and experimental results of ZAM631 alloy. The predicted results show good agreement with the experimental data. This flow stress model has been presented for the flow stress under various deformation conditions (strain, temperature and strain rate) and can be applied in the range of corresponding to the temperature between 533K and 653K, strain rate between $10^{-3}/s$ and $1/s$ and strain less than 1.

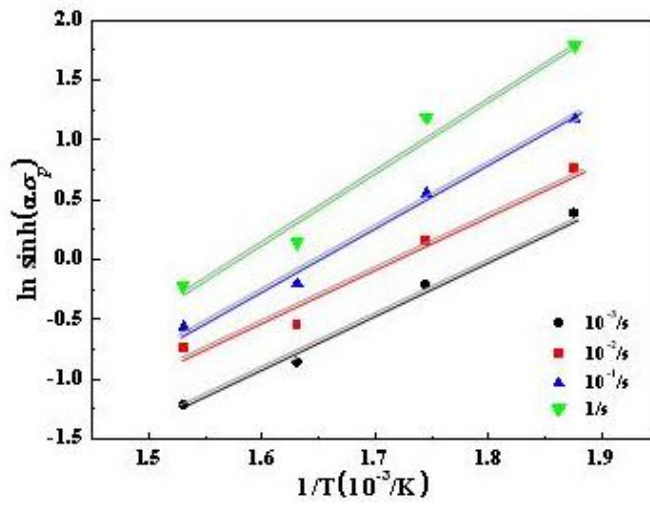


(a)

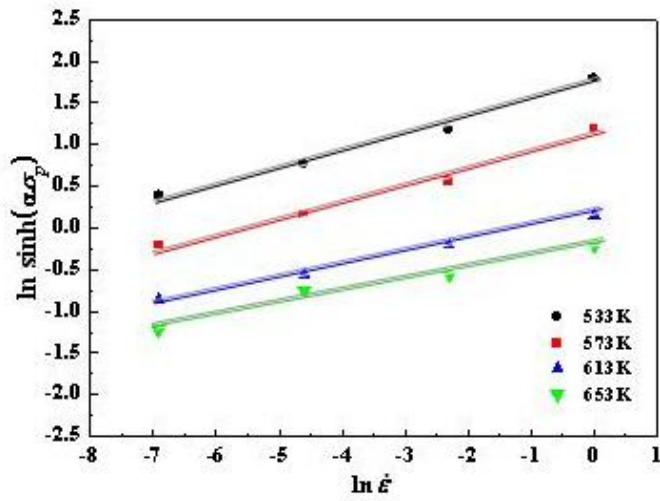


(b)

Figure 4.24 Schematic of the dependence of the peak stress of ZAM631 alloy on temperature and strain rate: (a) schematic of $\ln \sigma_p$ versus $\ln \dot{\epsilon}$, (b) schematic of σ_p versus $\ln \dot{\epsilon}$, (c) schematic of $\ln(\sinh(\alpha \sigma_p))$ versus $1/T$, (d) schematic of $\ln(\sinh(\alpha \sigma_p))$ versus $\ln \dot{\epsilon}$, (e) schematic of $\ln(\sinh(\alpha \sigma_p))$ versus $\ln Z$ and (f) schematic of $\ln \epsilon_p$ versus $\ln Z$.

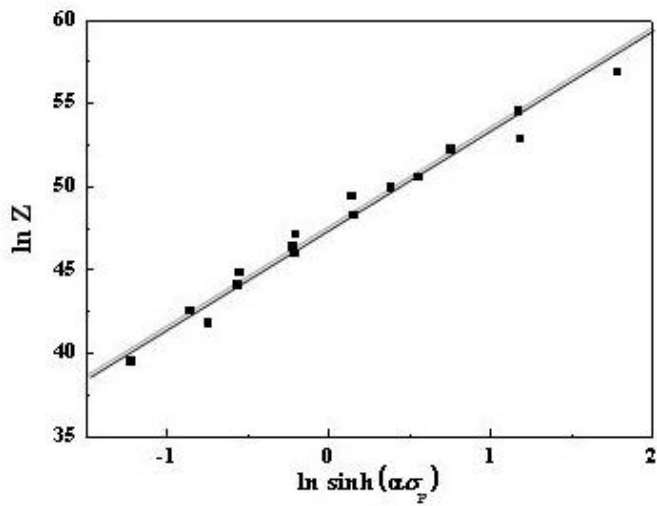


(c)



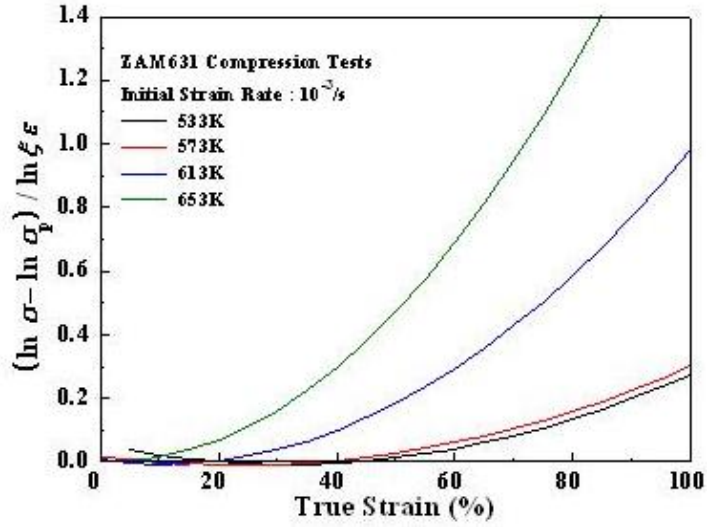
(d)

Figure 4.24 Continued.

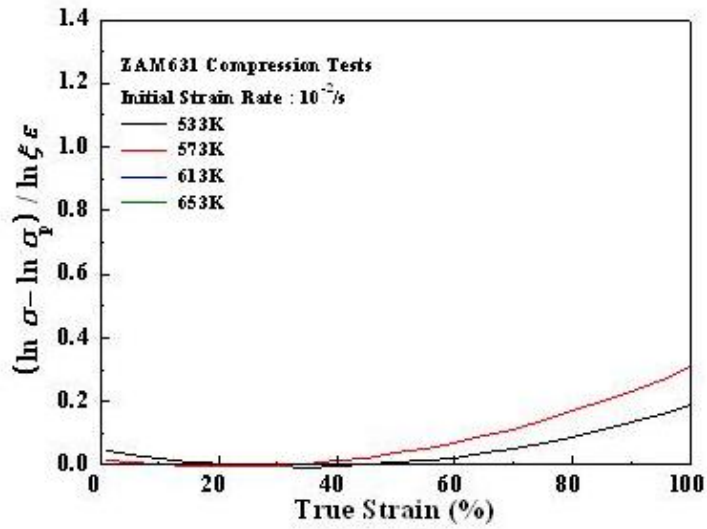


(e)

Figure 4.24 Continued.

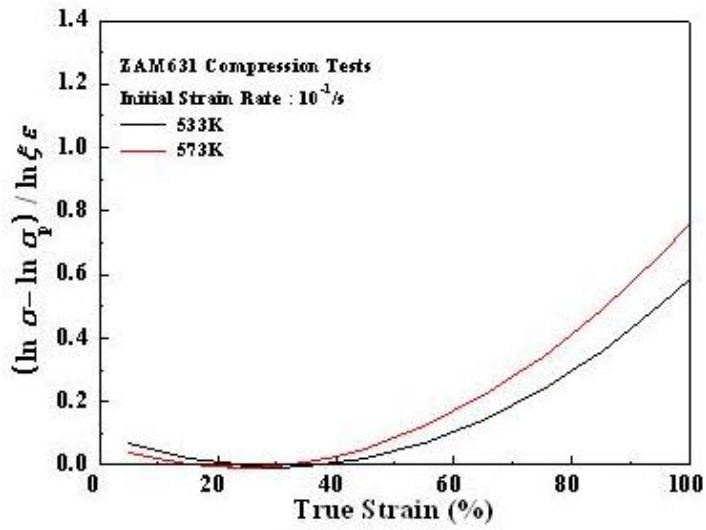


(a)

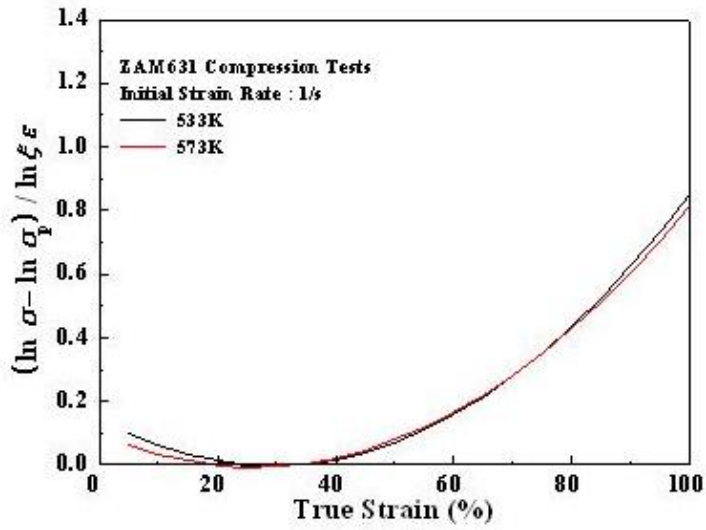


(b)

Figure 4.25 Schematic of the relationship of $(\ln \sigma - \ln \sigma_p) / \ln \xi \epsilon$ and ϵ of ZAM631 alloy at different strain rates; (a) $10^{-3}/s$, (b) $10^{-2}/s$, (c) $10^{-1}/s$ and (d) $1/s$.

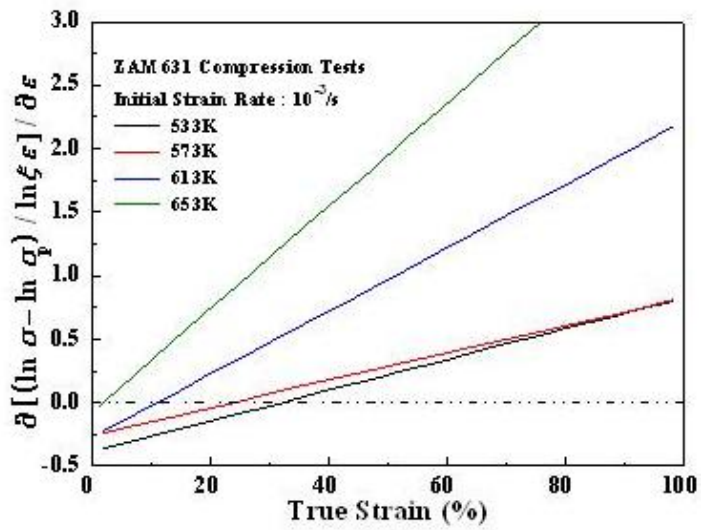


(c)

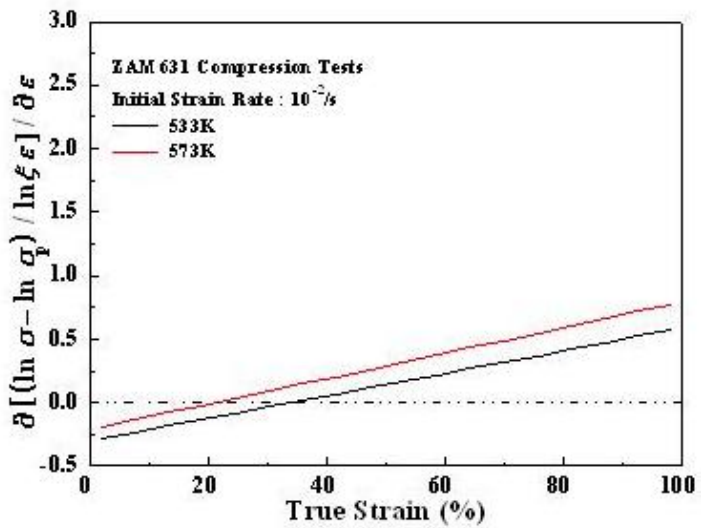


(d)

Figure 4.25 Continued.

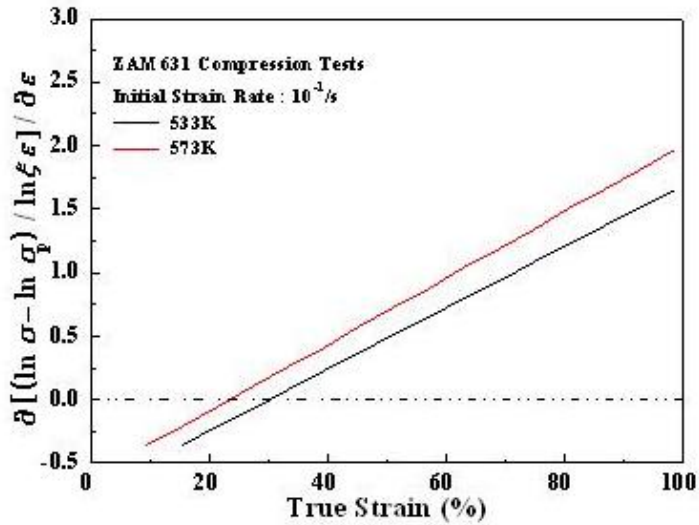


(a)

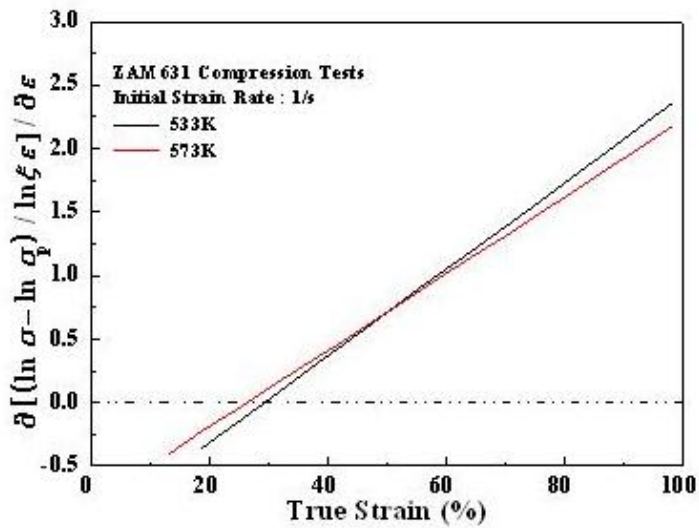


(b)

Figure 4.26 Schematic of the rate of change of $(\ln \sigma - \ln \sigma_p) / \ln \zeta \varepsilon$ with ε of ZAM631 alloy at different strain rates; (a) $10^{-3}/s$, (b) $10^{-2}/s$, (c) $10^{-1}/s$ and (d) $1/s$.

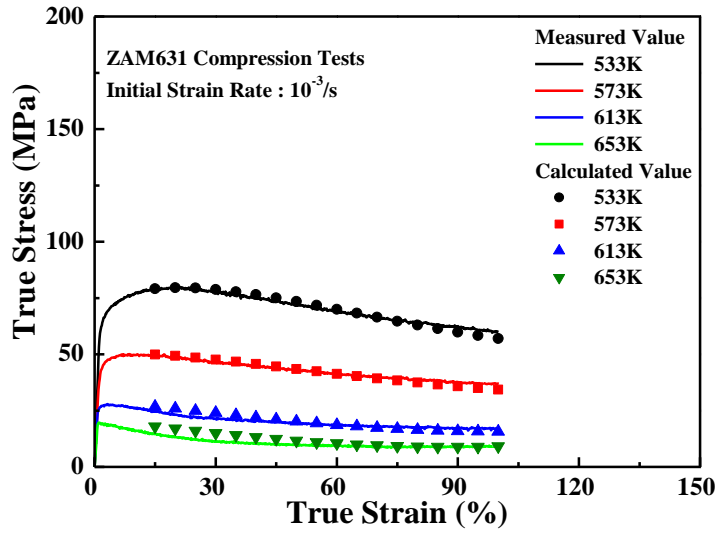


(c)

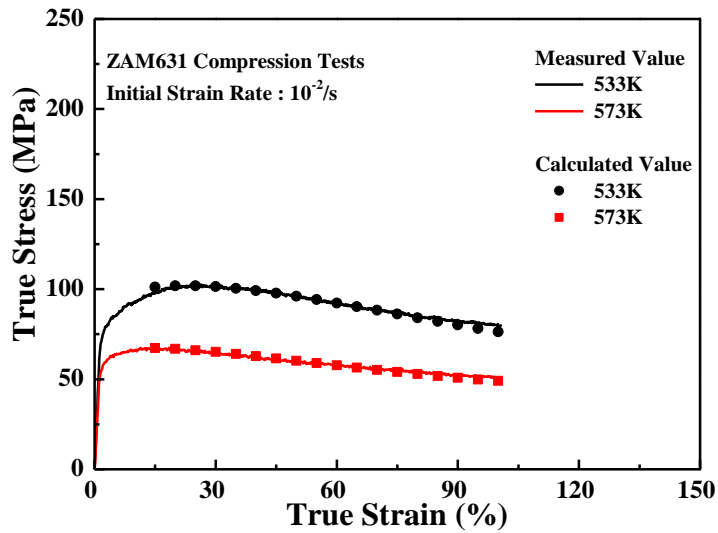


(d)

Figure 4.26 Continued.

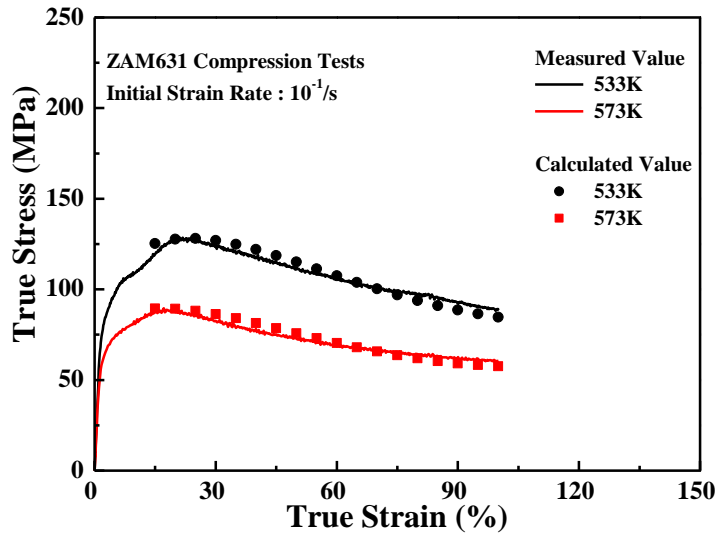


(a)

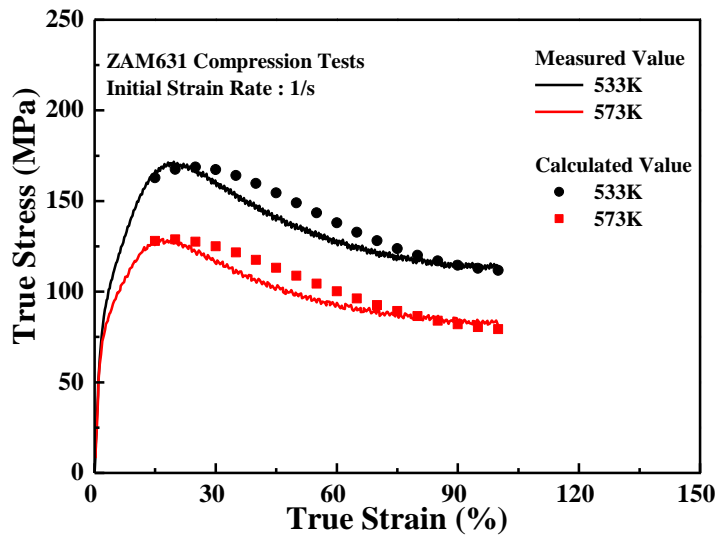


(b)

Figure 4.27 Comparison between model prediction results and experimental results of ZAM631 alloy; (a) $10^{-3}/s$, (b) $10^{-2}/s$, (c) $10^{-1}/s$ and (d) $1/s$.



(c)



(d)

Figure 4.27 Continued.

Table 4.11 Ψ and ξ values for ZAM631 alloy under different deformation conditions.

Strain rate (/s)	Temperature (K)	Ψ	ξ
$10^{-3}/s$	533	0.605	0.411
	573	0.540	0.433
	613	1.245	0.611
	653	2.021	0.677
$10^{-2}/s$	533	0.442	0.333
	573	0.501	0.445
$10^{-1}/s$	533	1.207	0.555
	573	1.309	0.611
1/s	533	1.707	0.655
	573	1.509	0.611

4.4 Finite element analysis of extrusion process

4.4.1 FE analysis during AZ31 alloy plate (3t) extrusion

Figure 4.28 shows the result of simulation at three different stages. The evolution of three macroscopic variables, temperature, strain rate and strain were compared at each stage. Point tracking function was used to trace the location of point P1 at each stage.

Figure 4.28 (a) shows the evolution of temperature of P1 traced during extrusion. The initial temperature of P1 was 533K. As the cross-section area of the billet were being reduced at the first stage, the temperature of P1 increased gradually and the maximum temperature reached 578K in the third stage which is the last part of the billet near the exit of the die. The varying temperature distribution of the billet during extrusion is caused by deformation, the friction between the billet and tooling, heat loss to the surroundings and the heat conduction within the billet. The temperature evolutions of P1 at 573K, 613K and 653K showed the similar trend to that at 533K. The maximum temperatures reached 609K, 643K and 684K during extrusion at 573K, 613K and 653K, respectively.

Figure 4.28 (b) shows the evolution of effective strain rate of P1 during extrusion. As P1 flowed into the deformation zone, the effective strain rate increased gradually. In the severe deformation zone in front of the die exit, the effective strain rate reached 1.9/s and remained higher than 1.9/s in the billet closer to the exit of the die. The effective strain rate evolutions of P1 at 573K, 613K and 653K showed the similar trend to that at 533K. The effective strain rate in all simulations remained at the range of 1.9~2.1/s in the third stage.

Figure 4.28 (c) shows the evolution of effective strain at P1 traced during extrusion. With reducing cross-section area of the billet, the strain of P1 increased gradually. And then the effective strain reached 4.92 in the third

stage. The effective strain evolutions of P1 at 573K, 613K and 653K showed the similar trend to that at 533K. The effective strain in all simulations remained at the range of 4.5~5.4 in the third stage.

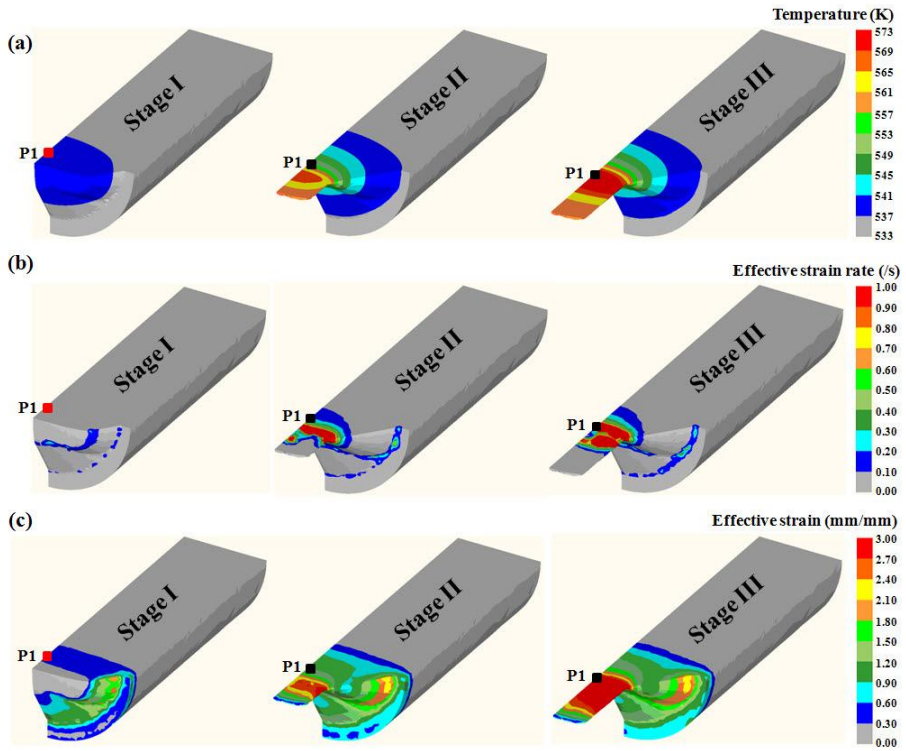


Figure 4.28 Macroscopic extrusion deformation behavior of the AZ31 alloy at P1 traced during extrusion at 533K; (a) evolution of temperature, (b) evolution of effective strain rate and (c) evolution of effective strain.

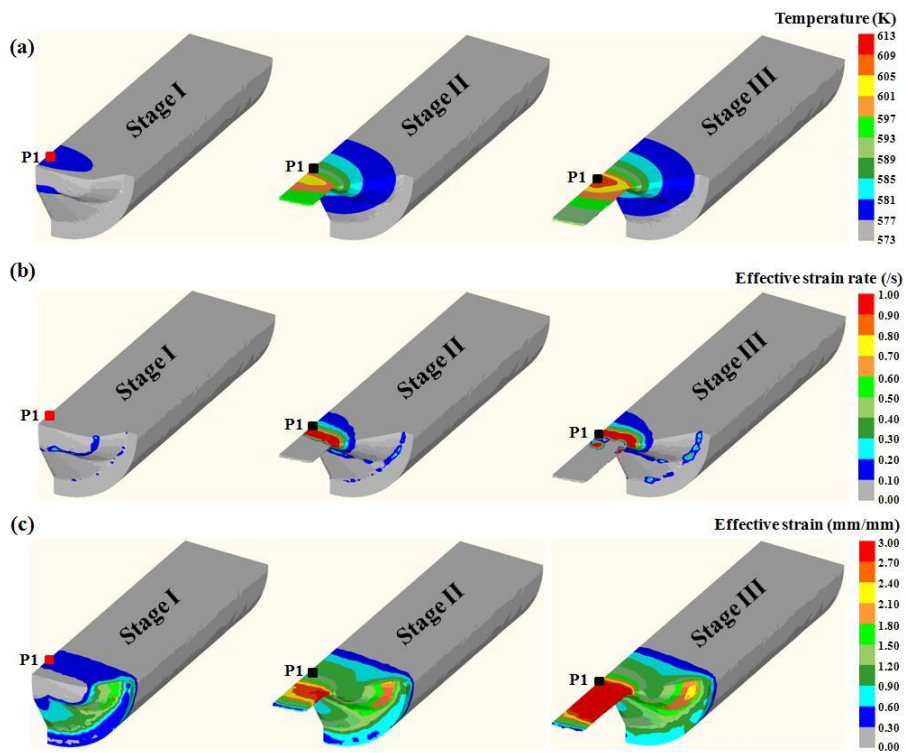


Figure 4.29 Macroscopic extrusion deformation behavior of the AZ31 alloy at P1 traced during extrusion at 573K; (a) evolution of temperature, (b) evolution of effective strain rate and (c) evolution of effective strain.

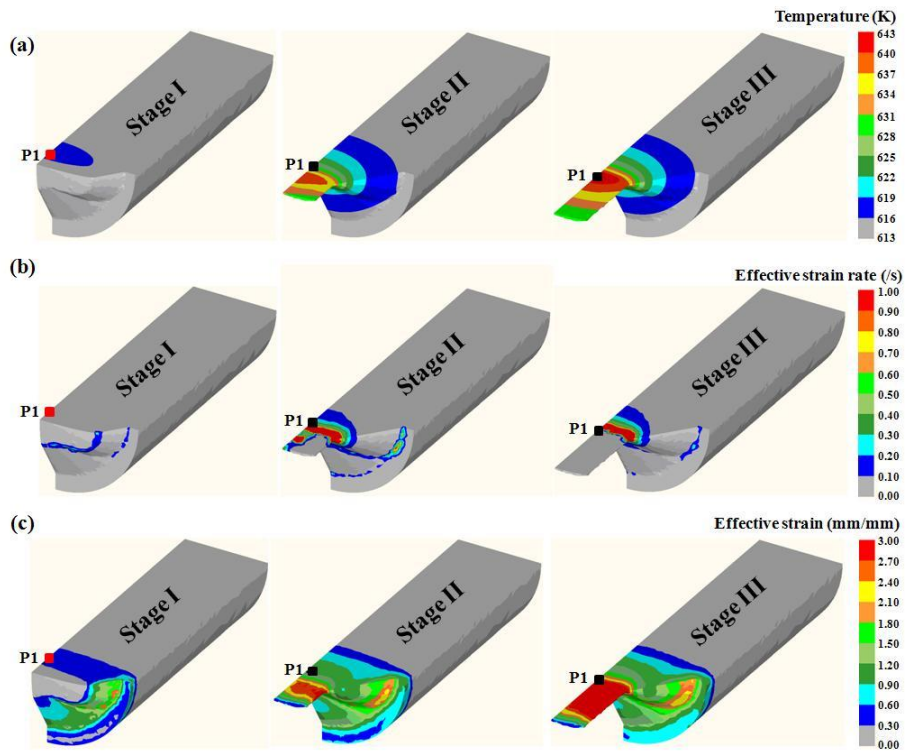


Figure 4.30 Macroscopic extrusion deformation behavior of the AZ31 alloy at P1 traced during extrusion at 613K; (a) evolution of temperature, (b) evolution of effective strain rate and (c) evolution of effective strain.

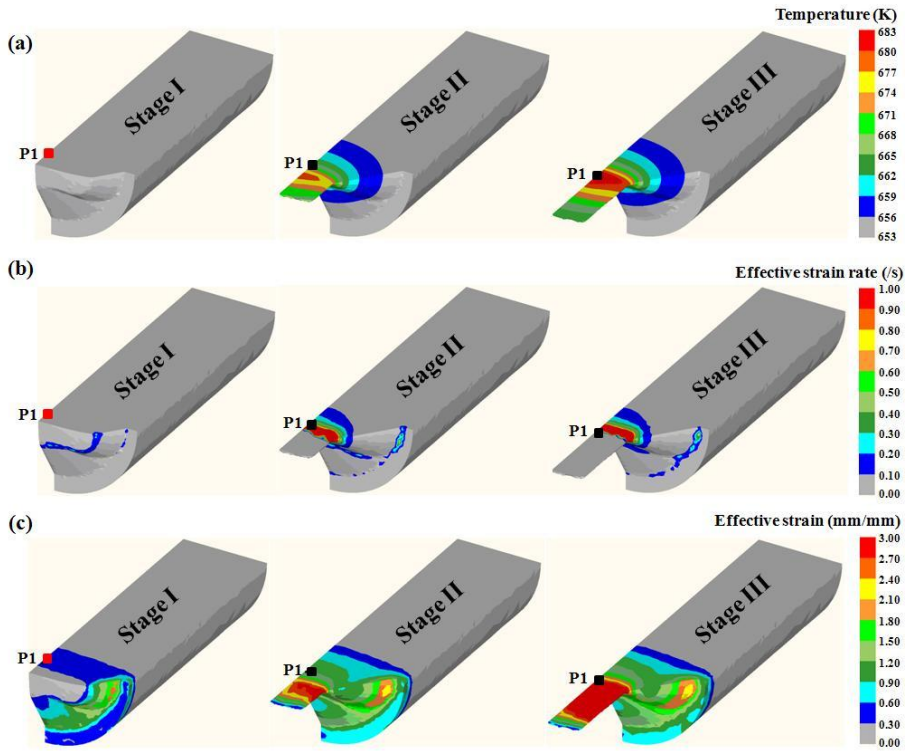


Figure 4.31 Macroscopic extrusion deformation behavior of the AZ31 alloy at P1 traced during extrusion at 653K; (a) evolution of temperature, (b) evolution of effective strain rate and (c) evolution of effective strain.

4.4.2 FE analysis during ZAM631 alloy rod (16Φ) extrusion

Figures 4.32~4.35 show the result of simulation at three different stages. The evolution of three macroscopic variables, temperature, strain rate and strain were compared at each stage. Point tracking function was used to trace the location of point P1 at each stage.

Figure 4.32 (a) shows the evolution of temperature of P1 traced during extrusion. The initial temperature of P1 was 533K. As the cross-section area of the billet were being reduced at the first stage, the temperature of P1 increased gradually and the maximum temperature reached 549K in the third stage which is the last part of the billet near the exit of the die. The varying temperature distribution of the billet during extrusion is caused by deformation, the friction between the billet and tooling, heat loss to the surroundings and the heat conduction within the billet. The temperature evolutions of P1 at 573K, 613K and 653K showed the similar trend to that at 533K. The maximum temperatures reached 584K, 621K and 659K during extrusion at 573K, 613K and 653K, respectively. Figure 4.32 (b) shows the evolution of effective strain rate of P1 during extrusion. As P1 flowed into the deformation zone, the effective strain rate increased gradually. In front of the die exit, the effective strain rate reached 0.23/s in the billet closer to the exit of the die. The effective strain rate evolutions of P1 at 573K, 613K and 653K showed the similar trend to that at 533K. The effective strain rate in all simulations remained at the range of 0.23~0.24/s in the third stage.

Figure 4.32 (c) shows the evolution of effective strain. With reducing cross-section area of the billet, the strain of P1 increased gradually. And then the effective strain reached 1.74 in the third stage. The effective strain evolutions of P1 at 573K, 613K and 653K showed the similar trend to that at 533K. The effective strain in all simulations remained at the range of 1.58~1.87 in the third stage.

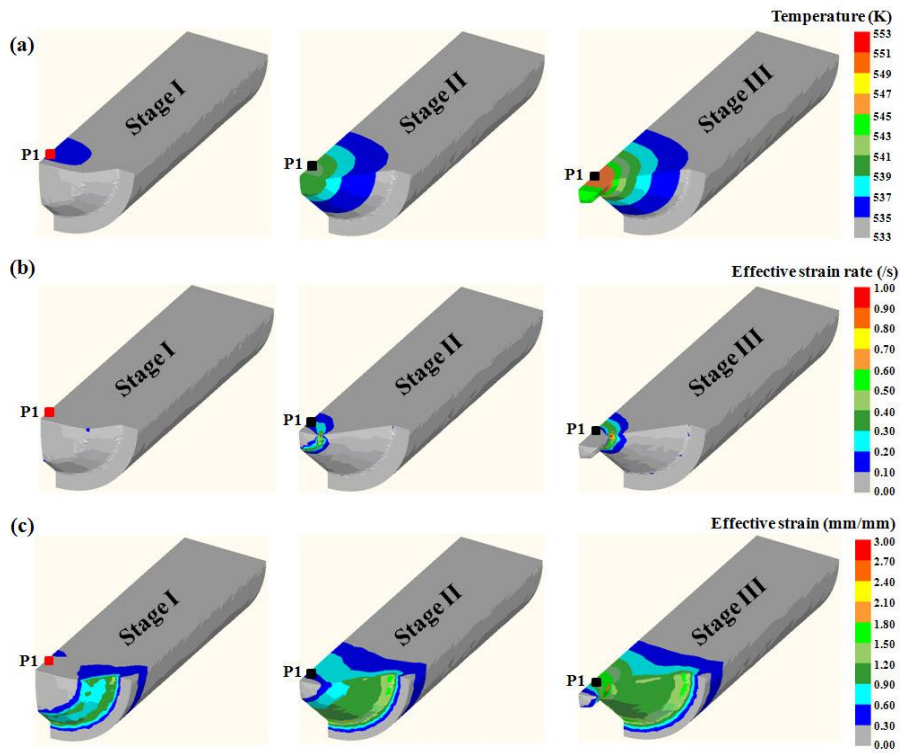


Figure 4.32 Macroscopic extrusion deformation behavior of the ZAM631 alloy at P1 traced during extrusion at 533K; (a) evolution of temperature, (b) evolution of effective strain rate and (c) evolution of effective strain.

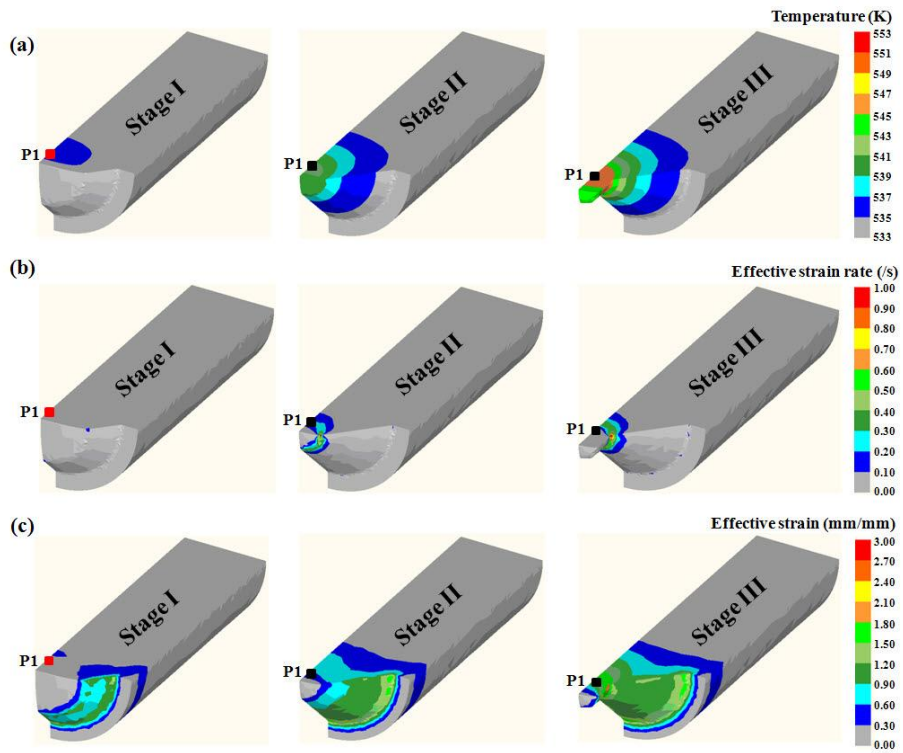


Figure 4.33 Macroscopic extrusion deformation behavior of the ZAM631 alloy at P1 traced during extrusion at 573K; (a) evolution of temperature, (b) evolution of effective strain rate and (c) evolution of effective strain.

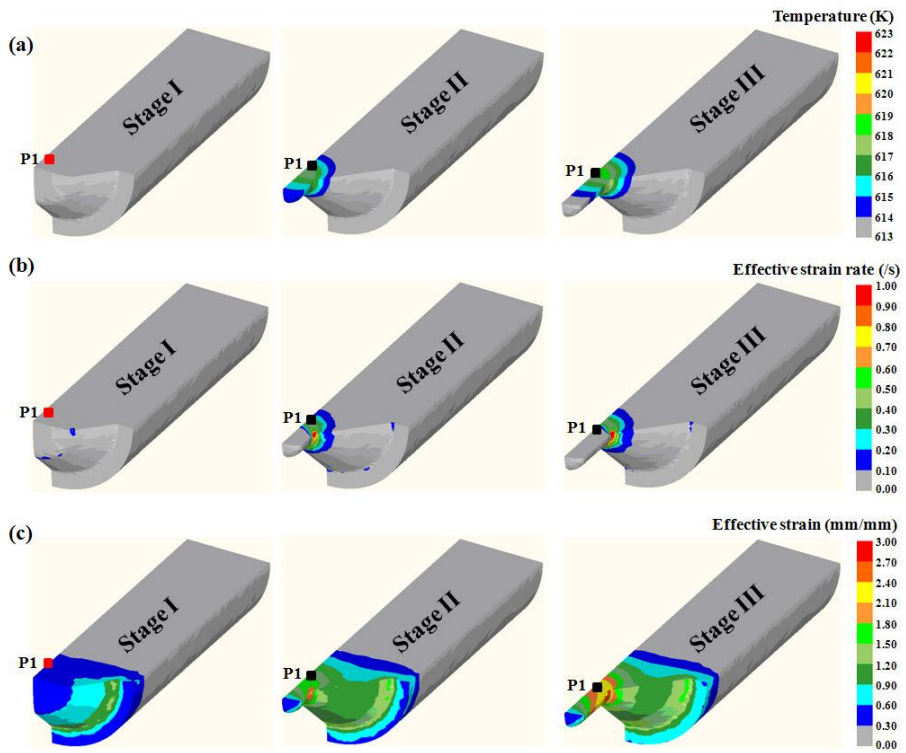


Figure 4.34 Macroscopic extrusion deformation behavior of the ZAM631 alloy at P1 traced during extrusion at 613K; (a) evolution of temperature, (b) evolution of effective strain rate and (c) evolution of effective strain.

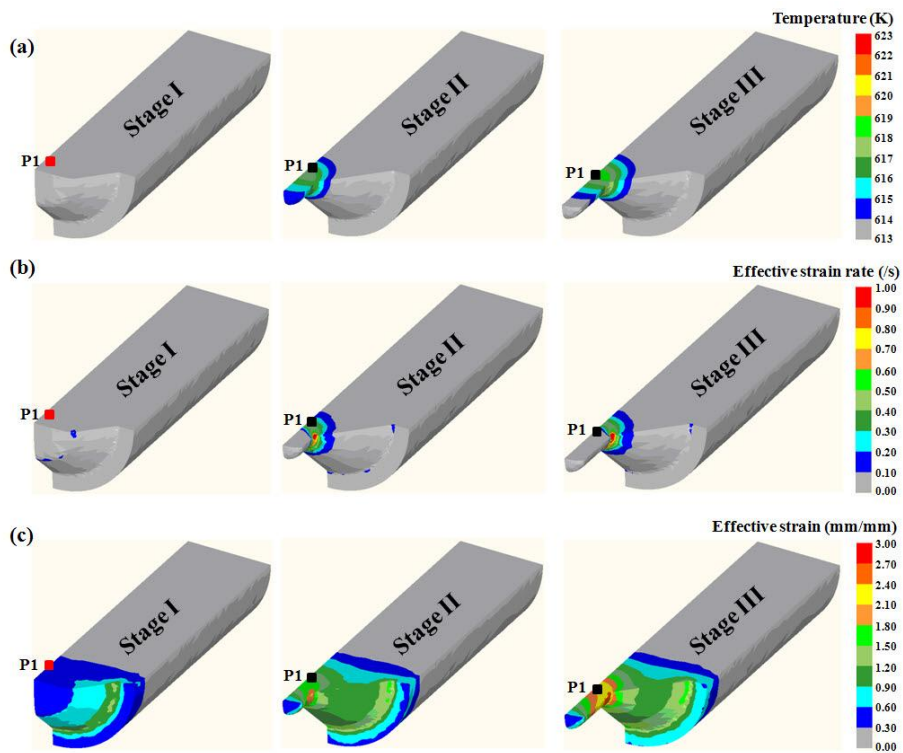


Figure 4.35 Macroscopic extrusion deformation behavior of the ZAM631 alloy at P1 traced during extrusion at 653K; (a) evolution of temperature, (b) evolution of effective strain rate and (c) evolution of effective strain.

4.5 Texture evolution prediction of magnesium alloys during extrusion process

4.5.1 Texture evolution prediction during AZ31 alloy plate (3t) extrusion

In this section, the predicted textures of AZ31 alloy extruded plate (3t) by VPSC-FE model and the experiment are presented in Figures 4.36~4.44. Figure 4.36 (a) shows the location of points at different stages of extrusion. The P1 is at the beginning of the extrusion process, P2 is the middle, and P3 is at the end of the extrusion process. As the extrusion are being performed from P1 to P3 at 533K, the c-axes of many grains in extrusions are being oriented perpendicular to the ED, basal texture, as shown in Figure 4.36 (b). Namely, a number of basal planes of deformed AZ31 alloy are aligning parallel to shearing direction because the basal $\langle a \rangle$ slip has lower CRSS value than those of non-basal slip. Figure 4.37 (b) shows the predicted textures by VPSC-FE model at 533K at the same location in Figure 4.36 (b). As the extrusion is being performed from P1 to P3, the basal planes of grains in extrusions start to be oriented parallel to the ED at P1. And then those of more grains are being oriented parallel to the ED at P2. Those changes are becoming more evident at P3 than P2. The microtextures in Figure 4.36 (b) obtained through EBSD measurements were compared with the macrotextures in Figure 4.37 (b) obtained through VPSC-FE model in Figure 4.38. Owing to the difference in the procedure obtaining the textures in Figures 4.36 (b) and Figure 4.37 (b), the quantitative comparison such as basal pole intensities is not reasonable but the qualitative comparison is very reasonable. The predicted textures in Figure 4.38 (b) are qualitatively in good agreement at all three stages with the experimental results in Figure 4.38 (a). Figure 4.39 shows the macrotexture evolution of the alloy extrusions with the rise in the extrusion temperature. Those textures were measured by XRD at the

temperature range of 573~653K. As the extrusion temperature increases from 573K to 653K, the basal planes are spreading towards the transverse direction (TD). Figure 4.40 shows the predicted texture evolutions by VPSC-FE model at 573K. As the extrusion is being performed from P1 to P3, the basal planes of grains in extrusions start to be oriented parallel to the ED at P1. And then those of more grains are being oriented parallel to the ED at P2. Those orientation changes are becoming more evident at P3 than P2. When the extrusion temperature increases from 573K to 613K and 653K, the texture evolutions at P1 and P2 are the same as at 573K but the basal planes are spread towards the TD at P3 as shown in Figure 4.41 and 4.42. Figure 4.43 shows the predicted texture evolutions at P3 with the rise in the extrusion temperature. The basal planes of grains in the extrusions, which were spread to the ED at 573K, were being spread to the TD with the rise in the extrusion temperature. The measured textures in Figure 4.39 (b) obtained through XRD measurements were compared with the predicted textures in Figure 4.43 (b) obtained through VPSC-FE model in Figure 4.44. The results show that the predicted textures are qualitatively in good agreement at each temperature and the texture evolution changes are also qualitatively in good agreement with the rise in the extrusion temperature.

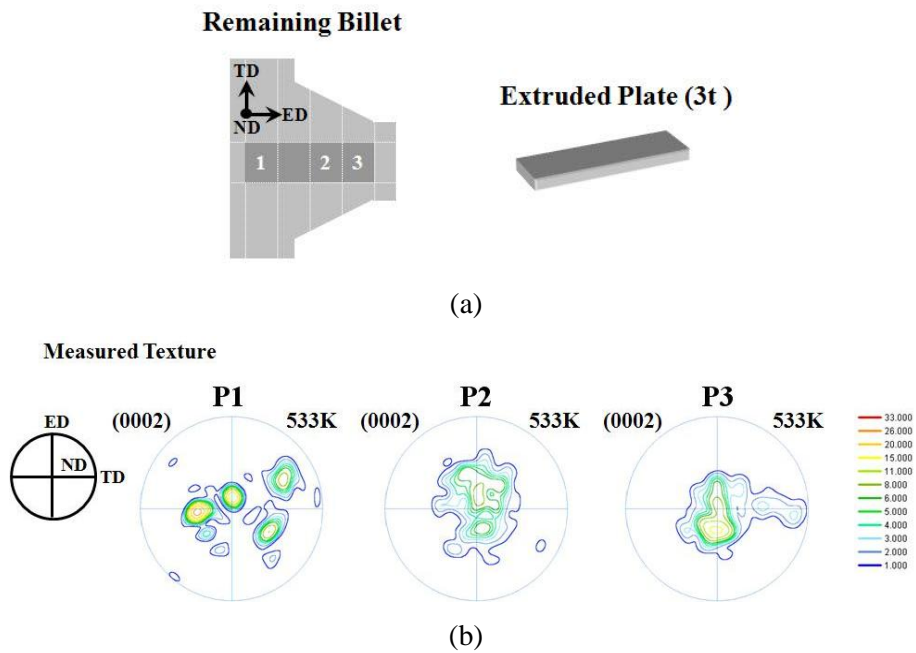


Figure 4.36 Measured texture distributions with the location in the remaining billet of AZ31 alloy extruded plate (3t) at 533K; (a) location of points at different stages of extrusion and (b) measured texture distributions (EBSD) at P1,P2 and P3.

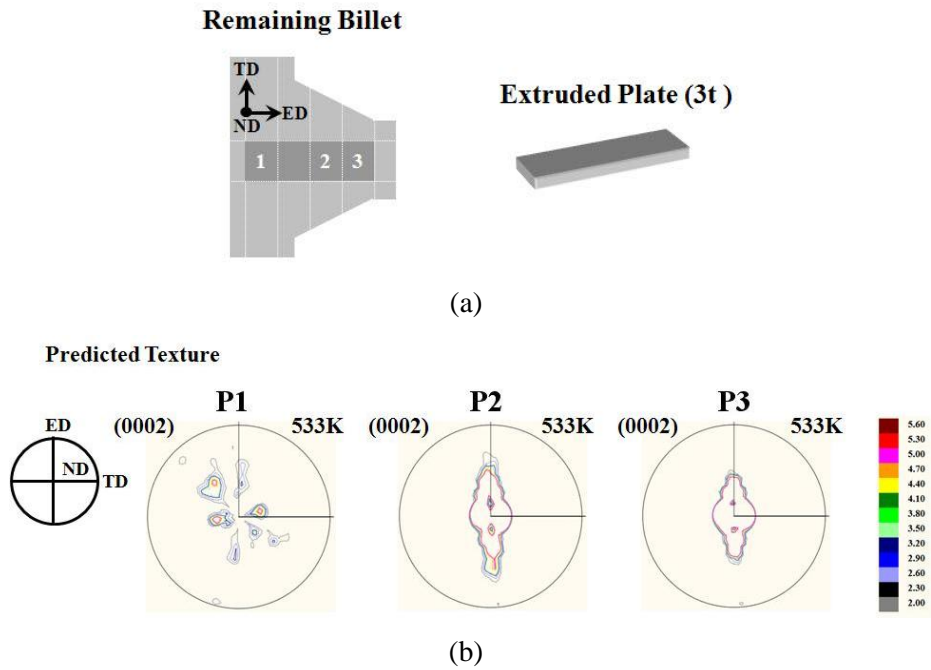


Figure 4.37 Predicted texture distributions with the location in the remaining billet of AZ31 alloy extruded plate (3t) at 533K; (a) location of points at different stages of extrusion and (b) predicted texture distributions (VPSC-FE) at P1,P2 and P3.

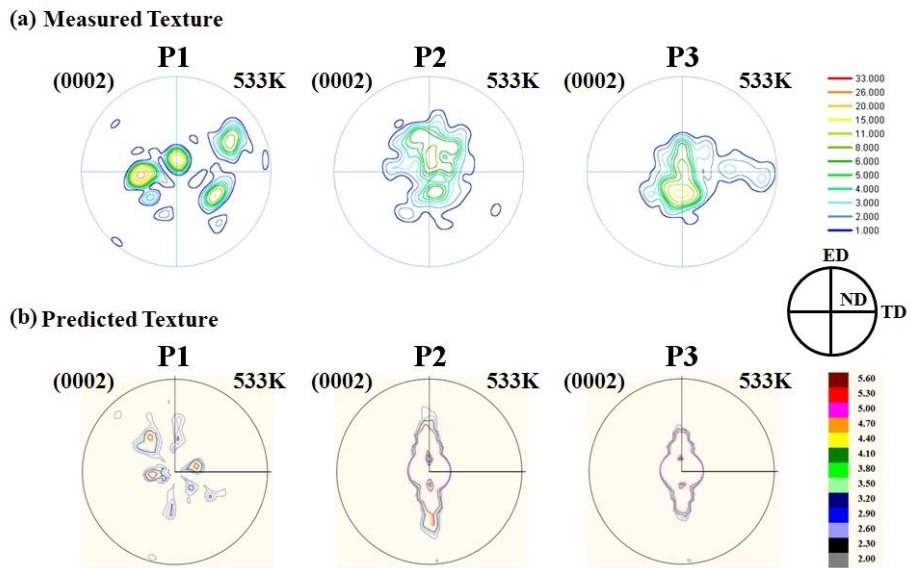


Figure 4.38 Measured texture distributions and predicted texture distributions of AZ31 alloy extruded plate (3t) at 533K; (a) measured texture distributions (EBSD) at P1, P2 and P3 and (b) predicted texture distributions (VPSC-FE) at P1, P2 and P3.

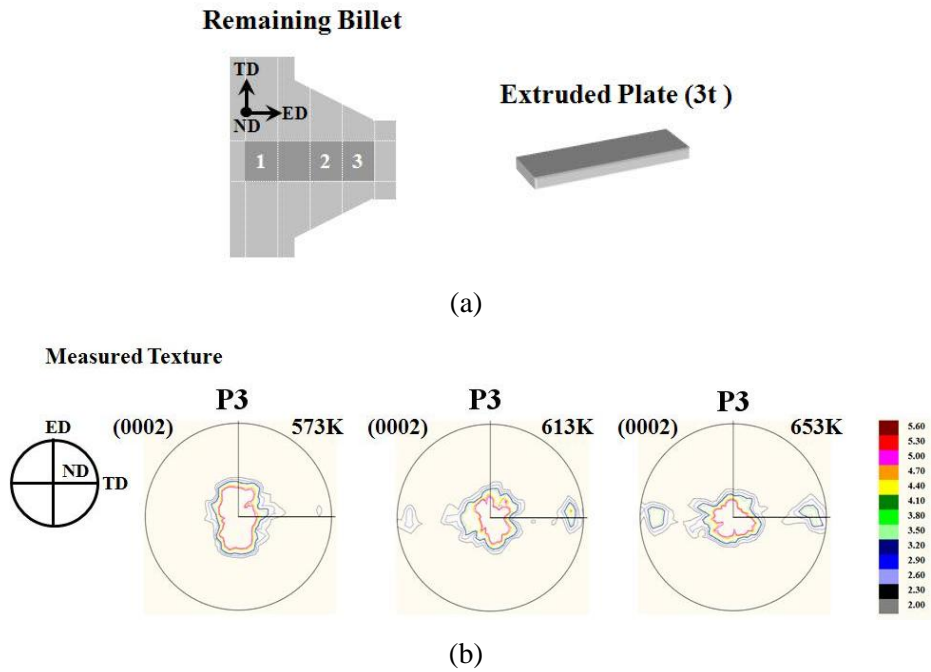


Figure 4.39 Measured texture distributions with the extrusion temperature of AZ31 alloy extruded plate (3t); (a) location of points at different stages of extrusion and (b) measured texture distributions (XRD) at P3.

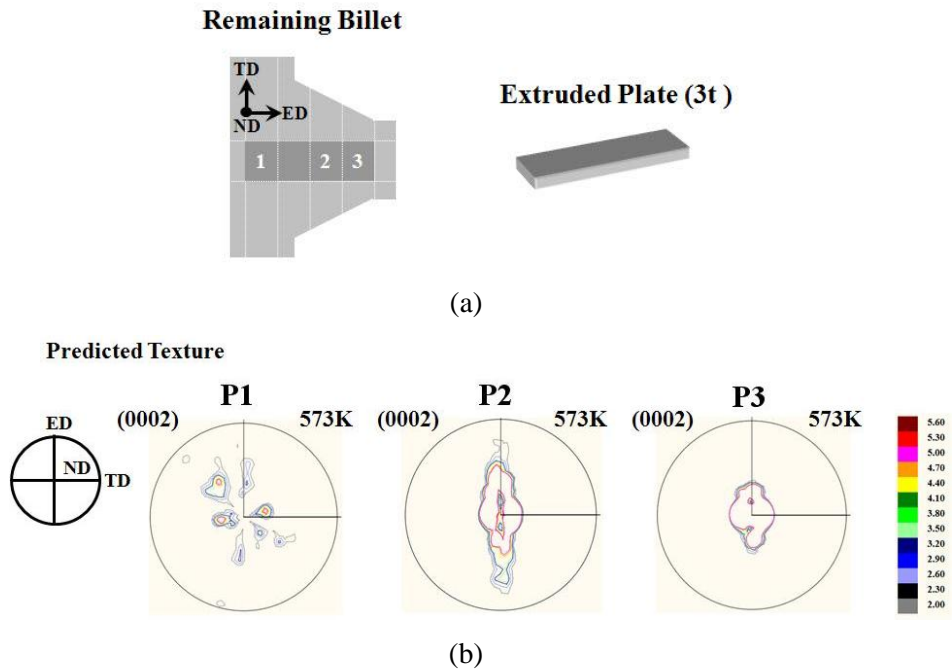


Figure 4.40 Predicted texture distributions with the location in the remaining billet of AZ31 alloy extruded plate (3t) at 573K; (a) location of points at different stages of extrusion and (b) predicted texture distributions (VPSC-FE) at P1,P2 and P3.

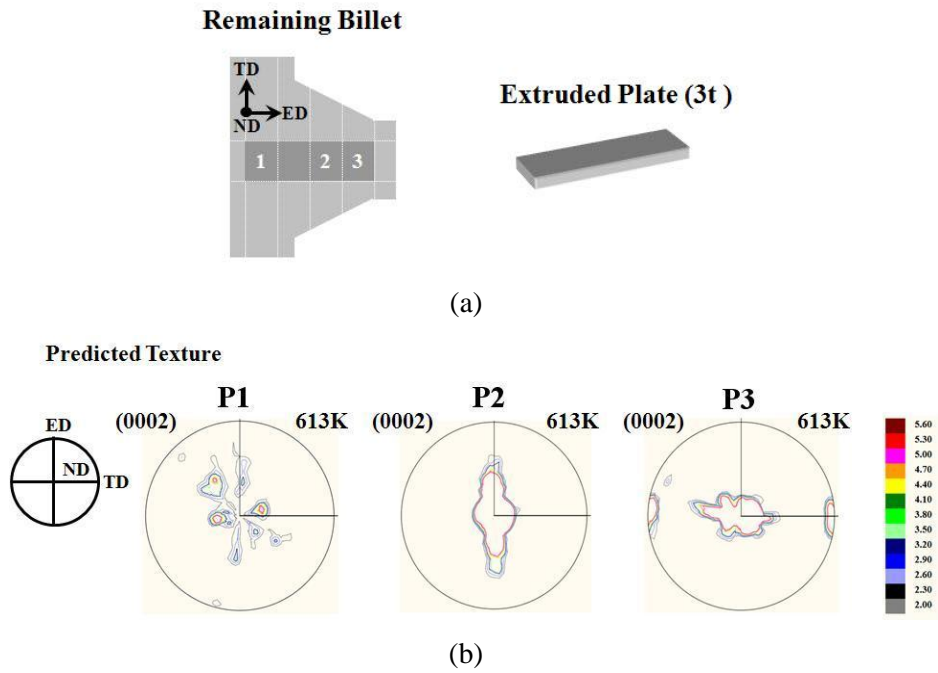


Figure 4.41 Predicted texture distributions with the location in the remaining billet of AZ31 alloy extruded plate (3t) at 613K; (a) location of points at different stages of extrusion and (b) predicted texture distributions (VPSC-FE) at P1,P2 and P3.

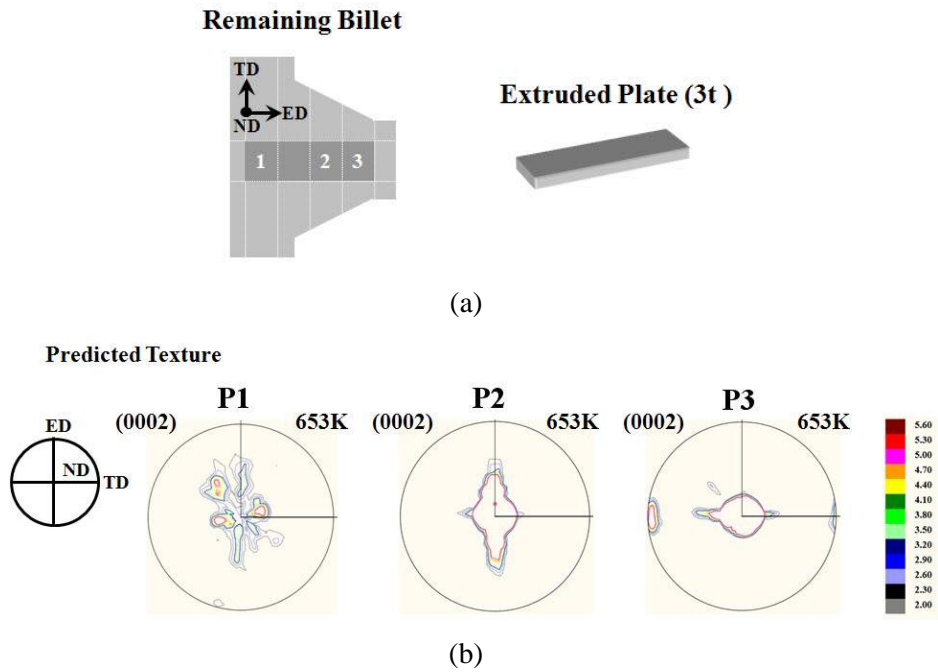


Figure 4.42 Predicted texture distribution with the location in the remaining billet of AZ31 alloy extruded plate (3t) at 653K; (a) location of points at different stage of extrusion and (b) predicted texture distribution (VPSC-FE) at P1, P2 and P3.

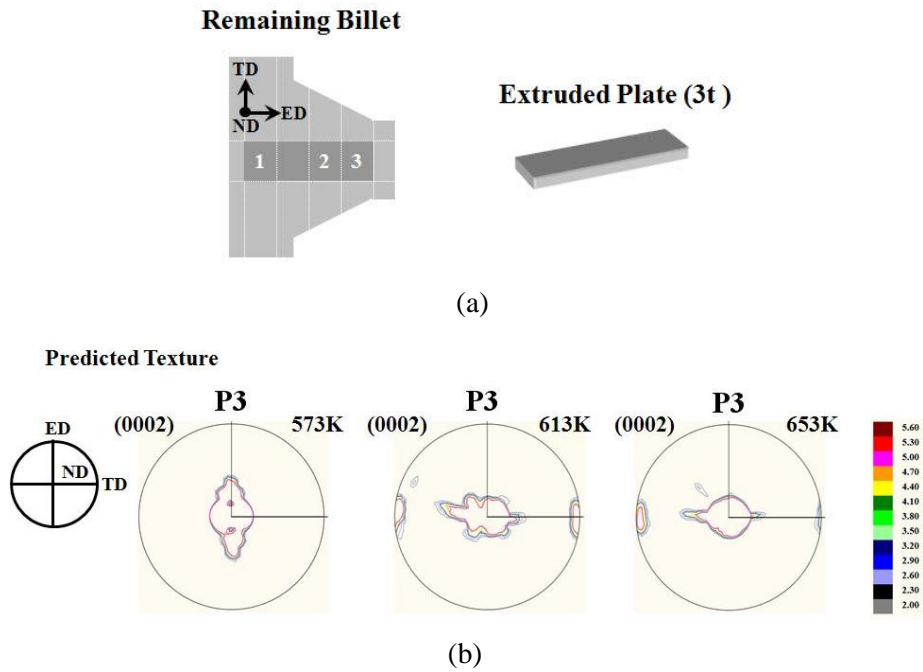


Figure 4.43 Comparison of predicted texture distributions of AZ31 alloy extruded plate (3t) with the extrusion temperature; (a) location of points at different stages of extrusion and (b) predicted texture distributions (VPSC-FE) at P3.

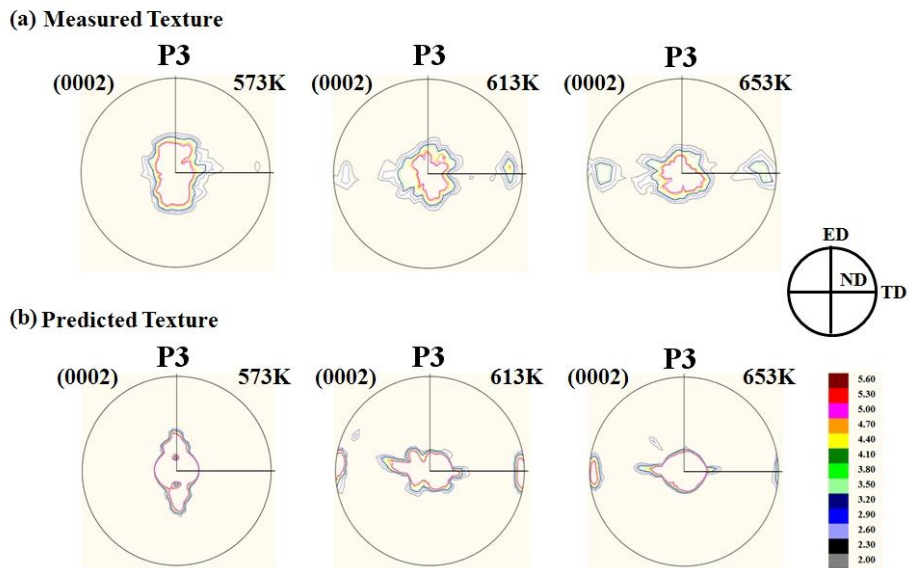


Figure 4.44 Measured texture distributions and predicted texture distributions of AZ31 alloy extruded plate (3t) with the extrusion temperature; (a) measured texture distributions (XRD) at P3 and (b) predicted texture distributions (VPSC-FE) at P3.

4.5.2 Texture evolution prediction during ZAM631 alloy rod (16Φ) extrusion

In this section, the predicted textures of ZAM631 alloy extruded rod (16Φ) by VPSC-FE model and the experiment are presented in Figures 4.45~4.49. Figure 4.45 (a) shows the location of points at different stages of extrusion. The P1 is shortly before at the extrusion die, the P2 is at the beginning of the extrusion process shortly after the entrance of the die, P3 is at the middle, and P4 is at the end of the extrusion process. As the extrusion was performed from P1 to P4 at 533K, the c-axes of many grains in extrusions has been oriented parallel to the ED, basal texture, as shown in Figure 4.45 (b). In particular, a number of basal planes of deformed ZAM631 alloy have been aligned parallel to shearing direction because, the basal $\langle a \rangle$ slip has lower CRSS value than those of non-basal slip. Figure 4.45 (b) shows also the measured textures at 613K at the same location as in the case of 533K. As the extrusion was being performed from P1 to P4, most of the grains in those extrusions have shown that the basal plane is perpendicular to the ED. The texture showed the non-basal texture. Namely, the basal texture at 533K has been changed to the non-basal texture because of the DRX grains with activation of $\langle c+a \rangle$ slip system increasing the extrusion temperature [78]. Figure 4.46 (b) shows the predicted textures by VPSC-FE model at 533K with the location of points at different stages of extrusion. As the extrusion is being performed from P1 to P4, the basal planes of grains in extrusions start to be oriented parallel to the ED at P1. In addition to that, more grains are being oriented parallel to the ED at P2 and P3. Those changes are becoming more evident at P4 than P3. Figure 4.46 (b) shows well the process of basal texture formation at 533K. Figure 4.47 (b) shows the predicted textures by VPSC-FE model at 613K at the same location in Figure 4.46 (b). As the extrusion is being performed from P1 to P4, the basal planes of grains in extrusions start

to be oriented parallel to the ED at P1. And then those of more grains are being oriented parallel to the ED at P2. Those of some grains are being oriented perpendicular to the ED at P3. Those changes are becoming more evident at P4 than P3. Figure 4.47 (b) shows the changing process of basal texture to the non-basal texture formation at 613K. Figure 4.48 shows qualitatively the change of predicted texture evolutions with the basal texture to the non-basal texture at P4 with increasing from 573K to 653K. The measured textures in Figure 4.45 (b) obtained through XRD measurements were compared with the predicted textures in Figure 4.48 (b) obtained through VPSC-FE model in Figure 4.49. The results show that the predicted texture is qualitatively in good agreement at 533K but is different from the experiment at 613K. However different it may be from the experiment at 613K, the trend for the basal texture to be changed to the non-basal texture is qualitatively in agreement.

In this study, VPSC-FE model considered the flow softening caused by DRX during extrusion, with imposing the computed velocity gradient on each of magnesium alloy polycrystals, then update the shape, orientation and hardening of the individual grains. In fact, the considered alloys have experienced the microstructure change by DRX during extrusion. The volume fraction of DRX found to change but it was not considered in this model. The measured texture of specimen compressed to the true strain of -0.357 was obtained through XRD measurement and was compared with the predicted texture obtained from VPSC-FE model (Figure 4.50). The results showed that the shape of the pole figure is different, however, the trend for the basal texture to be changed to the non-basal texture is similar and the maximum pole intensity of the predicted texture is much higher than that of the experiment. These discrepancies could be mainly ascribed to not accounting for the change of volume fraction of DRX.

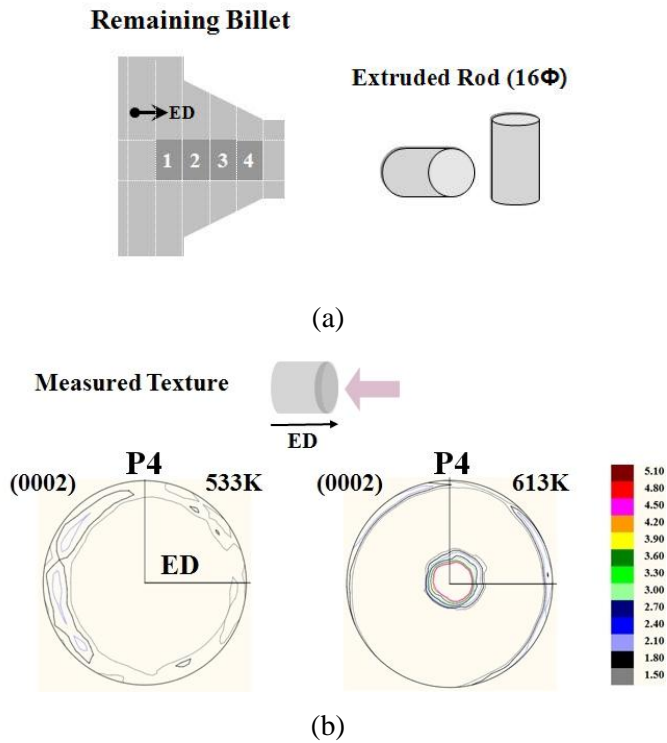


Figure 4.45 Measured texture distributions with the extrusion temperature of ZAM631 alloy extruded rod (16Φ); (a) location of points at different stages of extrusion and (b) measured texture distributions (XRD) at P4.

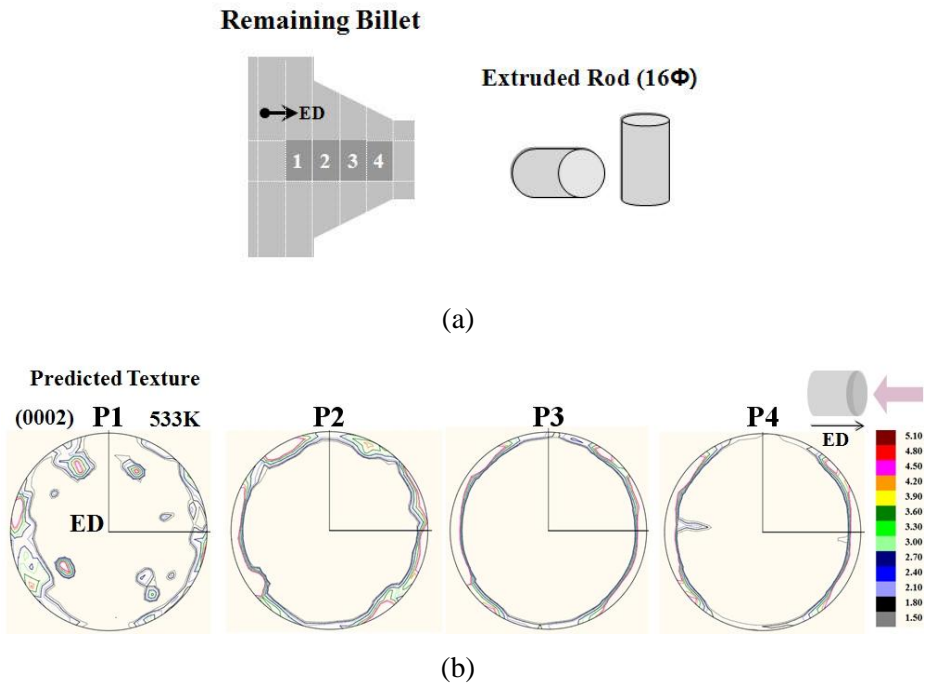


Figure 4.46 Predicted texture distributions with the location of remaining billet in ZAM631 alloy extruded rod (16Φ) at 533K; (a) location of points at different stages of extrusion and (b) predicted texture distributions (VPSC-FE) at P1, P2, P3 and P4.

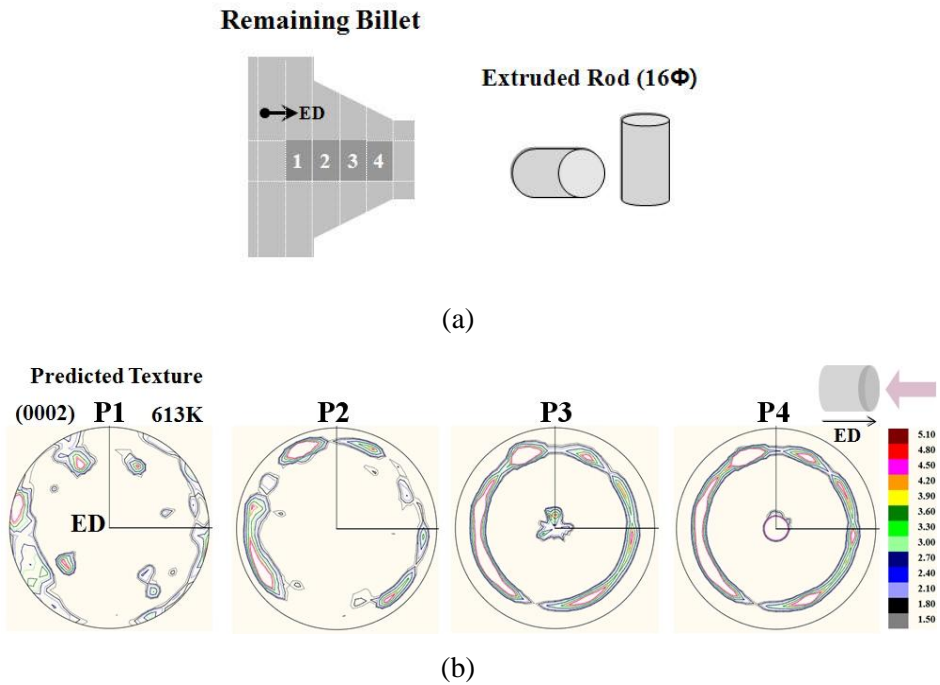


Figure 4.47 Predicted texture distributions with the location of remaining billet in ZAM631 alloy extruded rod (16Φ) at 613K; (a) location of points at different stages of extrusion and (b) predicted texture distributions (VPSC-FE) at P1, P2, P3 and P4.

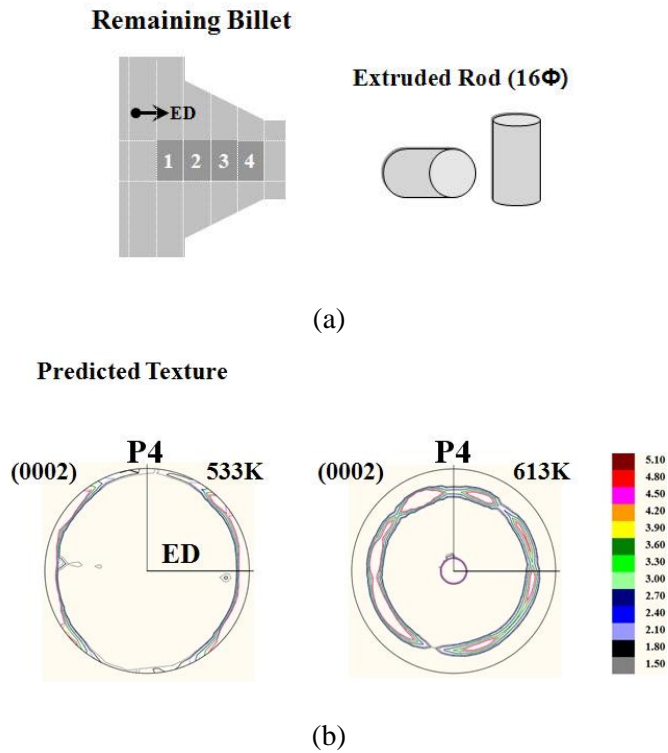


Figure 4.48 Predicted texture distributions with the extrusion temperature of ZAM631 alloy extruded rod (16Φ); (a) location of points at different stages of extrusion and (b) predicted texture distributions (XRD) at P4.

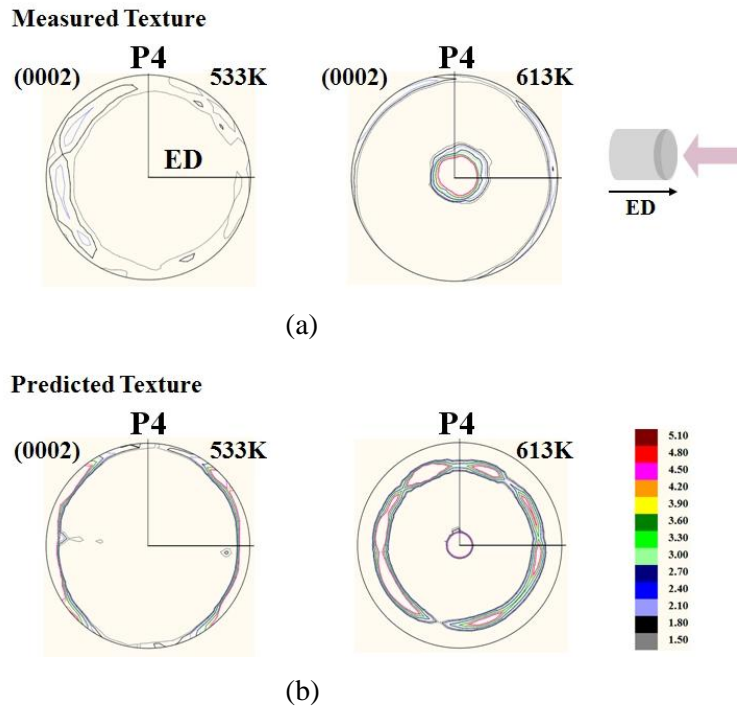


Figure 4.49 Measured texture distributions and predicted texture distributions with the extrusion temperature of ZAM631 alloy extruded rod (16 Φ); (a) measured texture distributions (XRD) at P4 and (b) predicted texture distributions (VPSC-FE) at P4.

Chapter 5. Conclusions

In order to analyze the effects of extrusion temperature and strain rate on the extrusion deformation behavior of magnesium alloys, the flow properties of AZ31 and ZAM631 alloy were investigated at the conditions with the temperature of 533~653K and the strain rate of 10^{-3} ~1/s. Using the VPSC model, the CRSS value of the major slip and twinning modes for AZ31 and ZAM631 alloy undergoing compressive deformation have been systematically analyzed as a function of temperature. A non-iso-thermal three-dimensional rigid-plastic FEM simulation of indirect extrusion process was carried out to analyze the macroscopic deformation behavior during extrusion. The texture evolution during extrusion was predicted with new methodology to connect the macroscopic deformation behavior to the microscopic deformation behavior and the following conclusions can be made:

- (1) Using the VPSC-GA optimizations, the macroscopic compressive stress-strain curves successfully were simulated, and the effect of temperature on the CRSS values of the various deformation modes was found. The results show that the basal slip and tensile twinning were weakly temperature dependent, whereas the prismatic slip, $\langle c+a \rangle$ slip and compressive twinning were strongly temperature dependent, in other words, decreased with increasing temperature at the temperature range of 533~653K.
- (2) The flow curves of both AZ31 and ZAM631 alloy exhibited typical flow behaviors with dynamic softening. The peak stress of both AZ31 and ZAM631 alloy decreased with increasing the deformation temperature from 533K to 653K at constant strain rate and increased with increasing the strain rate from 10^{-3} /s to 1/s at constant temperature.

- (3) The dynamic softening during compressive deformation is mainly caused by the dynamic recrystallization (DRX). The DRX of both AZ31 and ZAM631 alloy depends on the process temperature and strain rate. The average size of DRX grains (D_{drx}) is formulated as a function of the Zener-Hollomon parameter as Eq. (4.2) and Eq. (4.17). It increased with decreasing Z .
- (4) The flow stress of both AZ31 and ZAM631 alloy during high temperature deformation can be represented by Eq. (4.16). The parameters of Ψ and ζ and the strain softening exponents were determined. The activation energy for deformation can be calculated 187kJ/mol for AZ31 alloy 252kJ/mol for ZAM631 alloy respectively.
- (5) The macroscopic deformation behavior of magnesium alloys (AZ31 and ZAM631) with extrusion temperature has been successfully analyzed. The macroscopic variables such as temperature, strain rate and strain showed the similar deformation behavior at the considered temperature range (533~653K).
- (6) The new methodology for texture evolution prediction during extrusion has been proposed. This methodology presents a physically based approach to connect the macroscopic behavior to the microscopic behavior. The predictions of texture evolution during extrusion of magnesium alloys (AZ31 and ZAM631) have been performed by using VPSC-FE model. The predictions show qualitatively good agreement with the experimental results.

Bibliography

- [1] E. Aghion, B. Bronfin and D. Eliezer, “The Role of the Magnesium Industry in Protecting the Environment”, *J. Mater. Process. Tech.*, 117 (2001), pp. 381-385.
- [2] H. Friedrich and S. Schumann, “Research for a “New Age of Magnesium”, in the Automotive Industry”, *J. Mater. Process. Tech.*, 117 (2001), pp. 276-281.
- [3] H. Furuya, N. Kogiso, S. Matunaga and K. Senda, “Applications of Magnesium Alloys for Aerospace Structure Systems”, *Mater. Sci. Forum* 350-351 (2000), pp 341-348.
- [4] B.L. Mordike and T. Ebert, “Magnesium Properties-Application-Potential”, *Mater. Sci. Eng. A*, 302 (2001), pp. 37-45.
- [5] X.Y. Lou, M. Li, R.K. Boger, S.R. Agnew and R.H. Wagoner, “Hardening Evolution of AZ31B Mg Sheet”, *Int. J. Plasticity*, 19 (2007), pp. 1843-1864.
- [6] C. Roucoules, S. Yue and J.J. Jonas, “Effect of Alloying Elements on Metadynamic Recrystallization in HSLA steels”, *Metall. Mater. Trans. A*, 26 (1995), p. 181.
- [7] C. Roucoules, P.D. Hodgson, S. Yue and J.J. Jonas, “Softening and Microstructural Change Following the Dynamic Recrystallization of Austenite”, *Metall. Mater. Trans. A*, 25 (1994) 389.
- [8] L. Liu, H. Zhou, Q. Wang, Y. Zhu and W. Ding, “Dynamic Recrystallization Behavior of AZ61 Magnesium Alloy,” *Azjomo* (DOI:10.2240 / azojomo0211), 2 (2006), pp. 1-12.
- [9] M. Mabuchi, K. Ameyama, H. Iwasaki and K. Higashi, “Low Temperature Superplasticity of AZ91 Magnesium Alloy with Non-Equilibrium Grain Boundaries”, *Acta Mater.*, 47 [7] (1999) p. 2047.
- [10] J. Liu, Z. Cui and C. Li, “Modeling of Flow Stress Characterizing Dynamic Recrystallization for Magnesium Alloy AZ31B”, *Comp. Mater.*

- Sci., 41 (2008), pp. 375-382.
- [11] N.V. Ravi Kumar, J.J. Blandin, C. Desrayaud, F. Montheillet and N. Suery, "Grain Refinement in AZ91 Magnesium Alloy during Thermo-mechanical Processing", *Mater. Sci. Eng. A*, 359 (2003), pp. 150-157.
- [12] B.M. Closset, J.F. Perey, C. Bonjour and P.A. Moos, "Microstructures and Properties of Wrought Magnesium Alloys, Magnesium Alloys and Their Applications", Wiley-VCH, Weinheim, 1998, pp. 195-200.
- [13] G. Liu, J. Zhou and J. Duszczyk, "Prediction and Verification of Temperature Evolution as a Function of Ram Speed during the Extrusion of AZ31 Alloy into a Rectangular Section", *J. Mater. Process. Tech.*, 117 (2001), pp. 381-385. .
- [14] A.G. Beer and M.R. Barnett, "The Hot Working Flow Stress and Microstructure in Magnesium AZ31", *Magnesium Technology 2002*, TMS (The Minerals, Metals & Materials Society) 2002, pp. 193-198.
- [15] N. Ogawa, M. Shiomi and K. Osakada, "Forming Limit of Magnesium Alloy at Elevated Temperatures for Precision Forging", *Int. J. Mach. Tool. Manu.*, 42 (2002), pp. 607-614.
- [16] T. Laser, Ch. Hartig, M.R. Nurnberg, D. Letzig and R. Bormann, "The Influence of Calcium and Cerium Mischmetal on the Microstructural Evolution of Mg-3Al-1Zn during Extrusion and Resulting Mechanical Properties", *Acta Mater.*, 56 (2008), pp. 2791-2798.
- [17] S.S. Park, B.S. You and D.J. Yoon, "Effect of the Extrusion Conditions on the Texture and Mechanical Properties of Indirect-Extruded Mg-3Al-1Zn Alloy", *J. Mater. Process. Tech.*, 209 (2009), pp. 5940-5943.
- [18] R.A. Lebensohn and C.N. Tome, "A Self-Consistent Visco-plastic Model: Prediction of Rolling Textures of Anisotropic Polycrystals", *Mater. Sci. Eng. , A* 175 (1994), pp. 71-82.
- [19] S. Graff, W. Brocks and D. Steglich, "Yielding of Magnesium: from Single Crystal to Polycrystalline Aggregates", *Int. J. Plasticity.*, 23 (2007), pp. 1957-1978.

- [20] D. Steglich, Y. Jeong, M.O. Andar and T. Kuwabara, "Biaxial Deformation Behavior of AZ31 Magnesium Alloy: Crystal-Plasticity-Based Prediction and Experimental Validation", *Int. J. Solids Struct.*, 49 (25) (2012), pp. 3551-3561.
- [21] Z. Yand, J.P. Li, J.X. Zhang, G.W. Lorimer and J. Robson, "Review on Research and Development of Magnesium Alloys", *Acta Metall. Sin. (Engl. Lett.)*, 21 (5) (2008), pp. 313-328.
- [22] C.J. Bettles and M.A. Gibson, "Current Wrought Magnesium Alloys: Strengths and Weaknesses", *JOM*, May (2005), pp. 46-49.
- [23] M.M. Avedesian and H. Baker, "Magnesium and Magnesium Alloys", *ASM Specialty Handbook*, (1999), pp. 313-328.
- [24] L.L. Rokhlin, "Magnesium Alloys Containing Rare Earth Metals-Structure and Properties", Taylor & Francis Pub, (2003), p. 197.
- [25] H. Wang, P.D. Wu, C.N. Tome and J. Wang, "A Constitutive Model of Twinning and Detwinning for Hexagonal Close Packed Polycrystals", *Mater. Sci. Eng. A*, 555 (2012), pp. 93-98.
- [26] C.M. Byer, B.Li, B. Cao, and K.T. Ramesh, "Microcompression of Single-Crystal Magnesium", *Scripta Mater.*, 62 (2010), pp. 536-539.
- [27] S.R. Agnew, C.N. Tome, D.W. Brown, T.M. Holden and S.C. Vogel, "Study of Slip Mechanism in a Magnesium Alloy by Neutron Diffraction and Modeling", *Scripta Mater.*, 48 (2003), pp. 1003-1008.
- [28] M.H. Yoo, "Slip, Twinning, and Fracture in Hexagonal Close-Packed Metals", *Metall. Mater. Trans. A*, 12A (1981), pp 409-418.
- [29] M.H. Yoo, S.R. Agnew, J.R. Morris and K.M. Ho, "Non-basal Slip Systems in HCP Metals and Alloy: Source Mechanisms", *Mater. Sci. Eng. A*, 319-321 (2001), pp. 87-92.
- [30] H. Yang, S. Yin, C. Huang, Z. Zhang, S. Wu, S. Li and Y. Liu, "EBSD Study on Deformation Twinning in AZ31 Magnesium Alloy during Quasi-in-Situ Compression", *Adv. Eng. Mater.*, 10 (10) (2003), pp. 955-960.

- [31] S. Kleiner, P.J. Uggowitzer, “Mechanical Anisotropy of Extruded Mg-6% Al-1% Zn alloy”, *Mater. Sci. Eng., A* 379 (2004), pp. 258-268.
- [32] J. Koike, “Enhanced Deformation Mechanisms by Anisotropic Plasticity in Polycrystalline Mg Alloys at Room Temperature”, *Metall. Mater. Trans. A* 36A (2005), pp. 1689-1696.
- [33] W.J. Ai, G. Fang, J. Zhou, M.A. LeeFlang and J. Duszczyc, “Effect of Twinning on the Deformation Behavior of an Extruded Mg-Zn-Zr Alloy during Hot Compression Testing”, *Mater. Sci. Eng. A*, 556 (2012), pp. 373-381.
- [34] T. Al-Samman and G. Gottstein, “Dynamic Recrystallization during High Temperature Deformation of Magnesium”, *Mater. Sci. Eng. A*, 490 (2008), pp. 411-420.
- [35] S.W. Xu, K. Oh-ishi, H. Sunohara and S. Kamado, “Extruded Mg-Zn-Ca-Mn alloys with Low Yield Anisotropy”, *Mater. Sci. Eng., A* 558 (2012), pp. 356-365.
- [36] M. Wang, R. Xin, B. Wang and Q. Liu, “Effect of Initial Texture on Dynamic Recrystallization of AZ31 Mg Alloy during Hot Rolling”, *Mater. Sci. Eng., A* 528 (2011), pp. 2941-2951.
- [37] I. J. Beyerlein, L. S. Toth, “Texture Evolution in Equal-Channel Angular Extrusion”, *Prog. Mater. Sci.*, 54 (2009), pp. 427-510.
- [38] L. Delannay, “Observation and Modeling of Grain Interactions and Grain Subdivision in Rolled Cubic Polycrystals”, Ph. D Thesis (2001), p. 16.
- [39] S.B. Yi, “Investigation on the Deformation Behavior and the Texture Evolution in Magnesium Wrought Alloy AZ31”, Ph. D Thesis (2005), p. 25.
- [40] P.R. Dawson, S.R. MacEwen and P.D. Wu, “Advances in Sheet Metal Forming Analyses: Dealing with Mechanical Anisotropy from Crystallographic Texture”, *Int. Mater. Rev.*, 48 (2003), pp. 86–122.
- [41] P. Eyckens, A.V. Bael and P.V. Houtte, “Marciniak–Kuczynski Type

- Modelling of the Effect of Through-Thickness Shear on the Forming Limits of Sheet Metal”, *Int. J. Plasticity.*, 25 (2009), pp. 2249–2268.
- [42] J. Levesque, K. Inal, K.W. Neale and R.K. Mishra, “Numerical Modeling of Formability of Extruded Magnesium Alloy Tubes”, *Int. J. Plasticity.* 26 (2010), pp. 65–83.
- [43] Z. Chen, X. Zhang, C. Liu, H. Cai and F. Wang, “Computer simulation of Rolling Textures Evolution of Pure Aluminum with Initial Texture”, *Mater. Trans.*, 45 (9) (2004), pp. 2845-2850.
- [44] B. Clausen, C.N. Tome, D.W. Brown and S.R. Agnew, “Reorientation and Stress Relaxation due to Twinning: Modeling and Experimental Characterization for Mg”, *Acta Mater.*, 56 (2008), 2456-2468.
- [45] R.A. Lebensohn and C.N. Tome, “A Self-Consistent Anisotropic Approach for the Simulation of Plastic Deformation and Texture Development of Polycrystals: Application to Zirconium Alloys”, *Acta Metall. Mater.*, 41 (1993), pp. 2611-2624.
- [46] V. Boljanovic, “Metal Shaping Processes”, Industrial Press, (2010), pp. 179-180.
- [47] H.S. Valberg, “Applied Metal Forming”, Cambridge University Press, (2010), pp. 23-26.
- [48] K. Laue and H. Stenger, “Extrusion”, American Society for Metals, (1981), pp. 75-76.
- [49] L.P. Lei, “Analysis and Design of Hydroforming Processes by the Rigid-Plastic Finite Element Method”, Ph. D Thesis (2000), pp. 15-16.
- [50] Y.B. Park, “Rigid-Plastic Finite Element Analysis of Three-Dimensional Forming with Recurrent Boundary Conditions”, Ph. D Thesis (1995), pp. 3-6.
- [51] X. Zhang and Y. Cheng, “Tensile Anisotropy of AZ91 Magnesium Alloy by Equal Channel Angular Processing”, *J. Alloy Compd.*, 622 (2015), pp. 1105-1109.
- [52] X. Xia, Q. Chen, Z. Zhao, M. Ma, X. Li and K. Zhang “Microstructure,

- Texture and Mechanical Properties of Coarse-Grained Mg-Gd-Y-Nd-Zr Alloy Processed by Multidirectional Forging”, *J. Alloy Compd.*, 623 (2015), pp. 62-68.
- [53] A. Azushima, R. Kopp, A. Korhonen, D.Y. Yang, F. Micari, G.D. Lahoti, P. Groche, J. Yanagimoto, N. Tsuji, A. Rosochowski and A. Yanagida, “Severe Plastic Deformation (SPD) Process for Metals”, *CIRP Ann.-Manuf. Techn.*, 57 (2008), pp. 716-735.
- [54] D.F. Zhang, H.J. Hu, F.S. Pan, M.B. Yang and J.P. Zhang, “Numerical and Physical Simulation of New SPD method Combining Extrusion and Equal Channel Angular Pressing for AZ31 Magnesium Alloy”, *T. Nonferr. Metal. Soc.*, 20 (2010), pp. 478-483.
- [55] S.R. Agnew, M.H. Yoo and C.N. Tome, “Application of Texture Simulation to Understanding Mechanical Behavior of Mg and Solid Solution Alloys Containing Li or Y”, *Acta Mater.*, 49 (2001), pp. 4277-4289.
- [56] R.A. Lebensohn and C.N. Tome, “A Self-Consistent Viscoplastic Model: Prediction of Rolling Textures of Anisotropic Polycrystals”, *Mater. Sci. Eng. A*, 175 (1994), pp. 71-82.
- [57] S.B. Yi, C.H.J. Davies, H.G. Brokmeier, R.E. Bolmaro, K.U. Kainer and J. Homeyer, “Deformation and Texture Evolution in AZ31 Magnesium Alloy during Uniaxial Loading”, *Acta Mater.*, 54 (2006), pp. 549-562.
- [58] S.H. Choi, E.J. Shin and B.S. Seong, “Simulation of Deformation Twins and Deformation Texture in an AZ31 Mg Alloy under Uniaxial Compression”, *Acta Mater.*, 55 (2007), pp. 4181-4192.
- [59] M.M. Avedesian and H. Baker, “ASM Specialty Handbook: Magnesium and Magnesium Alloys”, *ASM Int.* (1999), pp. 26-27.
- [60] J.B. Lin, Q.D. Wang, M.P. Liu, Y.J. Chen and J.R. Hans, “Finite Element Analysis of Strain Distribution in ZK60 Mg Alloy during Cyclic Extrusion and Compression”, *T. Nonferr. Metal. Soc.*, 22 (2012), 1902-1906.

- [61] S.Y. Huang, S.R. Zhang, D.Y. Li and Y.H. Peng, "Modeling Texture Evolution during Rolling Process of AZ31 magnesium alloy with Elasto-Plastic Self Consistent Model", *T. Nonferr. Metal. Soc.*, 21 (2011), 1348-1354.
- [62] A. Srikanth and N. Zabarar, "Shape Optimization and Perform Design in Metal Forming Processes", *Comput. Method. Appl. M.* 190 (2000) 1859-1901.
- [63] X.Y. Lou, M. Li, R.K. Boger, S.R. Agnew and R.H. Wagoner, "Hardening Evolution of AZ31B Mg Sheet", *Int. J. Plasticity*, 23 (1) (2007), pp.44-86.
- [64] A. Jain, O. Duygulu, D.W. Brown, C.N. Tome and S.R. Agnew, "Grain Size Effects on the Tensile Properties and Deformation Mechanisms of a Magnesium Alloy, AZ31B, Sheet", *Mater. Sci. Eng. A*, 486 (1-2) (2008), pp. 545-555.
- [65] Y. Chino, K. Kimura and M. Mabuchi, "Twinning Behavior and Deformation Mechanisms of Extruded AZ31Mg Alloy", *Mater. Sci. Eng. A*, 486 (1-2) (2008), pp. 481-488.
- [66] G.Y. Chin and W.L. Mammel, "Competition among Basal, Prism and Pyramidal Slip Modes in HCP Metals", *Metall. Trans.*, 1 (1970), pp. 357-361.
- [67] S.R. Agnew, C.N. Tome, D.W. Brown, T.M. Holden, and S.C. Vogel, "Study of Slip Mechanisms in a Magnesium Alloy by Neutron Diffraction and Modeling", *Scripta Mater*, 48 (8) (2003), pp. 1003-1008.
- [68] M.R. Barnett, "A Taylor Model Based Description of the Proof Stress of Magnesium AZ31 during Hot Working", *Metall. and Mater. Trans. A*, 34A (9) (2003), pp. 1799-1806.
- [69] A. Fernandez, M.T.P. Prado, Y. Wei and A. Jerusalem, "Continuum Modeling of the Response of Mg Alloy AZ31 Rolled Sheet during Uniaxial Deformation", *Int. J. Plasticity*, 27 (2011), pp. 1739-1757.
- [70] M.Z. Bian, "Plastic Deformation Behavior of Magnesium Single

- Crystals”, Ph. D Thesis (2013), p. 58.
- [71] J.C. Tan and M.J. Tan, “Dynamic Continuous Recrystallization Characteristics in Two Stage Deformation of Mg-3Al-1Zn Alloy Sheet”, *Mater. Sci. Eng. A*, 339 (2003), pp. 124-132.
- [72] S.M. Fatemi-Varzaneh, A. Zarei-Hanzaki and H. Beladi, “Dynamic Recrystallization in AZ31 Magnesium Alloy”, *Mater. Sci. Eng. A*, 456 (2007), pp. 52-57.
- [73] H.Y. Wu, J.C. Yang, F.J. Zhu and H.C. Liu, “Hot Deformation Characteristics of As-Cast and Homogenized AZ61 Mg Alloys under Compression”, *Mater. Sci. Eng. A*, 550 (2012), pp. 273-278.
- [74] F.J. Humphreys and M. Hatherly, “Recrystallization and Related Annealing Phenomena”, Elsevier, 2nd Edition (2004), pp. 11-450.
- [75] F. Grosman, “Flow Stress Functions for the Computer Simulation of Metal Forming”, *J. Mater. Process. Tech.*, 106 (2000), pp. 45-48.
- [76] Z.P. Zeng, S. Jonssons, H.J. Roven and Y.S. Zhang, “Modeling the Flow Stress for Single Peak Dynamic Recrystallization”, *Mater. Design*, 30 (6) (2009), pp. 1939-1943.
- [77] R. Ebrahimi and S. Solhjo, “Characteristic Points of Stress-Strain Curve at High Temperature”, *Int. J. ISSI*, 4 (1-2) (2007), pp. 24-27.
- [78] J.H. Hwang, “Effects of Alloying Elements and Extrusion Condition on Texture and Mechanical Properties of Wrought Magnesium Alloys”, Ph. D Thesis (2010), pp. 121-123.

Appendix

A. Hot flow stress user subroutine for AZ31 alloy in DEFORM system

The below subroutine was coded with Absoft 11.0 Fortran compiler based on the flow stress model expressed as a function of plastic strain, strain rate and temperature defined by the compressive stress-strain curves measured using a Gleeble machine at the temperature range of 533-653K with the strain rate range of 10^{-3} ~1/s.

```
C*****
```

```
      SUBROUTINE USRMTR (NPTRTN,YS,YPS,FIP,TEPS,EFEPS,TEMP)
```

```
C*****
```

```
C
```

```
C   THIS SUBROUTINE CALCULATES THE FLOW STRESS OF PLASTIC MATERIAL
```

```
C
```

```
C   INPUT :
```

```
C
```

```
C   NPTRTN  =  FLOW STRESS NUMBER
```

```
C   TEPS    =  EFFECTIVE STRAIN
```

```
C   EFEPS   =  EFFECTIVE STRAIN RATE
```

```
C   TEMP    =  TEMPERATURE
```

```
C
```

```
C   OUTPUT :
```

```
C
```

```
C   YS      =  FLOW STRESS
```

```
C   YPS     =  DERIVATIVE OF FLOW STRESS W.R.T TEPS
```

```
C   FIP     =  DERIVATIVE OF FLOW STRESS W.R.T EFEPS
```

```
C
```

```
C*****
```

```
      IMPLICIT REAL*8 (A-H,O-Z), INTEGER*4 (I-N)
```

```
C
```

```
C   USER SUPPLIED SUBROUTINES
```

```

C
C
C ****      USER DEFINED VARIABLES ****
C
      CHARACTER*80 IUSRVL
      COMMON /IUSR/ IUSRVL(10)
C
C      TO READ DATA (10 RESERVED LINES)
C      READ(IUSRVL(LINE NUMBER),*) DATA1,DATA2,DATA3...
C
C      TO WRITE DATA (10 RESERVED LINES)
C      WRITES (IUSRVL(LINE NUMBER),*) NEWDATA1, NEWDATA2, NEWDATA3 ...
C
C ****      END      ****
C
C
C
C      COMMON /ELMCOM/ RZE(2,4),URZE(2,4),STSE(4),EPSE(4),EFEPSE,EFSTSE,
C      +                TEPSE,RDTYE,TEMPE(4),DTMPE(4),USRE1(2),USRE2(2),
C      +                NODEE (4), KELE
C
C
C
C      COMMON /ELMCOM/
C
C      RZE      : Four corners coordinates
C      URZE     : Velocity
C      STSE     : Stress
C      EPSE     : Strain rate
C      EFEPSE   : effective strain rate
C      EFSTSE   : Effective stress
C      TEPSE    : Total effective strain
C      RDTYE    : Density
C      TEMPE    : Temperature
C      DTMPE    : Temperature rate
C      DAMAGE   : Damage value
C      USRE1    : Element user state variable 1
C      USRE2    : Element user state variable 2
C      USRNE    : Nodal user state variables 1,2 at 4 nodes
C      NODEE    : Connectivity
C      KELE     : Global element number
C      KELEL    : Local element number

```

```

C          KGROUP   : Material group number
C
COMMON /ELMCOM/ RZE(2,4),URZE(2,4),STSE(4),EPSE(4),EFEPSE,EFSTSE,
+          TEPSE,RDTYE,TEMPE(4),DTMPE(4),DAMAGE,
+          USRE1(1500),USRE2(1500),
+          USRNE(1500,4),NODEE(4),KELE,KELEL,KGROUP

C
C          COMMON /NODCOM/
C
C          RZN       : Nodal point coordinates
C          URZN      : Nodal point velocities
C          DRZN      : Nodal point displacement
C          TEMPN     : Nodal point temperature
C          USRN1     : User defined state variables (Input : At the beginning of Step N)
C          USRN2     : User defined state variables (Output: At the end of Step N)
C          KNODE     : Node number
C          COMMON /NODCOM/ RZN(2),URZN(2),DRZN(2),TEMPN,DTMPN,USRN1(1500),
+          USRN2(1500),KNODE

C
C          CURTIM: CURRENT TIME
C
C          COMMON /CLOK/ CURTIM
C
C          DTMAXC: CURRENT TIME STEP SIZE
C
C          COMMON /SSTU/ DTMAXC
C
C
C          COMMON /USRCTL/
C
C          KOBJ      : Object number
C          KSTEP     : Step number (N)
C          ISTATUS   : 0 - the beginning of the step
C                   1 - the end of the step
C          KSSSTEP   : negative step indication -1 for negative step 1 for else
C
C          WHEN (ISTATUS.EQ. 1) → USRE2/USRN2 should be updated here

```

```

C   KELE  > 0           → Element data is active
C   INODE > 0           → Node Data is active
C
C   COMMON /USRCTL/ KOBJ,ISTATUS,KSTEP,KSSSTEP
C
C
C   Branching to proper flow stress routine based on the
C   number specified in the pre-processor
C
C
C   GO TO (510,520,530,540,550,560,570,580,590,600),NPTRTN
C
C   510 CALL UFLOW1(YS,YPS,FIP,TEPS,EFEPS,TEMP)
C       RETURN
C
C   520 CALL UFLOW2(YS,YPS,FIP,TEPS,EFEPS,TEMP)
C       RETURN
C
C   530 CALL UFLOW3(YS,YPS,FIP,TEPS,EFEPS,TEMP)
C       RETURN
C
C   540 CALL UFLOW4(YS,YPS,FIP,TEPS,EFEPS,TEMP)
C       RETURN
C
C   550 CALL UFLOW5(YS,YPS,FIP,TEPS,EFEPS,TEMP)
C       RETURN
C
C   560 CALL UFLOW6(YS,YPS,FIP,TEPS,EFEPS,TEMP)
C       RETURN
C
C   570 CALL UFLOW7(YS,YPS,FIP,TEPS,EFEPS,TEMP)
C       RETURN
C
C   580 CALL UFLOW8(YS,YPS,FIP,TEPS,EFEPS,TEMP)
C       RETURN
C
C   590 CALL UFLOW9(YS,YPS,FIP,TEPS,EFEPS,TEMP)
C       RETURN
C
C   600 CALL UFLOW10(YS,YPS,FIP,TEPS,EFEPS,TEMP)
C       RETURN
C

```

```

C TO BE CONTINUED BY USER
C
      END
C*****
C*****

      SUBROUTINE UFLOW 1 (YS,YPS,FIP,TEPS,EFEPS,TEMP)

C*****
C
C
C
C*****

      IMPLICIT REAL*8 (A-H,O-Z), INTEGER*4 (I-N)
C
C ****      USER DEFINED VARIABLES ****

      CHARACTER*80 IUSRVL
      COMMON /IUSR/ IUSRVL(10)
C
C TO READ DATA (10 RESERVED LINES)
C      READ (IUSRVL(LINE NUMBER),*) DATA1,DATA2,DATA3...
C
C TO WRITE DATA (10 RESERVED LINES)
C      WRITES (IUSRVL(LINE NUMBER),*) NEWDATA1, NEWDATA2, NEWDATA3 ...
C
C ****      END      ****
C
C DESCRIPTION
C
C THIS ROUTINE IS USED TO DEMONSTRATE THE IMPLEMENTATION OF
C MATERIAL ROUTINE. ALL THE REAL VARIABLES SHOULD BE DOUBLE
C PRECISION. THE DEFINITION OF ARGUMENTS ARE DESCRIBED AS FOLLOWS:
C
C INPUT :
C
C TEPS      = EFFECTIVE STRAIN
C EFEPS     = EFFECTIVE STRAIN RATE
C TEMP      = TEMPERATURE
C

```

```

C   OUTPUT :
C
C   YS      =   FLOW STRESS
C   YPS     =   DERIVATIVE OF FLOW STRESS W.R.T. TEPS
C   FIP     =   DERIVATIVE OF FLOW STRESS W.R.T. EFEPS
C
COMMON /ELMCOM/ RZE(2,4),URZE(2,4),STSE(4),EPSE(4),EFEPSE,EFSTSE,
+       TEPSE,RDTYE,TEMPE(4),DTMPE(4),DAMAGE,
+       USRE1(1500),USRE2(1500),
+       USRNE(1500,4),NODEE(4),KELE,KELEL,KGROUP

dimension TEMPO(4),RATE(4),PSIO(4,4),QSI0(4,4),PKR0(4,4)

dimension A(2,2),B(2,2)

double precision interp2

data PSIO/2.355,1.532,0.880,0.568,
&       1.758,1.499,0.799,0.477,
&       1.497,1.139,0.875,0.887,
&       0.962,1.075,1.083,1.007/

data QSI0/0.711,0.599,0.555,0.455,
&       0.655,0.600,0.500,0.400,
&       0.652,0.588,0.545,0.588,
&       0.555,0.588,0.588,0.544/

data PKR0/0.176,0.167,0.154,0.111
&       0.180,0.171,0.160,0.148,
&       0.222,0.190,0.173,0.164,
&       0.246,0.227,0.210,0.181/

data TEMPO /260,300,340,380/
data RATE /0.001,0.01,0.1,1.0/

!       TEMP = 270.d0
!       EFEPS = 0.05d0

!       WRITE (*,*) 'Input TEMP,EFEPS'
!       READ (*,*) TEMP, EFEPS

```

```

        itemp = 1

        if(TEMP <= TEMP0(1) ) itemp = -1
        if(TEMP >= TEMP0(4) ) itemp = -4

        if(itemp < 0 ) goto 100
!
!       find location
!
        do i =2,4

        if(TEMP < TEMP0(i)) then
            itemp= i
            exit
        endif
        enddo

100    irate  = 1

        if(EFEPS <= RATE(1) ) irate = -1
        if(EFEPS >= RATE(5) ) irate = -5

        if(irate < 0 ) goto 200

        do i =2,5

        if(EFEPS < RATE(i)) then
            irate= i
            exit
        endif
        enddo
!
!       interpolate PSi
!
200    if(itemp > 0) then
            itemp1 = itemp -1
        else
            itemp = abs(itemp)
            itemp1 = itemp
        endif

        if(irate > 0) then

```

```

        irate1 = irate -1
else
    irate = abs(irate)
    irate1 = irate
endif

A(1,1)= TEMP0(itemp1)
A(1,2)= TEMP0(itemp)

A(2,1)= PSi0(itemp1,irate1)
A(2,2)= PSi0(itemp,irate1)

B(1,1) = RATE(irate1)
B(2,1) = interp2(A,1,2,TEMP,2)

A(2,1)= PSi0(itemp1,irate)
A(2,2)= PSi0(itemp,irate)

B(1,2) = RATE(irate)
B(2,2) = interp2(A,1,2,TEMP,2)

PSI = interp2(B,1,2,EFEPS,2)

!
!   interpolate QSi
!

A(1,1)= TEMP0(itemp1)
A(1,2)= TEMP0(itemp)

A(2,1)= QSi0(itemp1,irate1)
A(2,2)= QSi0(itemp,irate1)

B(1,1) = RATE(irate1)
B(2,1) = interp2(A,1,2,TEMP,2)

A(2,1)= QSi0(itemp1,irate)
A(2,2)= QSi0(itemp,irate)

B(1,2) = RATE(irate)
B(2,2) = interp2(A,1,2,TEMP,2)

```

```

QSI = interp2(B,1,2,EFEPS,2)

!
!   interpolate PKR
!

A(1,1)= TEMP0(itymp1)
A(1,2)= TEMP0(itymp)

A(2,1)= PKR0(itymp1,irate1)
A(2,2)= PKR0(itymp,irate1)

B(1,1) = RATE(irate1)
B(2,1) = interp2(A,1,2,TEMP,2)

A(2,1)= PKR0(itymp1,irate)
A(2,2)= PKR0(itymp,irate)

B(1,2) = RATE(irate)
B(2,2) = interp2(A,1,2,TEMP,2)

PKR = interp2(B,1,2,EFEPS,2)

write(*,*) PSI,QSI,PKR,TEPS,EFEPS,TEMP

STRAIN = TEPS

IF( STRAIN < 1e-10) STRAIN = 1e-5

T = TEMP+273.0

RT = 187025.0/(8.314*T)

Z = EFEPS * exp(RT)

B = EXP((187025.0/(8.314*T)))

C

A1 = Z/9.452e13

PKS = 73.40 * log( A1**0.1 + dsqrt( A1**0.2 + 1.0 ))

```

```

!       write(*,*) 'EFEPS,PKS',EFEPS,PKS

A2= PSI *(STRAIN-PKR)**2.0*log(QSI*STRAIN)

YS = PKS * exp( PSI *(STRAIN-PKR)**2.0*log(QSI*STRAIN) )
!
write(*,*) 'YS, STRAIN',YS, STRAIN, log(QSI*STRAIN)

DA2 = 2*PSI*(STRAIN-PKR)*log(QSI*STRAIN)
& + PSI*(STRAIN-PKR)**2/STRAIN

!       write(*,*) 'A2, exp(A2),DA2',A2,exp(A2),DA2,YPS

YPS = PKS * exp(A2)*DA2

!       write(*,*) 'YPS',YPS

!       IF(STRAIN > 0.5) YPS = 1.0

A3 = 0.1 * A1**(-0.9)/9.452e13
& - 1.0/(A1**0.2+1.0)**2 *0.2* A1**(-0.8)/9.452e13

FIP = exp(A2)*73.40* A3 / A4 * exp(RT)

!       FIP=0.0d0
!       write(*,*) 'FIP',FIP

!       IF(STRAIN.GT.0.3.AND.YS.GT.USRE1(1)) THEN

                YS=USRE2(1)
                YPS=0.d0
ENDIF

USRE2(1)=YS
USRE2(2)=YPS
USRE1(1)=YS
USRE1(2)=YPS

```

```

                RETURN
                END
C*****
!-----
    function interp2(X,I,J,R,N)

    implicit none

    real*8, dimension(2,N) :: X

    real*8 :: a,b,c,fa,fb, interp2, R

    integer :: I, J, N
!
!   X : 2nd order array
!   I : left
!   J : right
!   R : middle
!

    a = X(1,I)
    b = X(1,J)
    c = R
    fa = X(2,I)
    fb = X(2,J)

    if(b-a < 1e-10) then

        interp2 = fa
        return

    endif

    interp2 = ( (b-c)*fa + (c-a)*fb ) / (b-a)

    return

end

```

B. Hot flow stress user subroutine for ZAM631 alloy in DEFORM system

The below subroutine was coded with Absoft 11.0 Fortran compiler based on the flow stress model expressed as a function of plastic strain, strain rate and temperature defined by the compressive stress-strain curves measured using a Gleeble machine at the temperature range of 533-653K with the strain rate range of 10^{-3} ~1/s.

```
C*****
SUBROUTINE USRMTR (NPTRTN,YS,YPS,FIP,TEPS,EFEPS,TEMP)

C*****
C
C   THIS SUBROUTINE CALCULATES THE FLOW STRESS OF PLASTIC MATERIAL
C
C   INPUT :
C
C   NPTRTN  =   FLOW STRESS NUMBER
C   TEPS    =   EFFECTIVE STRAIN
C   EFEPS   =   EFFECTIVE STRAIN RATE
C   TEMP    =   TEMPERATURE
C
C   OUTPUT :
C
C   YS      =   FLOW STRESS
C   YPS     =   DERIVATIVE OF FLOW STRESS W.R.T TEPS
C   FIP     =   DERIVATIVE OF FLOW STRESS W.R.T. EFEPS
C
C*****

IMPLICIT REAL*8 (A-H,O-Z), INTEGER*4 (I-N)
C
C   USER SUPPLIED SUBROUTINES
C
C
C ****   USER DEFINED VARIABLES ****
```

```

C
CHARACTER*80 IUSRVL
COMMON /IUSR/ IUSRVL(10)
C
C
C TO READ DATA (10 RESERVED LINES)
C READ(IUSRVL(LINE NUMBER),*) DATA1,DATA2,DATA3...
C
C TO WRITE DATA (10 RESERVED LINES)
C WRITES (IUSRVL(LINE NUMBER),*) NEWDATA1, NEWDATA2, NEWDATA3 ...
C
C **** END ****
C
C
C
C COMMON /ELMCOM/ RZE(2,4),URZE(2,4),STSE(4),EPSE(4),EFEPSE,EFSTSE,
C + TEPSE,RDTYE,TEMPE(4),DTMPE(4),USRE1(2),USRE2(2),
C + NODEE (4), KELE
C
C
C
C COMMON /ELMCOM/
C
C RZE : Four corners coordinates
C URZE : Velocity
C STSE : Stress
C EPSE : Strain rate
C EFEPSE : effective strain rate
C EFSTSE : Effective stress
C TEPSE : Total effective strain
C RDTYE : Density
C TEMPE : Temperature
C DTMPE : Temperature rate
C DAMAGE : Damage value
C USRE1 : Element user state variable 1
C USRE2 : Element user state variable 2
C USRNE : Nodal user state variables 1,2 at 4 nodes
C NODEE : Connectivity
C KELE : Global element number
C KELEL : Local element number
C KGROUP : Material group number
C
COMMON /ELMCOM/ RZE(2,4),URZE(2,4),STSE(4),EPSE(4),EFEPSE,EFSTSE,

```

```

+          TEPSE,RDTYE,TEMPE(4),DTMPE(4),DAMAGE,
+          USRE1(1500),USRE2(1500),
+          USRNE(1500,4),NODEE(4),KELE,KELEL,KGROUP

```

C

C COMMON /NODCOM/

C

C RZN : Nodal point coordinates

C URZN : Nodal point velocities

C DRZN : Nodal point displacement

C TEMPN : Nodal point temperature

C USRN1 : User defined state variables (Input : At the beginning of Step N)

C USRN2 : User defined state variables (Output: At the end of Step N)

C KNODE : Node number

C COMMON /NODCOM/ RZN(2),URZN(2),DRZN(2),TEMPN,DTMPN,USRN1(1500),

```

+          USRN2(1500),KNODE

```

C

C CURTIM: CURRENT TIME

C

COMMON /CLOK/ CURTIM

C

C DTMAXC: CURRENT TIME STEP SIZE

C

COMMON /SSTU/ DTMAXC

C

C

C COMMON /USRCTL/

C

C KOBJ : Object number

C KSTEP : Step number (N)

C ISTATUS : 0 - the beginning of the step

C 1 - the end of the step

C KSSSTEP : negative step indication -1 for negative step 1 for else

C

C WHEN (ISTATUS.EQ. 1) → USRE2/USRN2 should be updated here

C KELE > 0 → Element data is active

C INODE > 0 → Node Data is active

C

```

COMMON /USRCTL/ KOBJ,ISTATUS,KSTEP,KSSSTEP
C
C
C   Branching to proper flow stress routine based on the
C   number specified in the pre-processor
C
C
C   GO TO (510,520,530,540,550,560,570,580,590,600),NPTRTN
C
C   510 CALL UFLOW1(YS,YPS,FIP,TEPS,EFEPS,TEMP)
C         RETURN
C
C   520 CALL UFLOW2(YS,YPS,FIP,TEPS,EFEPS,TEMP)
C         RETURN
C
C   530 CALL UFLOW3(YS,YPS,FIP,TEPS,EFEPS,TEMP)
C         RETURN
C
C   540 CALL UFLOW4(YS,YPS,FIP,TEPS,EFEPS,TEMP)
C         RETURN
C
C   550 CALL UFLOW5(YS,YPS,FIP,TEPS,EFEPS,TEMP)
C         RETURN
C
C   560 CALL UFLOW6(YS,YPS,FIP,TEPS,EFEPS,TEMP)
C         RETURN
C
C   570 CALL UFLOW7(YS,YPS,FIP,TEPS,EFEPS,TEMP)
C         RETURN
C
C   580 CALL UFLOW8(YS,YPS,FIP,TEPS,EFEPS,TEMP)
C         RETURN
C
C   590 CALL UFLOW9(YS,YPS,FIP,TEPS,EFEPS,TEMP)
C         RETURN
C
C   600 CALL UFLOW10(YS,YPS,FIP,TEPS,EFEPS,TEMP)
C         RETURN
C
C   TO BE CONTINUED BY USER
C
C         END

```

C*****

C*****

SUBROUTINE UFLOW 1 (YS,YPS,FIP,TEPS,EFEPS,TEMP)

C*****

C

C

C

C*****

IMPLICIT REAL*8 (A-H,O-Z), INTEGER*4 (I-N)

C

C**** USER DEFINED VARIABLES ****

CHARACTER*80 IUSRVL

COMMON /IUSR/ IUSRVL(10)

C

C TO READ DATA (10 RESERVED LINES)

C READ (IUSRVL(LINE NUMBER),*) DATA1,DATA2,DATA3...

C

C TO WRITE DATA (10 RESERVED LINES)

C WRITES (IUSRVL(LINE NUMBER),*) NEWDATA1, NEWDATA2, NEWDATA3 ...

C

C**** END ****

C

C DESCRIPTION

C

C THIS ROUTINE IS USED TO DEMONSTRATE THE IMPLEMENTATION OF

C MATERIAL ROUTINE. ALL THE REAL VARIABLES SHOULD BE DOUBLE

C PRECISION. THE DEFINITION OF ARGUMENTS ARE DESCRIBED AS FOLLOWS:

C

C INPUT :

C

C TEPS = EFFECTIVE STRAIN

C EFEPS = EFFECTIVE STRAIN RATE

C TEMP = TEMPERATURE

C

C OUTPUT :

C

C YS = FLOW STRESS

```

C      YPS      =  DERIVATIVE OF FLOW STRESS W.R.T. TEPS
C      FIP      =  DERIVATIVE OF FLOW STRESS W.R.T. EFEPS
C
COMMON /ELMCOM/ RZE(2,4),URZE(2,4),STSE(4),EPSE(4),EFEPSE,EFSTSE,
+      TEPSE,RDTYE,TEMPE(4),DTMPE(4),DAMAGE,
+      USRE1(1500),USRE2(1500),
+      USRNE(1500,4),NODEE(4),KELE,KELEL,KGROUP

dimension TEMP0(4),RATE(4),PSI0(4,4),QSI0(4,4),PKR0(4,4)

dimension A(2,2),B(2,2)

double precision interp2

      data PSI0/0.605,0.540,1.245,2.021,
&      0.442,0.501,0.501,0.501,
&      1.207,1.309,1.309,1.309,
&      1.707,1.509,1.509,1.509/

      data QSI0/0.411,0.433,0.611,0.677,
&      0.333,0.445,0.445,0.445,
&      0.555,0.611,0.611,0.611,
&      0.655,0.611,0.611,0.611/

      data PKR0/0.211,0.085,0.033,0.010,
&      0.227,0.113,0.051,0.028,
&      0.236,0.172,0.073,0.012,
&      0.245,0.192,0.079,0.061/

      data TEMP0 /260,300,340,380/
      data RATE /0.001,0.01,0.1,1.0/

!      TEMP = 270.d0
!      EFEPS = 0.05d0

!      WRITE (*,*) 'Input TEMP,EFEPS'
!      READ (*,*) TEMP, EFEPS

      itemp = 1

      if(TEMP <= TEMP0(1) ) itemp = -1

```

```

        if(TEMP >= TEMP0(4) ) itemp = -4

        if(itemp < 0 ) goto 100
!
!   find location
!
        do i =2,4

        if(TEMP < TEMP0(i)) then
            itemp= i
            exit
        endif
        enddo

100   irate  = 1

        if(EFEPS <= RATE(1) ) irate = -1
        if(EFEPS >= RATE(5) ) irate = -5

        if(irate < 0 ) goto 200

        do i =2,5

            if(EFEPS < RATE(i)) then
                irate= i
                exit
            endif
            enddo
!
!   interpolate PSi
!
200   if(itemp > 0) then
            itemp1 = itemp -1
        else
            itemp = abs(itemp)
            itemp1 = itemp
        endif

        if(irate > 0) then
            irate1 = irate -1
        else
            irate = abs(irate)

```

```

    irate1 = irate
endif

A(1,1)= TEMP0(itemp1)
A(1,2)= TEMP0(itemp)

A(2,1)= PSi0(itemp1,irate1)
A(2,2)= PSi0(itemp,irate1)

B(1,1) = RATE(irate1)
B(2,1) = interp2(A,1,2,TEMP,2)

A(2,1)= PSi0(itemp1,irate)
A(2,2)= PSi0(itemp,irate)

B(1,2) = RATE(irate)
B(2,2) = interp2(A,1,2,TEMP,2)

PSI = interp2(B,1,2,EFEPS,2)

!
!   interpolate QSi
!

A(1,1)= TEMP0(itemp1)
A(1,2)= TEMP0(itemp)

A(2,1)= QSi0(itemp1,irate1)
A(2,2)= QSi0(itemp,irate1)

B(1,1) = RATE(irate1)
B(2,1) = interp2(A,1,2,TEMP,2)

A(2,1)= QSi0(itemp1,irate)
A(2,2)= QSi0(itemp,irate)

B(1,2) = RATE(irate)
B(2,2) = interp2(A,1,2,TEMP,2)

QSI = interp2(B,1,2,EFEPS,2)

```

```
!
```

```

!      interpolate PKR
!
A(1,1)= TEMPO(itemp1)
A(1,2)= TEMPO(itemp)

A(2,1)= PKR0(itemp1,irate1)
A(2,2)= PKR0(itemp,irate1)

B(1,1) = RATE(irate1)
B(2,1) = interp2(A,1,2,TEMP,2)

A(2,1)= PKR0(itemp1,irate)
A(2,2)= PKR0(itemp,irate)

B(1,2) = RATE(irate)
B(2,2) = interp2(A,1,2,TEMP,2)

PKR = interp2(B,1,2,EFEPS,2)

write(*,*) PSI,QSI,PKR,TEPS,EFEPS,TEMP

STRAIN = TEPS

IF( STRAIN < 1e-10) STRAIN = 1e-5

T = TEMP+273.0

RT = 251916.0/(8.314*T)

Z = EFEPS * exp(RT)

B = EXP((251916.0/(8.314*T)))
C

A1 = Z/3.761e20

PKS = 67.78 * log( A1**0.1 + dsqrt( A1**0.2 + 1.0 ) )

!      write(*,*) 'EFEPS,PKS',EFEPS,PKS

```

```

A2= PSI *(STRAIN-PKR)**2.0*log(QSI*STRAIN)

YS = PKS * exp( PSI *(STRAIN-PKR)**2.0*log(QSI*STRAIN) )
!
write(*,*) 'YS, STRAIN',YS, STRAIN, log(QSI*STRAIN)

DA2 = 2*PSI*(STRAIN-PKR)*log(QSI*STRAIN)
& + PSI*(STRAIN-PKR)**2/STRAIN

! write(*,*) 'A2, exp(A2),DA2',A2,exp(A2),DA2,YPS

YPS = PKS * exp(A2)*DA2

! write(*,*) 'YPS',YPS

! IF(STRAIN > 0.5) YPS = 1.0

A3 = 0.1 * A1**(-0.9)/3.761e20
& - 1.0/(A1**0.2+1.0)**2 *0.2* A1**(-0.8)/3.761e20

FIP = exp(A2)*67.78* A3 / A4 * exp(RT)

! FIP=0.0d0
! write(*,*) 'FIP',FIP

! IF(STRAIN.GT.0.3.AND.YS.GT.USRE1(1)) THEN

        YS=USRE2(1)
        YPS=0.d0
    ENDIF

    USRE2(1)=YS
    USRE2(2)=YPS
    USRE1(1)=YS
    USRE1(2)=YPS

    RETURN
    END
C*****

```

```

!-----
function interp2(X,I,J,R,N)

implicit none

real*8, dimension(2,N) :: X

real*8 :: a,b,c,fa,fb, interp2, R

integer :: I, J, N

!
! X : 2nd order array
! I : left
! J : right
! R : middle
!

a = X(1,I)
b = X(1,J)
c = R
fa = X(2,I)
fb = X(2,J)

if(b-a < 1e-10) then

    interp2 = fa
    return

endif

interp2 = ((b-c)*fa + (c-a)*fb) / (b-a)

return

end

```

초 록

본 연구는 상용 AZ31합금과 신개발 ZAM631합금의 압출변형 중에 발달하는 집합조직 예측을 통해 마그네슘합금의 성형성을 획기적으로 향상시키기 위한 연구이다.

온도변화에 따른 미시적 소성변형기구의 고찰을 위하여 여러 슬립 및 쌍정모드의 임계전단응력을 도출하였다. 이를 위하여 미소역학에 기초한 visco-plastic self-consistent-genetic algorithm (VPSC-GA) 전산 모사를 수행하였다. Basal 슬립과 tensile twin 모드의 임계전단응력은 온도변화에 민감하게 반응하지 않으며, 반대로 prismatic, $\langle c+a \rangle$ 슬립과 compressive twin모드의 임계전단응력은 온도변화에 크게 의존하는 것으로 관찰되었다.

AZ31합금과 ZAM631합금에 대하여 고온압축실험을 수행하여 유동응력에 미치는 온도 및 변형율속도의 영향을 분석하였다. 모든 변형조건에서 변형 중 연화현상이 발생했으며 미세조직 분석을 통해 동적재결정이 원인임을 규명하였다. 또한 동적재결정립의 크기와 Z (zener-hollomon parameter)의 관계를 정립하였고 변형 중의 연화현상을 반영한 유동응력 방정식을 구하였다. 유동응력 방정식으로 구한 응력곡선은 실험결과와 잘 일치하였다.

압출공정의 거시적 소성변형 해석을 위해 상용 유한요소 해석 프로그램인 DEFORM-3D를 사용하였다. AZ31합금 판상(3t)과 ZAM631합금 봉상(16 Φ) 압출재의 간접압출 모사를 수행하였고 압출비는 각각 56:1과 25:1이었다. 압출변형 중 빌렛의 온도분포, 유효변형율속도 및 유효변형율분포를 분석하고 압출재 잔여부분에 해당하는 위치에서의 변형거동을 각각 비교하였다.

압출변형 중에 발달하는 집합조직을 예측하기 위해 유한요소

해석 수행으로 획득한 거시적 압출변형거동을 미시적 변형거동에 연계시킨 VPSC-FE모델을 사용하여 새로운 집합조직발달 예측기법을 개발하였다. 현재까지 제안된 집합조직발달 예측기법들은 소재의 변형이력을 집합조직발달에 반영하는 데에 한계가 있었다. 특히 Voce경화법칙을 사용하는 VPSC모델의 경우에 압출변형 중에 발생하는 연화현상을 모사할 수 없는 한계로 인해 변형 중 연화현상이 발생하는 압출변형으로 인한 집합조직발달 예측에 한계가 있었다. 개발한 집합조직발달 예측기법을 사용하여 AZ31합금 판상(3t) 및 ZAM631합금 봉상(16Φ) 압출재의 집합조직발달을 예측하였다.

주요어: 마그네슘합금, 압출, 집합조직, 유한요소해석, VPSC

학 번: 2004-30237